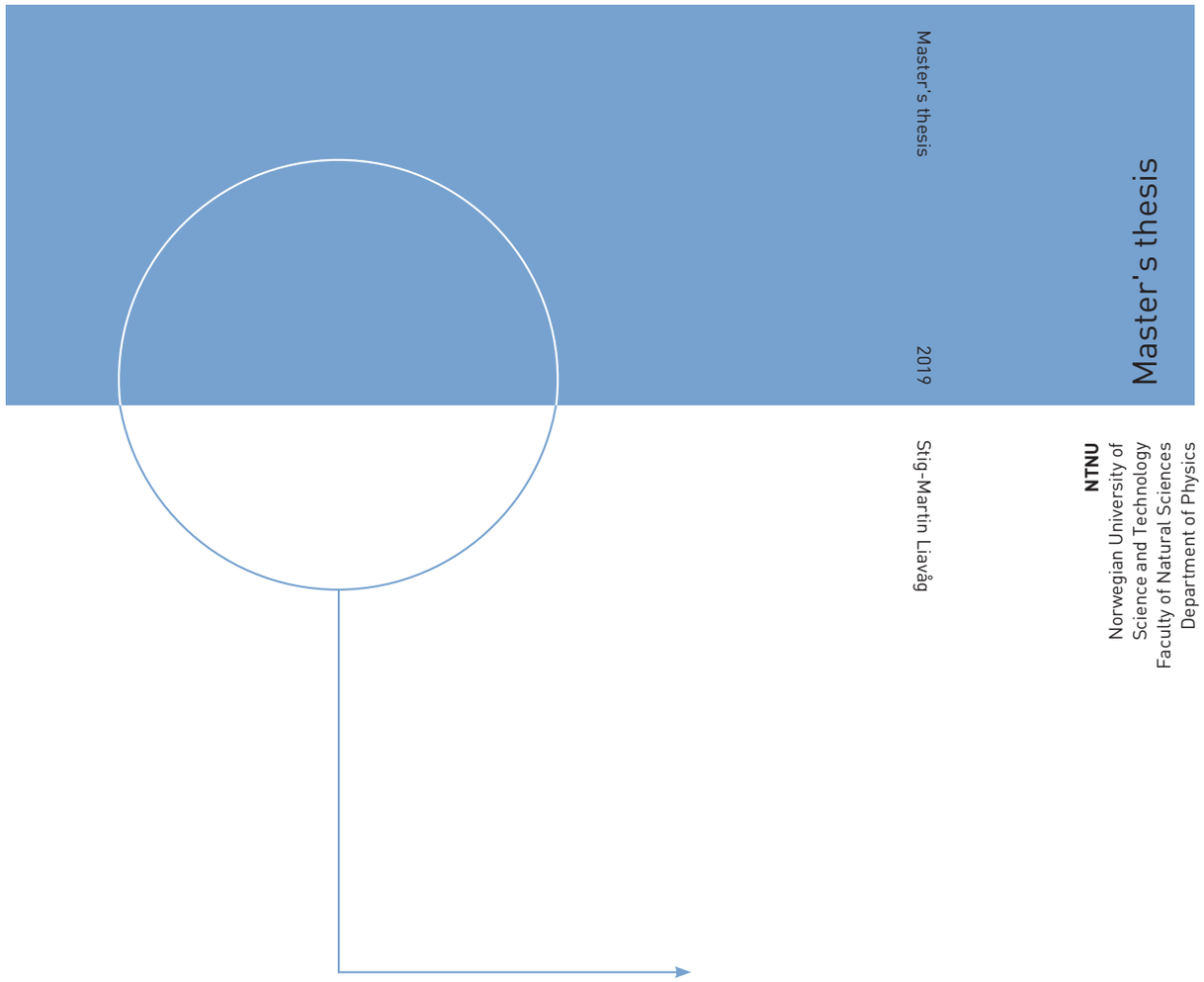

Stig-Martin Liavåg

Modeling nanoparticle transport in tumors with a pore network model

June 2019

NTNU
Norwegian University of
Science and Technology

NTNU
Norwegian University of
Science and Technology

NTNU
Norwegian University of
Science and Technology

Modeling nanoparticle transport in tumors with a pore network model

Stig-Martin Liavåg

Applied Physics and Mathematics
Submission date: June 2019
Supervisor: Catharina de Lange Davies
Co-supervisor: Magnus Aashammer Gjennestad

Norwegian University of Science and Technology
Department of Physics

Acknowledgments

This work will be submitted as a thesis for the degree Master of Science in Physics and Mathematics at the Norwegian University of Science and Technology, and was performed at the Department of Physics in addition to the Centre of Excellence PoreLab.

During my final years as a student I have had the privilege to attend the courses and study under the supervision of Professor Catharina de Lange Davies at the Department of Physics, and would like to thank her for offering me an interesting topic and providing practical insight into cancer research, and PhD candidate Magnus Aashammer Gjennestad at PoreLab for sharing an office space and supplying continuous advice and knowledge on the physics and numerical modeling.

I wish to offer my gratitude to Professors Signe Kjeldstrup and Dick Bedeaux at PoreLab, Professor Miguel Rubi at the Department of Fundamental Physics at the University of Barcelona and Professor Bjørn A.J. Angelsen at the Department of Circulation and Medical Imaging for expressing constructive interest in my work and taking part in interesting conversations and feedback throughout the semester.

Also, I must also express my gratitude to friends, family and my dear Stine for motivation, encouragement and continuous support during this final semester and over the course of my studies and time spent in Trondheim.

Stig-Martin Liavåg Trondheim, Juni 2019

Abstract

A possible approach in cancer therapy is to encapsulate cytotoxic drugs in nanoparticles to increase drug specificity while reducing the systemic toxicity. Focused ultrasound in combination with nanoparticles can improve the delivery of drugs to cancer tumors. Acoustic Cluster Therapy is a novel concept in which focused ultrasound in conjunction with microbubbles has been demonstrated to improve delivery of encapsulated drugs and successfully achieving a therapeutic response.

A rigid pore network model, based on similar models created by members of PoreLab for two-phase flow in porous media, was developed to look at the transport of nanoparticles subject to the advection-diffusion equation when driven by a ultrasound-induced pressure gradient. Sets of equations were derived for fluid flow and individual particles at the pore-scale level. Parameter studies were conducted to established power law relations between system input variables and stochastic nanoparticle transport at the tissue-scale level.

Additionally, theory for an elastic pore network model was derived, hypothesizing than an oscillating pressure boundary condition causes expansion and contraction of the pores, and net fluid transport through the network.

Finally, empirical sets of equations were established to estimate and extrapolate particle transport for finite times under various parameters, which is imperative in furthering a basic understanding of the system to optimize drug delivery and thus improving cancer therapy.

Samandrag

Ei mogleg tilnærming i kreftbehandling er å innkapsle cytotoksiske medisinar i nanopartiklar for å auke spesifisiteten til medisinane samtidig som systemisk toksisitet blir redusert. Fokusert ultralyd i kombinasjon med nanopartiklar kan auke transporten av medisinar til kvreftsvulstar. Acoustic Cluster Therapy er eit nytt konsept der fokusert ultralyd saman med mikrobobler har demonstrert ei forbetring i transporten av innkaplsa medisinar og dermed oppnådd ein vellukka terapeutisk respons.

Ein porenettverksmodell, basert på liknande modellar laga av medlem hjå PoreLab for tofasestraum i porøse medier, blei utvikla for å sjå på transport av nanopartiklar underlagt adveksjon og diffusjon når dei blir drivne av ein ultralydindusert trykkgradient. Likningssett ble utleia for væskestraum og individuelle partiklar på poreskalanivå. Parameterstudiar blei utførte for å etablere kraftlovrelasjonar mellom variablar inn i systemet og stokastisk nanopartikkeltransport på vevskala.

I tillegg blei toeri for ein elastisk porenettverksmodell utleia, med hypotesen om at eit oscillerande grensevilkår forårsaker ekspansjon og samantrekning av porene, og dermed netto væsketransport gjennom vevet.

Til slutt blei empiriske likningssett etablerte for å kunne estimere og ekstrapolere partikkel-transport over ei endeleg tid for ulike parameter, som er avgjerande for å kunne fremje ei grunnleggjande forståing av systemet og optimalisere leveringa av medisinar og dermed forbetre kreftbehandling.

Abbreviations

ACT	Acoustic Cluster Therapy
CW	continuous wave
DF	duty factor
ECM	extracellular matrix
EPR	enhanced permeability and retention effect
IFP	interstitial fluid pressure
link	The term for a pore in the interstitium
MB	microbubble
MI	mechanical index
NP	nanoparticle
PRF	pulse repetition frequency
PRP	pulse repetition period
PW	pulsed wave
US	ultrasound

Contents

1 Introduction and background

Cancers can be defined as a kind of abnormal tissue where cells grow uncontrollably, causing an increase in the number of dividing cells, which results in a tumor [1, p. 758]. It is a term that describes diseases growing in tissues and spreading widely through the body of the affected organism, eventually killing it. Tumors can originate and grow in any organ, and can be grouped into several categories depending on origin, such as carcinomas due to epithelial cells and sarcomas from connective tissue.

Cancers are a part of life, and affect 36 % of all men and 30 % of all women in Norway before the age of 75 [2]. Cancers are the second-leading cause of death after cardiovascular diseases, and is the focus of a great deal of research [1, p. 758]. Approximately 9.6 million individuals died from cancer in 2018, which accounted for around 1 in 6 of all global deaths annually, and an estimated 30 % to 50 % of these cancer deaths could have been prevented and cured [3]. 11 000 of these occurred in Norway, and over 33 000 new cases were diagnosed in 2017, which is an increase of 2.24 % from 2016 [2]. In 2016 it was expected that the number of diagnosed cancer cases in Norway will be increased by 42 % for men and 27 % for women in 2030 [4]. By that time, Norway's aging population will have increased dramatically, while the risk of being diagnosed with cancer will only have decreased marginally in that time period. In Europe and North America, 10 % of those in cancer therapy are battling a second cancer. The continuation of an unhealthy lifestyle, genetic predisposition and late effects from previous treatments can induce malignancies at a later point in the patient's life [5, p. 412]. In order to face this increase, large resources will have to be invested into hospitals and health care.

In regular cancer therapy, radiotherapy and chemotherapy are nonspecific to cell type, cancerous or not. Conventional chemotherapy therefore is systemic, which can have toxic effects on normal tissue. The maximum dose size can be administered is limited due to toxicity, and the treatment can have ravaging side effects on the patient. Surgical tumor removal leave scars and permanent reminders of the treatment, and cases that fail to respond to these treatments have deadly consequences. Due to breakthroughs in nanotechnology, it is possible to incorporate therapeutic agents, such as viruses and drugs inside nanoparticles (NPs) [6]. These NPs can have sizes from 1 nm to 1000 nm. Facilitated by the enhanced permeability

and retention effect (EPR) effect present in tumors, the NPs will passively accumulate in the tumor tissue [7], reducing systemic exposure and enabling preferential drug delivery [6, 7]. In order for the treatment to be successful, sufficient amounts of drugs need to be accumulated and distributed inside the tumor

Several challenges are faced here, both to elevated interstitial fluid pressure (IFP) and lack of pressure gradients that can transport the particles across the vessel and into the tumor [7]. Understanding the delivery of therapeutic agents into tumors is an important aspect to consider in cancer treatments. Traditional cancer therapy, such as chemotherapy, and drug delivery is limited by the physiology of the tumor, as the drug has to be delivered through the blood stream in a non-uniform manner, from the vascular system to the cell interstitium. One method to improve the transport is by the use of ultrasound (US), which can transfer momentum indirectly through the formation and interaction with gas bubbles, and directly by radiation force. It has been known since the late 1980s that US increases the permeability of cell membranes by cavitation [8].

A hypothesis is that the application of US might result in net transport of fluid into the interstitium. Two effects will be investigated in this thesis. In the first case, the continuous application of US and radiation force results in a pressure gradient in a porous medium, which by convection causes streaming of fluid. By placing NPs in a rigid pore network model, the advective and diffusive effects of the particle transport is modeled. A parameter study was conducted to investigate how different properties affect the stochastic behavior of the NP in the network. For the second case, a vibrating gas bubble is situated in a capillary, which acts as an oscillating boundary condition, applying pressure to an elastic pore network. The pores can contract or expand, depending on the pressure amplitude. A basic set of theoretical and discretized equations will be presented for this case. The aim of studying these kinds of networks is to provide further understanding of the relative driving forces in relation to pore properties. While the pore network does not model the complexity of the interstitium, this work is essential in furthering a basic understanding of NP transport in tissue and the effect of US, which is imperative for optimizing drug delivery and thus improving cancer therapy.

1.1 Causes of cancer and modern treatment

In order for healthy cells to function normally, a large number of processes have to function as intended and be coordinated between a large amount of cells. Tumors typically arise when an imbalance occurs between the processes of cell division, cell differentiation and cell death [1, p. 758]. These cell processes are usually regulated by the signaling mechanisms that allow cells to communicate not only with its neighbors, but also with the local environment. The cells in the tissue are given signals to proliferate, divide or go into apoptosis if certain conditions are satisfied. The pathways responsible for the signaling can become erroneous or altered in

cancer cells, causing constant division with no growth factor present, or to either ignore or block pathways that trigger apoptosis, i.e. programmed cell death. The cancer cells are hence able to proliferate and survive under conditions that normally would cause cell death in healthy cells.

The causes of cancers have been studied for over two centuries, and the leading conclusion is that cancers usually emerge due to environmental agents and lifestyle factors, which act to trigger DNA mutations [1, p. 766]. Development of cancers can be contributed to external factors, such as smoking, carcinogenic chemicals or ionizing and ultraviolet radiation, in addition to internal factors, such as genetics [1, p 766-771]. All individuals are therefore inherently at risk of developing cancer, with some population groups being more so than others. The mutations that deregulate the control mechanisms occur in three groups of genes: proto-oncogenes, tumor suppressor genes and DNA stability genes [5, p. 273]. Proto-oncogenes are essential genes for the regulation of cell survival and growth. A mutation can turn these into oncogenes, which can cause abnormal cell growth or inhibition of apoptosis. Tumor suppressor genes restrain cell proliferation, and are part of the same signaling components as proto-oncogenes, but reversely act as negative growth regulators. The loss or inhibition of these genes cause can therefore lead to excessive cell proliferation [1, p. 782]. The last group, DNA stability genes, are responsible for monitoring and maintenance of DNA integrity. Losing these can lead to defective sensing of DNA lesions and improper repair of damaged DNA templates [5, p. 273].

Because of all these possible mutations that can disrupt the different signaling pathways and gene expression, uncontrolled proliferation is one of the defining characteristics of cancers. An additional danger of cancer cells is the ability to spread to other sites in the body of the organism through processes known as metastasis and invasion. The former concerns the migration and penetration of cancer cells into nearby tissue, and the latter involves cancer cells entering bodily fluids, such as blood, to be transported away and forming metastases that are physically disconnected and growing independently from the tumor of origin. Such spreading complicates treatment, and only 10 % of cancer deaths are caused by the primary tumor itself. The most common approach to treatment is surgical removal of the primary tumor in conjunction with radiation and chemotherapy to remove cancer cells that remain or have spread [1, p. 787].

1.2 Transport and cancer physiology

For a cancer to be cured, the drugs must be able to traverse the vascular, transvascular and interstitial areas in the tissue in order to affect all tumor cells. Only a single surviving cancer cell can form the basis for tumor regrowth. In the vascular area, convective transport through the blood stream provides the supply of drugs to close proximity of the tumor tissue. A combination of diffusive and convective

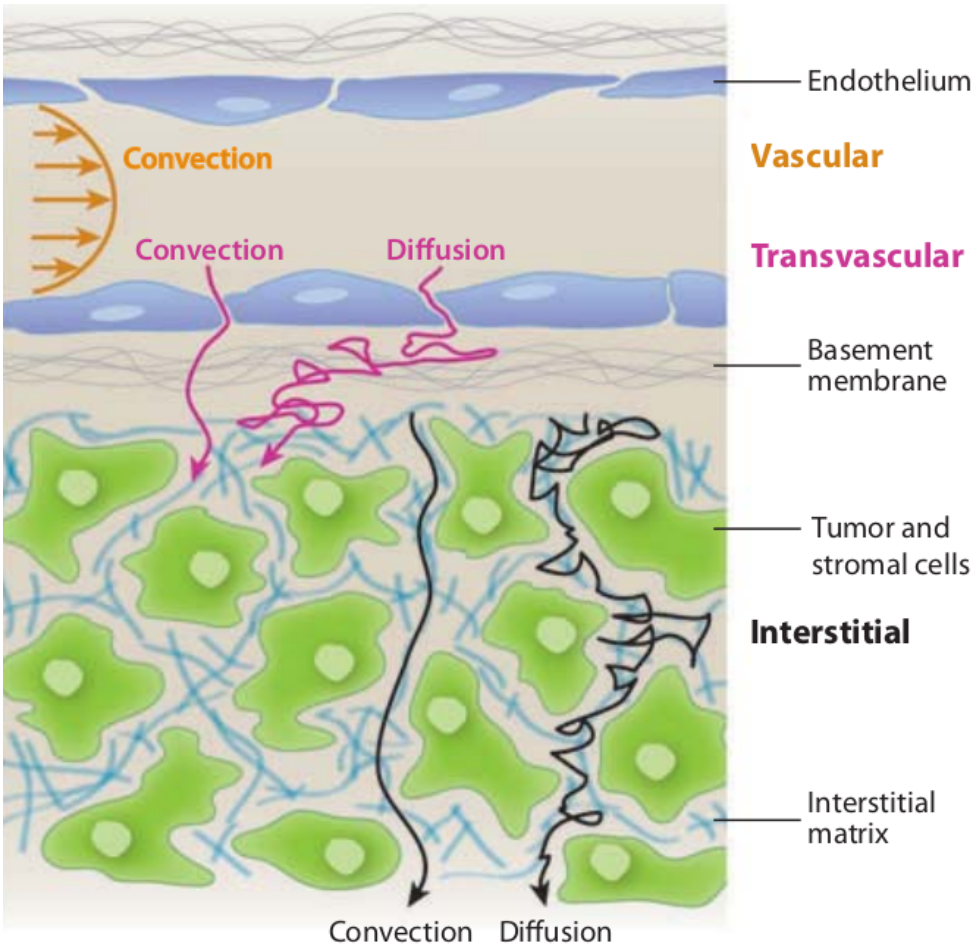

Figure 1.1: Schematic of the important processes for transport in the vascular, transvascular and interstitial areas of the tissue [9]. Convective vascular transport provides the supply of drugs to close proximity of the tumor tissue. A combination of diffusive and convective transport is responsible for the movement of drugs into the transvascular area, through the vessel wall and basement membrane. Interstitial transport also occurs through the combination of convection and diffusion [9].

transport is responsible for the movement of drugs into the transvascular area, through the vessel wall and basement membrane. In the interstitium, transport also occurs through the combination of convection and diffusion [9]. A schematic of the different transport processes in the tumor can be seen in fig. 1.1. To understand how drug delivery can be improved one needs to know how cancer physiology differs from normal, healthy tissue, in addition to how this physiology leads to further difficulties in the transport of oxygen, nutrients and drugs into the tissue. On the other hand, some aspects of tumor physiology can be beneficial when examining transport.

The EPR effect, which is recognized as a universal trait of solid tumors, is of particular importance for the ability of NPs to preferentially accumulate at the tumor site [10]. The effect is defined as increased cell leakiness and impaired lymphatic function, and the basis for this effect is vascular permeability and hydraulic conductivity that, compared to healthy tissue, is significantly higher in tumors [6]. Additionally, the basement membranes which surround the vessels in healthy tissue may be damaged or missing in some tumors, and the lymphatic vessels may even be absent in solid tumors [11]. The EPR effect may be the most important concept in modern drug delivery, but its usefulness for delivering NPs homogeneously to the tumor might effectively be reduced due to the complexity and irregularity of the tumor environment [12].

The interstitial space is a complex environment, and varies according to tissue type. The cells are situated in the extracellular matrix (ECM), which in turn defines the physical properties of the environment, such as providing support for the tissue and enabling extracellular signaling. The extracellular matrix (ECM) largely consists of components such as collagen, proteoglycans and other matrix-binding molecules [14]. A schematic of the interstitium can be seen in fig. 1.3. In some kinds of soft tissues, such as cartilage and cornea, collagen accounts for more than two-thirds of the protein content in the ECM. Collagen is responsible for the structural and mechanical integrity in the ECM, while proteoglycans are attached to the collagen network and regulate transport of fluids and solutes, in addition to resisting compressive forces [13]. The organization of collagen in combination with protoglyceans contributes strongly to fluid flow resistance in the interstitial space, and well-defined collagen networks are more resistant to macromolecular drug penetration in comparison to tumors with less organized networks. Those kinds of tumor with more organized networks are usually also more stiffer [13]. This can be seen in fig. 1.2 for two carcinomas and sarcomas with different collagen content and network connectivity.

The interstitial fluid is closely connected with the lymphatic system, which drains the plasma that has leaked from the capillary back into the vascular system. Hydrostatic and osmotic pressure gradients act as the driving forces behind fluid motion between blood in the capillary, interstitial space and lymphatic system [14]. The IFP is affected by several factors, such as local deformations, from for example physical exercise, blood pressure, the metabolism of the surrounding tissue, the level of hydration and composition of ECM components. The lymphatic system is

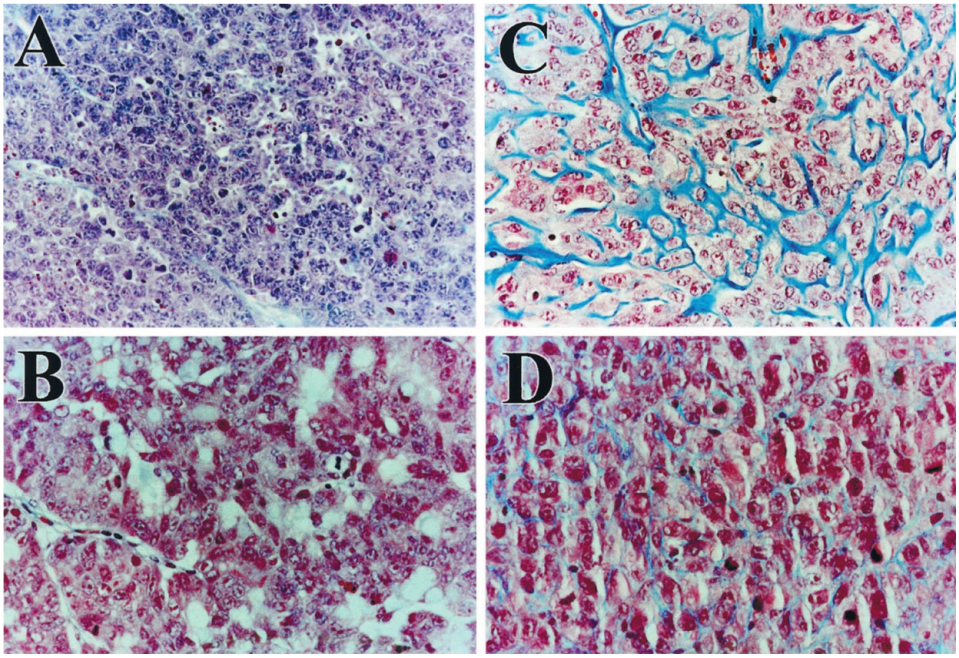

Figure 1.2: Staining of collagen in four different tumors: MCaIV (A), LS174T (B) U87 (C) and HSTS26T (D). The most important feature to note is the lack of an interconnected collagen network in the two carcinomas (A) and (B). In contrast to the carcinoma tissues, the sarcomas (C) and (D) have sections that show well-organized interconnected collagen lattices surrounding cell clusters, and are more stiffer than the carcinomas. Collagen is associated with the presence of blood vessels, and both carcinomas exhibit deficient collagen assemblies [13].

also severely degraded in tumors, which means that drainage of interstitial fluid in the ECM is hindered, causing IFP to be heightened.

Resistance to drug transport arises from abnormalities in the tumor environment, which is coupled with other unusual properties of the tumor, such as abnormal capillary networks, accumulation of solid stress, a dense interstitial space, and elevated IFP. These properties cause the tumor environment to have barriers to drug delivery, such as heterogeneous vascularity, non-uniform perfusion, dense ECM components that limit diffusion and lowered pressure gradients that obstruct transvascular transport. The overall heterogeneity and multitude of barriers in tumors are major challenges when dealing with targeted drug delivery.

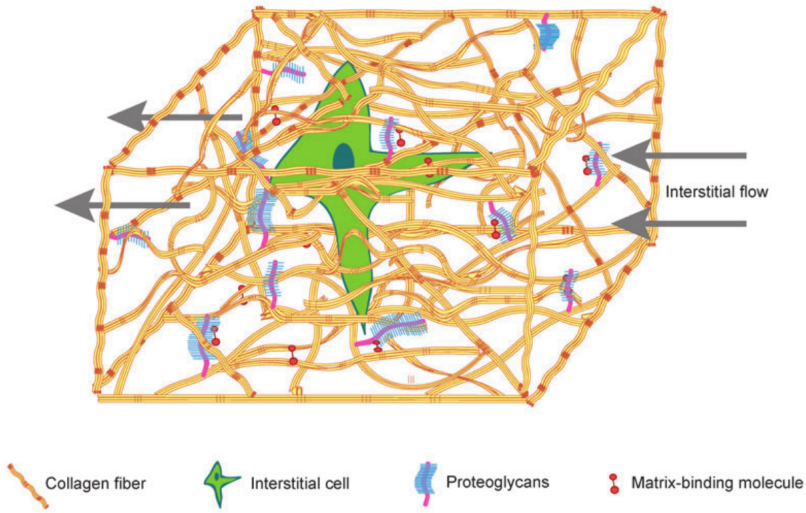

Figure 1.3: A schematic of the interstitial space showing the main features and components of the ECM. Collagen fibers are arranged in a matrix network surrounding the interstitial cells. The fibers are connected to each other and the cells by proteoglycans and other matrix-binding molecules, such as lamins, and fibrin in some cases. Interstitial fluid fills the space between ECM components, and will undergo a resistance to flow that depends on the tissue matrix properties [14].

1.2.1 Vascular networks

Due to both genetic and epigenetic changes the tumor can produce a mix of proangiogenic factors which allow cells to grow beyond the approximately 200 µm diffusion distance of oxygen and other required nutrients in the tissue [14]. This production happens uncontrollably and can be considered important in angiogenic tumors and metastases, and causes the blood vessels to be highly irregular in comparison to normal tissue vasculature[6]. In normal tissues, blood vessels branch in an orderly fashion into smaller and shorter units, which can be said to be homogeneously distributed. Tumor vessels, on the other hand, are distributed in a rather heterogeneous fashion. Tumors are known to have tortuous vessel architectures with shunts, vascular loops, wide ranges of intravascular distances and large avascular areas [15]. This difference in vessel distribution is visualized in fig. 1.4.

Additionally, tumor vessel walls are found to be unusually leaky in comparison to normal tissue, which can be attributed to defective endothelial monolayers, intercellular openings, transcellular holes and fenestrations [16]. Due to these faults, the vessel walls can be hyperpermeable and leaky in some regions, while not exhibiting this property in other regions, causing heterogeneous transport over the transvascular area. While the leakiness and permeability forms a part of the EPR

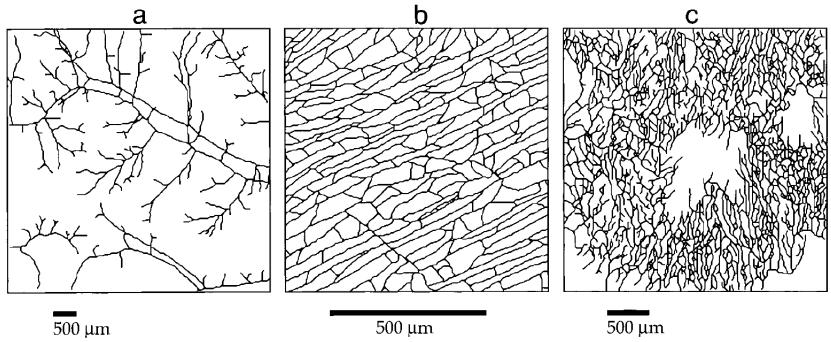

Figure 1.4: (a) Normal subcutaneous arteries and veins. The vessels become shorter as the degree of branching increases. (b) Subcutaneous capillaries distributed homogeneously. (c) Heterogeneous distribution of vessels in an adenocarcinoma (LS174T). The degree of branching and vessel sizes are highly irregular, resulting in an inhomogeneous vessel distribution and avascular spaces in the tissue [15].

effect, these heterogeneities in the tumor environment also severely impair ability to uniformly deliver these drugs throughout the tumor [6].

1.2.2 Uncontrolled cell proliferation

The rapid proliferation and cell-growth in a highly restricted volume, and therefore tissue expansion, leads to accumulation of solid stress by contact of ECM components and by cell-to-cell. In tumors this is the result of high collagen production. This proliferation can cause compression and collapse of the lymphatic system and blood vessels, limiting transport and potential drug delivery through the vascular system [17]. The flow of blood is hindered, since resistance to flow increases. Perfusion therefore tends to decrease as the tumor is growing [6].

Higher tumor densities, caused by cells and collagen, also hinder diffusion into the tumor as a result increased tortuosity, which is a measure of diffusive hindrance due to the increased path length both fluid and particles need to travel in the tissue [18]. Tortuosity is here defined as

$$\lambda = \sqrt{\frac{D_{\text{aq}}}{D_{\text{eff}}}} = \frac{L}{L_0}, \tag{1.1}$$

where D_{aq} is the diffusion constant for a solute molecule in a free isotropic solution and L_0 the path length in a free solution and D_{eff} and L the equivalent measures in the tissue. The relation in eq. (1.1) shows that if the cells are more tightly packed and the tortuosity increases, D_{eff} decreases, and transport into the interstitium is further hindered in the tumor tissue. This is visually summarized in fig. 1.5. Higher

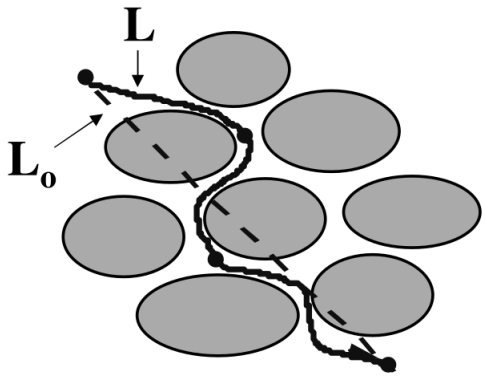

Figure 1.5: Schematic of the tortuous path length of molecules diffusing into the tumor interstitium. The gray spheres represent cells in the ECM, L_0 the linear path length in a free solution and L the effective path length. As tumor density increases, the ratio between path lengths, and thus the tortuosity, increases [19].

cell densities therefore make it more challenging to deliver therapeutic drugs into the tumor tissue.

1.2.3 Elevation of IFP

The combined effects of a nonfunctional lymphatic system due to compression in addition to high permeability of blood vessels leads to accumulation of fluids and macromolecules from the plasma in the interstitial space. As drainage is reduced, IFP becomes similar to the microvascular pressure (MVP) [20]. At the interstitial boundary, the IFP is equal to the MVP, and rises sharply to a maximum at 200 µm to 1000 µm from the endothelial wall. In normal tissues the IFP is usually at or slightly above atmospheric pressure at 5 mmHg, whereas the upper range for tumors will be 10 mmHg to 30 mmHg [21], approximately 1.33 kPa to 4.0 kPa. An example of this can be seen in fig. 1.6. IFP gradients are approximately nonexistent far away from the endothelial wall. The driving convective force component of mass transport is therefore negligible, and diffusion becomes the dominating mechanism for drug carrying drugs. As each blood vessel in the leaky vasculature must supply a relatively large tumor volume, drug penetration distance is shortened and drugs poorly distributed.

A flat IFP profile inside the tumor in addition to the steep pressure gradient which results from the equilibrium between IFP and MVP at the tumor boundary, means that the driving forces for extravasation of both fluid and molecules are effectively reduced. Additionally, a convective flux will be generated that pushes fluids and solutes down the gradient towards the tumor periphery and out of the interstitium,

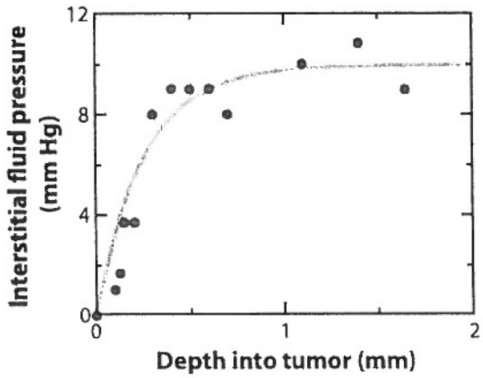

Figure 1.6: An example of IFP measurements from breast cancer in mice. The solid line represents the theoretical pressure profile, while the dots are data points. Notice how the pressure sharply increases close to the tumor surface and flattens out in a plateau after approximately 1 mm [21, 9].

further hindering transport and flow into the tumor [21].

1.3 Ultrasound

US is a term usually applied to waves where the frequency exceeds the range of human hearing capabilities, i.e. above 20 kHz [22]. US is mechanical waves of an acoustic nature, which unlike electromagnetic waves, that can travel in vacuum, requires a medium for propagation. The scattering of these wave have provided the basis for US imaging, and the energy absorption in tissue and transfer of momentum from the propagating wave can in combination with microbubbles (MBs) result in beneficial effects for drug delivery such as enhanced membrane transport, changes in capillary permeability, radiation force and streaming, in addition to mechanical or thermal changes in the delivery vehicles themselves [23].

1.3.1 Principles

When a pressure source, such as a sinusoidally driven piston, is put on the boundary of a material, the waves will propagate through the material as compression waves [22]. Since medium displacement is parallel to the wave instead of transverse, as is the case for a guitar string, the US acts as longitudinal compression waves [24]. Wave propagation in a medium causes local motion of particles, where both pressure and density will vary locally. Areas with high acoustic pressures will compress, while areas where pressures are low will experience rarefaction [24]. These changes occur as the wave cycles through each period. In terms of particle displacement,

the one-dimensional wave equation is given as

$$\frac{\partial^2 \Psi}{\partial t^2} = c^2 \frac{\partial^2 \Psi}{\partial x^2}, \tag{1.2}$$

where $\Psi(x,t)$ is the displacement, c the propagation speed and x the axis which the wave travels along [25]. The wave equation can also be described by particle velocity $u(x,t)$ or pressure $p(x,t)$. A solution to eq. (1.2) for a wave propagating along the x axis as

$$\Psi(x,t) = \Psi_0 \cos(\omega t - kx). \tag{1.3}$$

The solution has a sinusoidal nature, and Ψ_0 denotes the displacement amplitude, ω the angular frequency and k the wave number.

Scattering of waves due to local differences in tissue compressibility and density is the basis for US imaging [23]. Scattering occurs due to local inhomogeneities in tissue properties as the wave propagates through the tissue. As the wave encounters these inhomogeneieties, components of the wave will be reflected to paths that differ from the original wave-propagation direction. This effect occurs due to small differences in the acoustic impedance of the medium, which is defined as [25]

$$Z = \rho c, \tag{1.4}$$

where ρ is the medium density. When a wave passes from one medium to another with a different acoustic impedance, a certain amplitude of the transmitted wave will be lost trough reflection at the material interfaces. These kinds of reflections can occur multiple times, and more energy is lost for each reflection due to absorption, since the path length of the wave increases.

In addition to scattering, some acoustic energy is irreversibly lost as heat to the tissue through absorption. Absorption is the dominating factor in energy loss, and is given as a loss factor $e^{-\alpha x}$, where α is an absorption coefficient which depends on and is proportional to US frequency and intensity [22]. This effect, in addition to reflection, means that the US wave amplitude decreases as it propagates through tissue. Waves therefore have higher penetration depths for lower frequency ranges. The absorbed heat can be exploited beneficially in order to increase drug diffusion, ease absorption of drugs and enhance perfusion in the affected area [24].

The relation between frequency f and acoustic wavelength λ is given by

$$\lambda = \frac{c}{f}, \tag{1.5}$$

where c is the acoustic propagation speed of the wave [25]. In soft tissues the propagation speed is approximately $c \approx 1540\,\mathrm{m\,s^{-1}}$. The time of one cycle, the period, is the inverse of frequency, $T = 1/f$. According to eq. (1.5), the wavelength shortens as frequency is increased, and it is possible to image smaller objects for higher frequency ranges. Since penetration depth increases for lower frequencies, there is an inverse relationship between penetration depth and image resolution [25].

US waves can either be delivered as a continuous wave (CW), or as pulses for a short span of time, called pulsed wave (PW) ultrasound. The transducer is excited for a certain time period, and then shut off. If the transducer is excited for N cycles, the pulse duration will be $\tau = NT$. The duty factor (DF) is defined as the time frequency of the pulse repetition period (PRP). The pulse repetition frequency (PRF) is the rate of pulse excitations, and given as the inverse of the PRP. The DF can then be expressed as [25]

$$\mathrm{DF} = \frac{\tau}{\mathrm{PRP}} = \tau \mathrm{PRF}. \tag{1.6}$$

In imaging, the PRF must be chosen in such a way that the scattering of the previous pulse from the desired imaging depth can be returned to the transducer before the next pulse is sent. The PRF is therefore limited by the desired depth of imaging.

1.3.2 The effect of ultrasound on microbubbles

US exposure can cause acoustic cavitation in tissue. In this context, cavitation can be defined as a process where gas bubbles which are already present in a liquid enlarge to MBs or start oscillating, forming bubbles due to pressure variations, or any other kind of bubble interaction resulting from acoustic pressure oscillations [24]. The phenomenon is usually divided into two different types: inertial and stable. Inertial cavitation is the rapid and uncontrolled growth of bubbles, eventually leading to collapse due to the backlash of inertia in surrounding tissue or fluid, while the second type refers to the oscillation of cavitation bubbles over many cycles without collapse. Additionally, bubble collapse can cause formation of tiny jet streams in the fluid which can have velocities of up to $100\,\mathrm{m\,s^{-1}}$, and symmetrical collapse of the bubble will focus the energy into a tiny volume compared to the original, causing an enormous local increase in pressure and temperature [26]. Acoustic cavitation can thus cause local heat accumulation, increased velocities of the surrounding fluid and shear forces on the tissue, which in turn can cause biological effects [23].

In order for a bubble to be formed in the first place, gas bubbles, also called cavitation nuclei, must be present in the tissue [7, 26]. During US exposure, the bubble oscillations will follow the variations in the pressure field. The probability

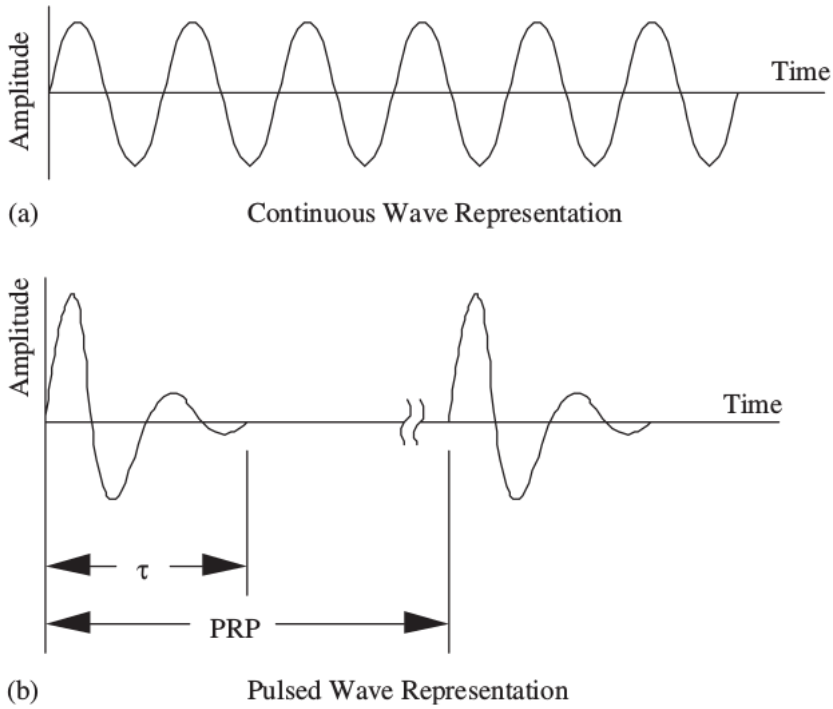

Figure 1.7: Schematics of waveforms for CW and PW US. (a) The transducer is excited continuously with a sinusoidal electric signal of constant frequency and amplitude, producing an US wave that exhibits the same frequency. (b) The transducer is excited for a pulse duration of τ, producing a pulse with a broader frequency bandwidth than the former case. A new pulse is created after a time PRP [25].

for bubble formation by inertial cavitation depends on the mechanical index (MI), which by itself is inversely proportional to the square root of US frequency [27], and defined as

$$\mathrm{MI} = \frac{p_{r,3}}{\sqrt{f}}, \tag{1.7}$$

where $p_{r,3}$ is the peak rarefaction pressure measured in MPa and f the frequency in MHz [25]. MI was developed as a simple relationship between the start of cavitation and acoustic pressure. For lower rarefaction pressures, and therefore lower MIs, gas oscillations are stable and result in micro-streaming and shear stresses on the tissue [28]. As MI increases, the bubble oscillations become unstable and finally lead to collapse.

1.3.3 Radiation force

US interactions can also be used to apply radiation force to the tissue [28]. When US passes through a material, the accompanying pressure gradient of the wave exerts a force on a volume of tissue or liquid which acts in the same direction as the wave propagation [22]. This force can result in several beneficial effects, such as the generation of acoustic streaming, improving convection in the ECM and additionally enhancing drug penetration and distribution by [28] by displacing the therapeutic agents away from the wave source [29]. Radiation force occurs in the direction of wave propagation and is proportional to the wave intensity, inversely proportional to the phase velocity, and also depends on the attenuation if the medium is absorbing [25].

The acoustic radiation force can have two different components working on the MBs, where primary radiation force is produced from the incident pressure field originating from the transducer. Secondary radiation force is produced by a field scattered from resonating MBs in the primary field [29]. The primary radiation force is linked with displacing the MBs causing accumulation on the endothelial wall, while the secondary type can cause bubble aggregation or dispersion, depending on the parameters of the applied US.

1.3.4 Thermal bioeffects in tissue

Focused US allows local tissue heating at a given depth with minimal temperature increases in the surrounding tissue. These thermal effects can at low intensities lead to heightened perfusion and changes in the drug carriers themselves. This can in turn facilitate the release of drugs from heat-dependent carriers, such as those based on liposomes or lipids, in a region of interest [23]. Additionally, the increases in heat can lead to a heightened EPR effect, which results in better drug extravasation and tissue diffusion [30]. The tissue becomes hyperthermic in temperature ranges of 40 °C to 45 °C, which acts as a powerful sensitizer for chemotherapy. Hyperthermia alters a host of biological effects which affect drug transport. Factors such as blood flow, perfusion, vascular permeability, drug accumulation and immune response is heightened by hyperthermia, while other factors such as IFP, hypoxia and DNA damage repair is lowered. Thus, the combination of heat-dependent carriers and hyperthermic effects can cause advantageous synergies [31].

1.3.5 Acoustic Cluster Therapy

US contrast MBs such as Sonovue^{TM} from Bracco Imaging S.p. A, Italy, or Optison^{TM} by GE Healthcare AS, Norway, have been used in conjunction with various drugs in experiments and clinical trials [32]. Such drug delivery approaches have shown promise, but are hampered due to the fact that these MBs are small

and free flowing the biomechanical work and effects are rather limited. Additionally, since MBs are cleared from the vascular system after a few minutes, high US intensities must be provide in on order to produce acceptable levels of biomechanical work and effects. Inertial effects can then occur with some safety issues.

Acoustic Cluster Therapy (ACT) is a novel concept in which negatively a charged MB is mixed with an oil microdroplet of opposite charge, forming clusters of MBs and microdroplets due to electrostatic attraction[33]. The size of these are in the range of 2 µm to 8 µm [34]. Drugs can be co-injected with the clusters or loaded into the microdroplets for targeted therapy. After injection, the procedure consists of local US activation followed by delivery enhancement [32]. The clusters can be activated by regular low MI medical US, with frequencies from 1 MHz to 10 MHz and MI < 0.4, which causes the MBs to act as cavitation nuclei. The application of US causes vibration of the MBs, transferring energy to the oil microdroplets, resulting in vaporization. This causes the formation of ACT bubbles with diameters of 20 µm to 30 µm, which transiently lodge into the local vasculature and hinders blood flow for up to a few minutes [33]. This has the effect of preventing local washout of the drug. The activated bubble will be in direct contact with a segment of the capillary wall, as the average diameter of capillaries in for example the lung are approximately 7 µm [34].

After activation, US with lower frequencies, such as 0.3 MHz to 1 MHz, induce controlled volume oscillations of these bubbles [33]. Bioeffects are generated and local permeability is enhanced in the tissue, causing improved drug distribution and extravasation in the tumor ECM [32]. By enhancing the EPR effect, drug accumulation is also enhanced, and the ACT concept has been shown to improve the uptake of both hydrophilic macromolecules and small hydrophobic molecules into the tumor. Additionally, drug distribution may be enhanced due to disruption in the ECM between tumor cells and due to induced shear forces and streaming [35] This effect increases drug specificity while reducing harm done to healthy tissue, increasing efficacy of the treatment. The process of ACT US activation and delivery enhancement is visualized in fig. 1.8.

While the mechanisms that result in enhanced drug accumulation are not fully understood, the ACT concept has shown promise as a technique for the delivery of different agents [35]. In one experiment, a group of mice were implanted with human prostate adenocarcinoma and treated with a combination of ACT with a chemotherapeutic drugs as Abraxane, and paclitaxel which has been bound to albumin and given intravenously. The survival rate after 120 days was 100 % vs. 0 % for the group that was treated only with Abraxane. ACT therefore was shown to induce a strong increase in the therapeutic efficacy of Abraxane [32]. Further investigation must be done in order to gain more understanding of the mechanisms behind this promising technique.

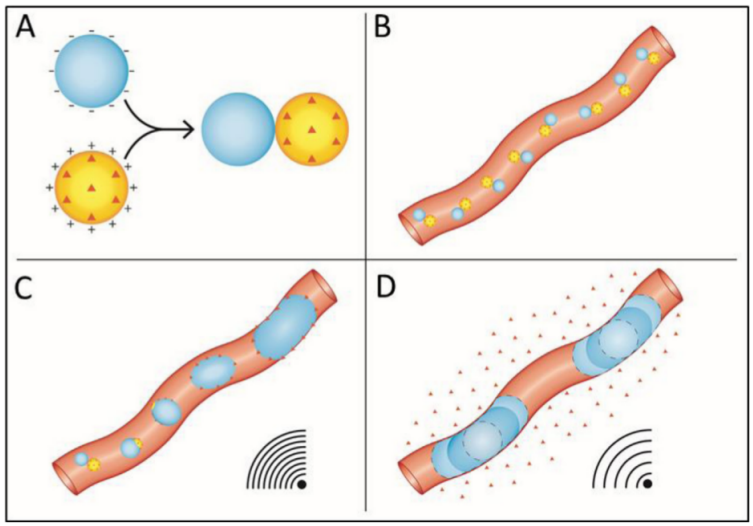

Figure 1.8: Visualization of ACT. A: Clusters are formed from MBs with negative charge and microdroplets of positive charge. The microdroplets can be loaded with drugs and therapeutic agents. B: The clusters flow freely in the blood stream after injection. C: Low MI medical US causes evaporation of the oil microdroplet, inducing the formation of bubbles from 20 µm to 30 µm in size. These lodge transiently into the vasculature and hinder blood flow, preventing local wash out of the drug. D: By applying a lower frequency US with low MI, controlled bubble volume oscillations are induced, generating bioeffects which improve extravasation and drug distribution in the the local tissue [33].

2 Theory

This chapter focuses on both the tissue-scale and pore-scale physics of NP transport in the ECM. The interstitium is modeled as a two-dimensional pore network model [36] where the cells are situated in a regular network. Sets of equations describing the fluid flow rate in both rigid and elastic pore networks will then be derived from the fundamental equations of fluid mechanics and elastic theory in biomechanics. These will be presented along with the equations governing the advective-diffusive transport of particles in the pores between cells. Finally, some attention is given to dimensional analysis of variables describing the transport problem and useful dimensionless numbers in fluid mechanics.

2.1 Pore networks

The interstitial space as shown in fig. 1.1 is investigated in a two-dimensional fashion. As the interstitial tissue is known to be irregular, in addition to cells being inside a complex ECM network, the interstitial model has to be greatly simplified. It is therefore assumed that the tumor has high collagen content and a well-organized interconnected collagen lattice, the cells in the ECM have fixed positions and are nondeformable. Each cell can then be approximated as a sphere surrounded by an incompressible interstitial fluid where the NPs are transported, as in fig. 1.5.

By representing the space between two cells as a link, and the intersection of three links as a node, the interstitial space can then be modeled as a regular hexagonal pore network in two dimensions, in a similar fashion as performed in [37], where links are connected together with nodes. All the links are rigid, have equal radii, and represent all the volume in the pore network. Liquid will flow through the links when a uniform pressure is applied over the pore network, and the flow in a single link depends on the pressure difference between the two nodes it is connected to [36]. The nodes are thus used to quantify the pressures in the network interior. A schematic illustration of a pore network can be seen in fig. 2.1

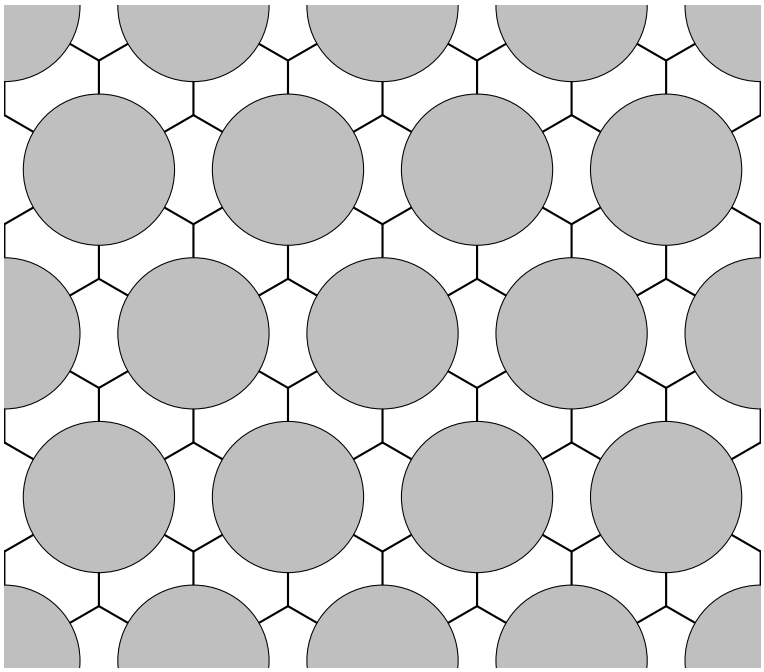

Figure 2.1: Schematic illustration of the tumor interstitium geometry as a hexagonal pore network. The gray spheres represent cells in the ECM which are engulfed by interstitial fluid. The empty white space between two cells represent the links, i.e. pores, of the network. The links are connected at nodes, where three links meet at an intersection. The nodes hold no volume, and the links thus represent the volume of both the pores and the throats.

2.1.1 Hagen–Poiseuille flow

In a similar fashion to the method described in [38], each link in the pore network, as seen in fig. 2.2a, is modeled by its average radius for simplicity. Each link is thus considered as a straight tube with a circular cross section $a = \pi R^2$ and length L, subjected to a pressure difference $\Delta p = p_2 - p_1$. A schematic can be seen in fig. 2.2b. This kind of laminar flow is known as Hagen–Poiseuille flow, and can be derived by the use of the Navier–Stokes momentum equations in three-dimensional cylindrical coordinates (r, θ, z).

The equations of motion for an incompressible viscous fluid [39, eq. 15.7] can be expressed as:

$$\frac{\partial \mathbf{u}}{\partial t} + \mathbf{u} \cdot \boldsymbol{\nabla} \mathbf{u} = -\frac{1}{\rho} \boldsymbol{\nabla} p + \frac{\mu}{\rho} \nabla^2 \mathbf{u}, \tag{2.1}$$

where $\mathbf{u} = (u_r, u_\theta, u_z)$ is the velocity field in cylindrical coordinates, ρ fluid density, μ absolute or dynamic viscosity and p fluid pressure.

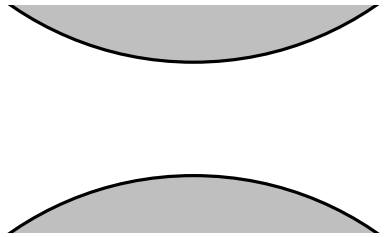

(a) A single pore in the network.

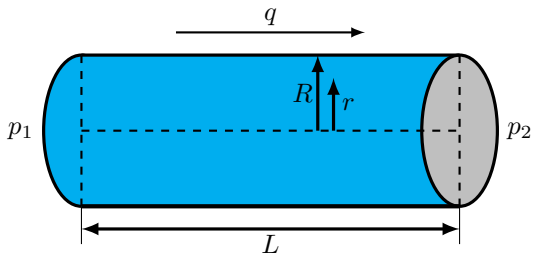

(b) The pore approximated as a cylindrical tube.

Figure 2.2: Schematic of a single pore situated between two spheres in the network (fig. 2.2a). The pore is approximated as a cylindrical tube of radius R subjected to a pressure difference of $\Delta p = p_2 - p_1$ which draws the flow rate q over the span of its length L. The cross-section of the tube has an area $a = \pi R^2$. (fig. 2.2b).

One can assume that the system has the following properties:

1. The flow is laminar along the z axis and fully developed.
   $u_r = u_\theta = 0,\ \partial_z u_z = 0,$

2. The flow is stationary.
   $\partial_t \mathbf{u} = 0,$

3. The flow is axisymmetric since the tube is cylindrical.
   $\partial_\theta \mathbf{u} = 0,$

4. The continuity equation for an incompressible fluid is satisfied.
   $\boldsymbol{\nabla} \cdot \mathbf{u} = 0,$

Since the tube has axial symmetry, all terms related to θ can be neglected. The defined model is in two dimensions, and the angular component θ can be set to zero. The spatial coordinates can now be expressed as $(r, \theta, z) \to (r, z)$.

Since the velocity is assumed to be constant along the tube axis, it only varies due to radial position in the cross section. Therefore, one can safely assume that

$u_z = u_z(r)$, with $r = 0$ in the tube center. eq. (2.1) can now be written as

$$\nabla^2 \mathbf{u} = \frac{1}{\mu} \boldsymbol{\nabla} p, \tag{2.2}$$

The partial derivative operators ∇ and ∇^2 in cylindrical coordinates and axial symmetry for a scalar function $f = f(r, z)$ are given as

$$\boldsymbol{\nabla} f = \frac{\partial f}{\partial r} \hat{\mathbf{e}}_r + \frac{\partial f}{\partial z} \hat{\mathbf{e}}_z, \qquad \nabla^2 f = \frac{\partial^2 f}{\partial r^2} + \frac{1}{r} \frac{\partial f}{\partial r} + \frac{\partial^2 f}{\partial z^2}. \tag{2.3}$$

By solving eq. (2.2) separately for each component in (r, z), two equations are yielded as

$$\partial_r p = 0, \tag{2.4a}$$

$$\frac{1}{\mu} \frac{\partial p}{\partial z} = \frac{1}{r} \frac{\partial}{\partial r} \left(r \frac{\partial u_z}{\partial r} \right). \tag{2.4b}$$

The expression eq. (2.4a) implies that $p = p(z)$, i.e. independent of r and the pressure varies only along the axis z. By solving eq. (2.4b) with respect to the velocity component u_z and integrating twice over r, the expression for axial velocity becomes

$$u_z = \frac{1}{4\mu} \frac{\partial p}{\partial z} r^2 + c_1 \ln(r) + c_2, \tag{2.5}$$

where c_1 and c_2 are integration constants. In order to determine these, two boundary conditions have to be established. The fluid velocity u_z has to be finite and well-defined at $r = 0$, and the no-slip condition at the tube wall for the viscous fluid implies that $u_z(R) = 0$. Mathematically, these boundary conditions are equivalent to

$$\lim_{r \to 0} \ln(r) = -\infty, \tag{2.6a}$$

$$\frac{1}{4\mu} \frac{\partial p}{\partial z} R^2 + c_2 = 0. \tag{2.6b}$$

In order for eq. (2.5) to be finite for $r = 0$, which is not the case in eq. (2.6a), the first integration constant has to be discarded. The second one is given from eq. (2.6b), and the integration constants are thus

$$c_1 = 0, \tag{2.7a}$$

$$c_2 = -\frac{1}{4\mu}\frac{\partial p}{\partial z}R^2. \tag{2.7b}$$

Finally, by substituting the integration constants in eqs. (2.7a) to (2.7b) into eq. (2.5), an expression for the parabolic velocity profile is yielded:

$$u_z(r) = \frac{-1}{4\mu}\frac{\partial p}{\partial z}(R^2 - r^2). \tag{2.8}$$

The equation is prepended with a negative sign since it is assumed that the pressure drops across the length of the tube, i.e. $\partial_z p < 0$. For a given axial direction, a negative pressure gradient is therefore equivalent to positive flow velocity. The flow rate in the tube can be found by integrating the velocity profile in eq. (2.8) across the cross section of the tube in polar coordinates. This can be expressed as

$$\begin{aligned} q &= \int_0^R u_z(r) dA \\ &= \frac{-1}{4\mu}\frac{\partial p}{\partial z}\int_0^R \left(R^2 - r^2\right) 2\pi r dr \\ &= \frac{-\pi R^4}{8\mu}\frac{\partial p}{\partial z} \end{aligned} \tag{2.9}$$

The pressure gradient can be approximated and rewritten in terms of system properties related to the tube itself as

$$\frac{\partial p}{\partial z} \approx \frac{\Delta p}{L}. \tag{2.10}$$

Inserting eq. (2.10) into eq. (2.9) yields the final expression for Hagen–Poiseuille flow

$$q = \frac{-\pi R^4}{8\mu L}\Delta p = -g\Delta p, \tag{2.11}$$

where g is the link mobility of the tube, which only depends on the tube geometry and fluid viscosity. A negative pressure difference over the tube length, i.e. $\Delta p < 0$, mean that the flow is positive along the direction of the pressure drop.

2.1.2 Elastic links

Consider the network in section 2.1. That kind of network had fixed tube radii, constant for all pressures. Now, consider that the radius at a given time is dependent on the current pressure in the tube. This can be investigated for a thin-walled cylinder of radius r and wall thickness $t \ll r$, where the azimuthal strain ϵ_θ of the cylinder is related to its radial change [40, eq. (4.45)]

$$\epsilon_\theta = \frac{r - r^0}{r^0}, \tag{2.12}$$

where r^0 is the radius at some reference pressure p^0. The azimuthal strain is given as [40, eq. (4.44)]

$$\epsilon_\theta = \frac{1 - \nu_{\text{cyl}}}{E}\sigma_\theta, \tag{2.13}$$

where ν_{cyl} is Poisson's ratio, defined as the ratio of transverse contraction strain and longitudinal strain, E Young's modulus of the tube wall and σ_θ the hoop stress. The two latter quantities have units $[E] = [\sigma_\theta] = \text{Pa}$. For a thin-walled cylinder, the hoop stress σ_θ is given as [40, eq.(2.168)]

$$\sigma_\theta = \frac{\left(p - p^0\right) r}{\delta} \tag{2.14}$$

where p is the pressure inside the cylinder and δ the wall thickness. By inserting eqs. (2.13) to (2.14) into eq. (2.12), the local tube radius is related to the local pressure as

$$r = r^0 + rr^0 \frac{(1 - \nu_{\text{cyl}})}{E\delta}\left(p - p^0\right), \tag{2.15}$$

By assuming small radial deformations and thin walls, the thickness t of the wall and length L of the cylinder are constant. Thus there is no radial or axial strain of the cylinder, which can act as transverse strains to the azimuthal, longitudinal strain under scrutiny, such that $\nu_{\text{cyl}} \approx 0$. The expression in eq. (2.15) can then be approximated as

$$r \approx r^0 + \frac{(r^0)^2}{E\delta}\left(p - p^0\right). \tag{2.16}$$

A high pressure will expand the tube radially, and a lower pressure contracts it. Due to volume conservation, the change in flow rates in and out of the tube is related to the change in tube volume as

$$\frac{\partial V}{\partial t} + \Delta q = 0, \tag{2.17}$$

where V is the link volume and Δq the flow rate difference in the link. A positive volume rate change is equivalent to a negative flow rate difference, i.e. the tube expands and less flows out than in. The tube is a cylinder, and by application of the chain rule, the volume term in eq. (2.17) can be expressed as

$$\begin{aligned} \frac{\mathrm{d}V}{\mathrm{d}t} &= \pi L \frac{\mathrm{d}r^2}{\mathrm{d}t} \\ &= 2\pi r L \frac{\mathrm{d}r}{\mathrm{d}t}, \end{aligned} \tag{2.18}$$

where the radial time derivative is found from eq. (2.16) as

$$\frac{\mathrm{d}r}{\mathrm{d}t} = \frac{(r^0)^2}{E\delta} \frac{\mathrm{d}p}{\mathrm{d}t}. \tag{2.19}$$

The change in rube radius thus depends on how the pressure p varies over time. By inserting eq. (2.19) into eq. (2.18), the volume conservation equation now becomes

$$\Delta q = -2\pi r L \frac{(r^0)^2}{E\delta} \frac{\mathrm{d}p}{\mathrm{d}t}. \tag{2.20}$$

This equation can be understood by the time evolution of the pressure. If $\partial_t p < 0$ in the link, then $\Delta q > 0$, which is equivalent to radial expansion and reduced flow through the link over time.

2.2 Particle motion

Transport of mass within the interstitium is facilitated by both diffusion and advection [14]. The expression for concentration of particles C in the interstitial fluid satisfies a convection-diffusion equation [41, eq. (9.33)] of the form

$$\frac{\partial C}{\partial t} + \mathbf{u} \cdot \boldsymbol{\nabla} C = D\nabla^2 C + Q(t, x, y, \mathbf{u}, C), \tag{2.21}$$

where Q is a source term which depends on time, location, velocity and concentration. The diffusion coefficient D is valid for a particle in free solution [14]

$$D = \frac{k_\mathrm{B} T}{6\pi\mu d_p}, \tag{2.22}$$

where k_B is the Boltzmann constant, T absolute temperature and d_p particle diameter. By considering the equation in one dimension along an axis x with no source term, eq. (2.21) is rewritten as

$$\frac{\partial C}{\partial t} + u\frac{\partial C}{\partial x} = D\frac{\partial^2 C}{\partial x^2}. \tag{2.23}$$

By insertion it can be shown by insertion that a possible solution to eq. (2.23) is

$$C(x,t) = \frac{C_0'}{\sqrt{4\pi D t}} \exp\left\{ \frac{-(x - ut - x_0)^2}{4Dt} \right\}, \tag{2.24}$$

which is a Gaussian function with a mean at the variable position

$$\mu_x = ut + x_0, \tag{2.25}$$

which must not be misinterpreted with the viscosity μ_0. The variance is

$$\sigma_x^2 = 2Dt. \tag{2.26}$$

C_0' is a measure of the initial particle concentration and u the flow velocity of the interstitial fluid surrounding the particle. The flow velocity depends on changes in the IFP or other pressure gradients presents in the interstitium.

2.2.1 Treatment time

As seen in the expressions for mean and variance in eqs. (2.25) to (2.26) for the advection-diffusion equation in eq. (2.24), the mean increases linearly with time,

and the standard deviation with the square root of time. This means that the contribution from the diffusion will be larger than the advection before a certain time limit. Since a point of interest is transport by advection, the time t_{adv} at which diffusion no longer dominates can be found by solving the inequality of eqs. (2.25) to (2.26) with $x_0 = 0$ as

$$\begin{aligned} &\mu_x > \sigma_x \\ \implies &t_{\text{adv}} > \frac{2D}{u^2}. \end{aligned} \tag{2.27}$$

The time criterion in eq. (2.27) will depend on multiple parameters, and will thus change as some parameters is changed. In animal trials, the exposure time of US have been of upwards to five minutes [32, 35]. One crucial question to ask is if the time used in this experimental setting is sufficiently long enough to ensure a facilitated increase in particle transport from US exposure.

2.3 Dimensional analysis

The advantages of using dimensionless variables are apparent, since there is no need to keep track of the units when performing mathematical calculations, in addition to the convenience of expressing variables in orders of magnitude that can be more easily related to. The author refers to appendix B for a comprehensive approach. For the Hagen–Poiseuille flow, eq. (2.11), the variables can be written in dimensionless form by using the characteristic length L_0, density ρ_0 and dynamic viscosity μ_0, such as

$$L = L' L_0, \tag{2.28a}$$
$$R = r' L_0, \tag{2.28b}$$
$$\mu = \mu' \mu_0, \tag{2.28c}$$
$$\Delta p = \Delta p' \Delta p_0 = \Delta p' \frac{\mu_0^2}{\rho_0 L_0^2}, \tag{2.28d}$$
$$q = q' q_0 = q' \frac{L_0 \mu_0}{\rho_0}, \tag{2.28e}$$
$$t = t' t_0 = t' \frac{L_0^2 \rho_0}{\mu_0}, \tag{2.28f}$$
$$\tag{2.28g}$$

where the variables with an apostrophe, such as L', indicate the dimensionless variable and subscript 0 the equivalent dimensional factor. Now it is possible to trans-

form each variable from a dimensional form to a dimensionless form, and vice versa. For example, by inserting the dimensionless variables in eqs. (2.28a) to (2.28e) into eq. (2.11), the dimensionless Hagen–Poiseuille flow is written as

$$q' = \frac{-\pi r'^4}{8\mu' L'} \Delta p' = -g' \Delta p'. \tag{2.29}$$

The dimensionless quantities or variables can then be converted back into dimensional form after the required calculations have been performed.

2.4 Dimensionless numbers

Ratios of quantities with dimensions, but whose units cancel out to yield a dimensionless number, such as the Reynolds and Péclet numbers, are common in for example fluid mechanics. Some dimensionless groups can therefore be thought of as ratios between different effects or forces in the system, and by using characteristic variables, the ratios can be calculated in rough orders of magnitude to for example determine the dominating effect in the system [42, p. 355].

2.4.1 Reynolds number

For a flow determined by eq. (2.1), the dimensionless Reynolds number Re represents the relative ratios of inertial and viscous forces in fluid flow [41, p. 19]. By representing the mathematical operators in these terms with characteristic variables, one gets

$$\text{Inertial} : \mathbf{u} \cdot \nabla \mathbf{u} \sim u_0 \frac{\mathbf{u}}{L_0}, \tag{2.30a}$$

$$\text{Viscous} : \frac{\mu}{\rho} \nabla^2 \mathbf{u} \sim \frac{\mu_0}{\rho_0} \frac{\mathbf{u}}{L_0^2}, \tag{2.30b}$$

where L_0, ρ_0 and μ_0 are the characteristic variables of the system as shown in a previous section, and u_0 some characteristic velocity. By using the terms defined in eqs. (2.30a) to (2.30b), the quantity can be written as

$$\text{Re} = \frac{\text{inertial force}}{\text{viscous force}} = \frac{L_0 \rho_0 u_{\max}}{\mu_0}, \tag{2.31}$$

which will be a dimensionless number. For the sake of the simulations, the characteristic velocity used in eq. (2.31) is the maximum fluid velocity in the pore network, defined as

$$u_{\max} = \max_{ij} \left(\frac{q_{ij}}{a_{ij}} \right), \tag{2.32}$$

where $a_{ij} = \pi r_{ij}^2$ is the tube cross section of link ij. An important assumption in the derivation of eq. (2.29) is that the flow is laminar along the tube z axis and fully developed. The Reynolds number is therefore a useful quantity to investigate, since the flow starts to become turbulent once a certain critical Reynolds number, such as $\mathrm{Re} \approx 2.34 \times 10^3$ for pipe flow, has been reached [41, p. 155]. The flow will then not be laminar anymore and the assumption invalid. The maximum fluid velocity in the network is there chosen in order to determine if the inertial forces can be of significance, and thus if the assumption of laminar flow is upheld.

2.4.2 Péclet number

The movement of the particles depends on both an advective and diffusive term. The Péclet number is defined as the dimensionless ratio between advective and diffusive contributions to the transport [14]. Similar to the derivation of the Reynolds number, the mathematical operator of each relevant term in eq. (2.23) can be represented with characteristic variables as

$$\text{Advective} : u\frac{\partial C}{\partial x} \sim u_0 \frac{C}{L_0}, \tag{2.33a}$$

$$\text{Diffusive} : D\frac{\partial^2 C}{\partial x^2} \sim D\frac{C}{L_0^2}. \tag{2.33b}$$

By using eqs. (2.33a) to (2.33b), the Péclet number is written as

$$\mathrm{Pe} = \frac{\text{advective transport rate}}{\text{diffusive transport rate}} = \frac{L_0 u_{\min}}{D}, \tag{2.34}$$

which will also be a dimensionless number. The characteristic velocity is now defined as

$$u_{\min} = \min_{ij} \left(\frac{q_{ij}}{a_{ij}} \right), \tag{2.35}$$

where q_{ij} is the average flow rate through the cross section a_{ij} of link ij. The Péclet number is useful to investigate in order to determine whether the simulated flow rates in the network are of a sufficient magnitude to improve transport in comparison with diffusion only. For the cases where $\mathrm{Pe} < 1$, the diffusive contribution is larger than the advective, and vice versa when $\mathrm{Pe} > 1$. The minimum fluid velocity in the pore network is therefore chosen to determine how significant the largest contribution from diffusion is in comparison to the fluid flow rate.

3 Methods

In this chapter, the sets of equations for both types of pore networks as presented in chapter 2 will be discretized with regards to the nodes. The pore network is based on the rectangular network seen in [36] with extensions into a hexagonal pore network by [37]. The basic building blocks and rules of the pore network is given to relate the nodes and links. To account for the different properties of the pore networks, systems of linear equations describing the discrete pressures will be displayed. Stochastic modeling of NP transport is also presented by analyzing the behavior of individual particles on the pore-scale. In the end, the procedures of the aforementioned parameter study, which aims to establish relations between system properties on the pore-scale to particle transport on the tissue-scale, is laid out.

3.1 The pore network model

By representing the links in fig. 2.1 with cylindrical tubes as described in fig. 2.2b, the porous medium can be represented as a hexagonal lattice network of N nodes connected by M links, where each node is given an index $i \in [0, N-1]$. The nodes are simply described as points, and all volume contributions to the network are therefore contained in the links, which are identified by the connected node indices.

The size of an open hexagonal network is defined by the number of rows and columns in the interior, n_x and n_y. Additionally, the boundaries at the top and bottom each have $n_x/2$ nodes, yielding a total of $N = n_x(n_y+1)$ nodes for an open network. In the interior, a row contains n_x repeating units, each with exactly one node. A single repeating unit has the geometric properties

$$dx = L\cos 30°, \tag{3.1a}$$
$$dy = L + dY = L(1+\sin 30°), \tag{3.1b}$$

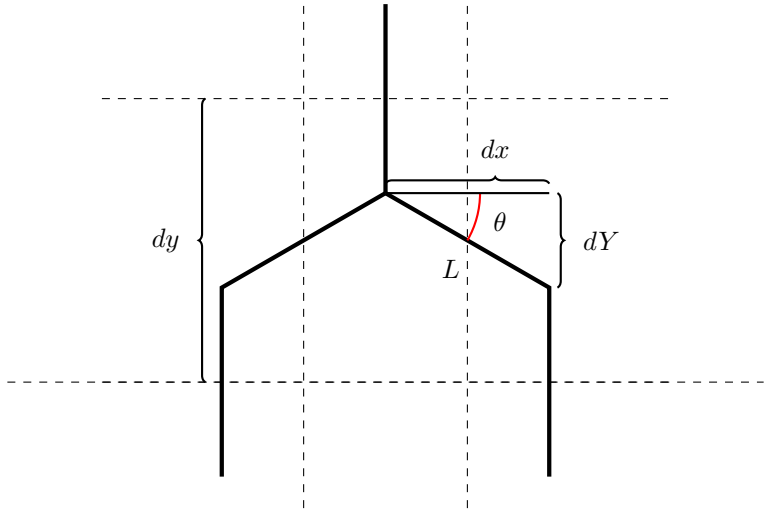

Figure 3.1: Schematic of a single unit with exactly one node contained within the dashed lines in a row in the pore network model. $dY = L\sin 30°$ signifies the opposite side of the angle θ, $dy = L + dY = L(1 + \sin 30°)$ the total height of the unit, $dx = L\cos 30°$ the width and double the length from the node at the center of the unit to either vertical dashed line. Consecutive repeating units in the same row are flipped vertically in comparison to the previous unit. Since the node in this unit is situated in the upper half of the unit, the next and previous units will have their nodes in the lower half, etc, owing to the hexagonal pattern of the network.

as width and height, respectively, as seen in fig. 3.1. For consecutive repeating units in the same row, the next unit is flipped vertically in comparison to the previous unit, owing to the hexagonal pattern of the network. Additionally, each node has three unique neighbors except at the top and bottom boundaries, where the number of neighbors is one. These properties will be used when calculating the positions of all nodes and links.

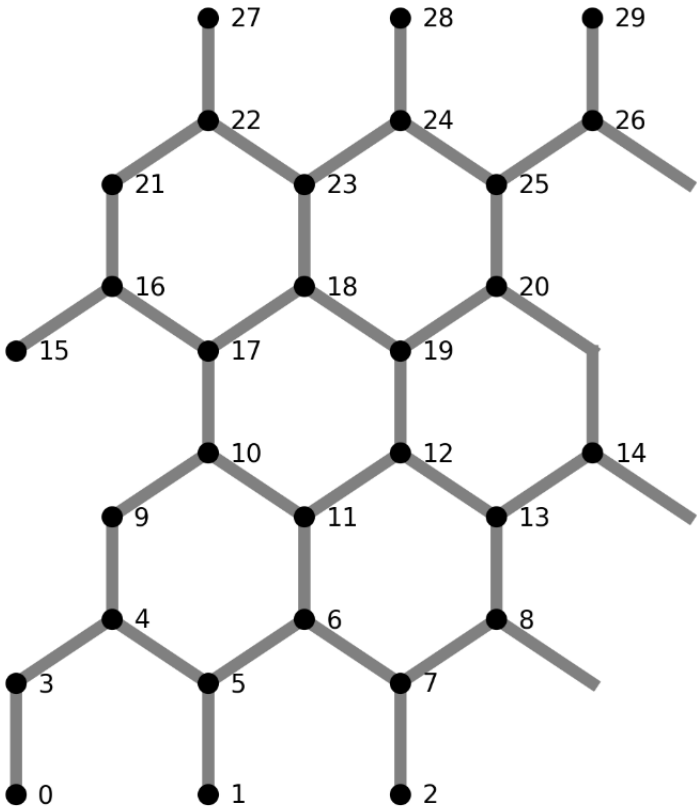

Figure 3.2: Schematic illustration of a pore network model with $n_x = 6$, $n_y = 4$, and $N = 30$ nodes. Nodes are represented as points, and links as the lines connecting two points. Links with unconnected ends wrap around horizontally, such node 14 connected to node 9. For the internal rows, the first spans over nodes 3 to 8 and the last from node 21 to 26. Note that the link lengths and diameters are not up to scale.

For these kinds of networks, the very first row of nodes $i \in [0, n_x/2 - 1]$ is usually called an inlet row where the same fixed pressure is applied. The very last row of nodes $i \in [N - n_x/2, N - 1]$ is called an outlet row, usually with node pressures fixed at zero [43]. In dynamic pore network models it is therefore common and numerically straightforward to implement constant pressures as Dirichlet boundary conditions [44]. Periodic boundary conditions are applied horizontally [36], and the network therefore wraps as a torus in the x-direction as seen in fig. 3.2.

3.2 Rigid network

The flow of each link in a pore network, such as the one illustrated in fig. 3.2, has to be determined in order to calculate the total flow in the network. The flow in one link can be calculated by omitting the apostrophes in the dimensionless Hagen–Poiseuille flow, eq. (2.29), for simplicity, the equation can be expressed as

$$q_{ij} = -g_{ij}(p_i - p_j). \tag{3.2}$$

Here the index i indicates the current node and $j \neq i$ a neighboring node. The flow q_{ij} therefore indicates the fluid flow from node j to i, and g_{ij} the mobility of the link ij which connects these two nodes. If the pressure is larger in node j than in node i, the pressure difference is negative and the flow positive.

Since the fluid is incompressible, mass conservation implies that net flow into a node i from all its neighbors j has to be zero, i.e. the net flow in cannot be larger than net flow out, and vice versa. Hence, the equation that needs to be solved is the conservation of fluid flux passing through each node [43], which for a single node i is expressed by Kirchhoff's equation as

$$\sum_j q_{ij} = 0. \tag{3.3}$$

By switching the order of indices such that $ij \to ji$, some properties of the network flow can be investigated. The link mobilities will be symmetric, as they are a scalar property of the link which connects two nodes, and independent of flow direction. The following statement is equivalent to

$$g_{ij} = g_{ji}. \tag{3.4}$$

By switching indices in eq. (3.2) and using the property in eq. (3.4), this results in the following property for the flow as

$$q_{ij} = -q_{ji}, \tag{3.5}$$

which means that the flow in a given link changes sign when viewed from the opposite direction.

The flow in eq. (3.2) for a given link can be calculated once the relevant pressures are known. Since the node pressures at inlet and outlet rows are known and serve

as Dirichlet boundary conditions, the pressure of all nodes in the network can be determined. To solve the equations with respect to the pressures, the dimensionless flow expression in eq. (3.2) can be inserted into eq. (3.3), yielding

$$\sum_j g_{ij}(p_i - p_j) = p_i \sum_j g_{ij} - \sum_j g_{ij} p_j = 0, \tag{3.6}$$

which means that for a given node i, the product of its pressure and the sum of mobilities for neighbouring links, and the sum of products of pressures at the neighbouring nodes and corresponding mobilities, has to be equal in order for the condition for mass conservation to be preserved. By solving with respect to pressure, eq. (3.6) can be expressed as a matrix equation

$$A\mathbf{x} = \mathbf{b}, \tag{3.7}$$

where the matrix is of size $N \times N$. The column vector $\mathbf{x} = [p_0, ..., p_{N-1}]^T$ of size $N \times 1$ contains the node pressures and $b_i = 0$ except at the inlet rows, where the pressure is given as a finite boundary condition. The matrix components for the inlet and outlet nodes are given as $A_{ij} = \delta_{ij}$ and $b_i = P$, where P is the boundary pressure at the inlet row and set to zero at the outlet row. Each matrix element for the network interior is given as

$$A_{ij} = \delta_{ij} \sum_k g_{ik} - (1 - \delta_{ij}) g_{ij}. \tag{3.8}$$

Once eq. (3.7) is solved, by using methods such as LU decomposition, the flow rate can finally be calculated for each link by inserting the computed node pressures into eq. (2.29). The bulk-averaged flow velocity in some link ij can then be computed as

$$u_{ij} = \frac{q_{ij}}{a_{ij}}, \tag{3.9}$$

where q_{ij} is the calculated flow rate in the link and a_{ij} its cross section. The pressures of all nodes and flow rates of all links in the network can thus be determined when the boundary conditions are known.

3.2.1 Particle transport

For convenience it can be more advantageous to consider the particle distribution as a number of individual particles rather than a concentration C in eq. (2.24). The

concentration can then be approximated as the distribution of particle positions rather than dividing the pore network, and therefore the individual links, into a number of cells where the particle concentration must be computed for each individual cell. By assuming that the particle velocity within a link is equal to that the streamline of the link, the particle positions will then evolve over time by advection, in addition to a random walk where the particle can randomly move a small distance.

The properties of the Gaussian in eq. (2.24) can be analyzed in order to investigate the behavior of an individual particle undergoing diffusion modeled as a random walk by evolving the system over one time step as $t \to t + \Delta t$. The mean change in position x over that time step can be expressed [45, p. 201] as

$$\frac{\langle \Delta x \rangle_x}{\Delta t} = u, \tag{3.10}$$

which means that the mean change of the position in the next Δt depends on the velocity u of the fluid surrounding the particle. The mean change in variance of x in the next timestep is given [45, p. 201] as

$$\frac{\langle (\Delta x)^2 \rangle_x}{\Delta t} = 2D, \tag{3.11}$$

and the macroscopic diffusion coefficient is then coupled with the microscopic random jumps of the particle. The change in position resulting from advection or diffusion respectively can thus be described as

$$\Delta x_{\text{adv}} = \langle \Delta x \rangle_x = u \Delta t, \tag{3.12a}$$

$$\Delta x_{\text{diff}} = \sqrt{\langle (\Delta x)^2 \rangle_x} = \sqrt{2D\Delta t}. \tag{3.12b}$$

The total change Δx in position for the timestep Δt for a single particle can therefore be written as the sum of eqs. (3.12a) to (3.12b) as

$$\Delta x = x_{\text{adv}} + s\Delta x_{\text{diff}} \tag{3.13}$$

The first term in eq. (3.13) can be thought of as the mean change in particle position, and the second as the standard deviation of that change, where s is drawn from the normal distribution $N(0, 1)$, which a has a mean of zero and standard deviation of 1. A new s is drawn from the distribution for each time the particles

moves a single step in order to approximate the particle diffusion as a random walk. The particle can jump a diffusive step in either direction along axis, with lower probability for longer jumps. The flow velocity is the bulk-averaged flow velocity as defined in eq. (3.9).

To update the particle position at each iteration, the time step can be chosen similarly to the method described in [37], in such a way that the contributions from the advective and diffusive terms in *eq.* (3.13) is guaranteed to be less than or equal to a maximum spatial step, i.e. $\Delta x_{\text{adv}} = \Delta x_{\text{diff}} = \Delta x_{\max}$. The minimum time step that satisfies this constraint is found by rewriting each term in eqs. (3.12a) to (3.12b) with respect to time, as

$$\Delta t = \frac{1}{\tau} \min_{ij} \left(\Delta t_{\text{adv}}, \Delta t_{\text{diff}} \right) = \frac{1}{\tau} \min_{ij} \left(\frac{\Delta x_{\max}}{u_{ij}}, \frac{(\Delta x_{\max})^2}{2D} \right), \tag{3.14}$$

where τ is a scaling factor. The number s for the random walk is in eq. (3.14) set to $s^2 = 1$. Note that the minimum time step depends on the maximum local fluid velocity in a link.

When a particle reaches the end of the current link and comes upon a node, a new link has to be chosen in order for the particle to propagate further into the pore network. For the advection step, links with flow rates away from the current node are eligible for selection, and this process depends on the flow rates for the selection of next possible links, which are drawn from a weighted probability distribution proportional to their flow rates. For the diffusion step, the particle can go to any link connected to the node except the current one.

3.3 Elastic network

The theory in section 2.1.2 describes how time evolution of pressure is related to radial expansion and contraction of the link, and hence the flow rate difference. As described in section 2.1, the nodes of the pore network are used describe the pressure, not the link. To discretize the equations for the elastic network, the link pressures must then be expressed in terms of the node pressures. For this problem, the arithmetic mean is chosen to approximate the link pressure as

$$p_{ij} \approx \frac{1}{2} \left(p_i + p_j \right), \tag{3.15}$$

and the pressure inside link ij is thus the mean of the pressures of its corresponding nodes i and j. Inserting eq. (3.15) into eq. (2.20) now yields

$$\Delta q_{ij} = -\pi r_{ij} L \frac{(r_{ij}^0)^2}{E\delta} \left(\frac{\mathrm{d}p_i}{\mathrm{d}t} + \frac{\mathrm{d}p_j}{\mathrm{d}t} \right) = -h_{ij} \left(\frac{\mathrm{d}p_i}{\mathrm{d}t} + \frac{\mathrm{d}p_j}{\mathrm{d}t} \right), \tag{3.16}$$

where Δq_{ij} is the flow rate difference of link ij and h_{ij} a factor related to the geometry and radial elasticity of the link. The discretized flow rate difference can also be written as

$$\Delta q_{ij} = {}_i q_{ij} - {}_j q_{ij}, \tag{3.17}$$

where the first subindex denotes whether whether the flow rate at the link end closest to the link i or furthest away, j, of the given link ij. The node pressures for some node labeled with index k are discretized in time as

$$\frac{\mathrm{d}p_k}{\mathrm{d}t} \approx \frac{p_k^{(n+1)} - p_k^{(n)}}{\Delta t}, \tag{3.18}$$

where (n) is the current timestep where the values of all quantities are known and $(n+1)$ the next timestep which has to be solved for. The final discrete equation for the flow rate difference is found by inserting eq. (3.18) into eq. (3.16).

$$\Delta q_{ij}^{(n+1)} = -h_{ij}^{(n)} \left(\frac{p_i^{(n+1)} - p_i^{(n)}}{\Delta t} + \frac{p_j^{(n+1)} - p_j^{(n)}}{\Delta t} \right). \tag{3.19}$$

The change in flow rate due to volume change in a link has now been examined. For Hagen-Poiseuille flow, the flow rate in a tube occurs due to the pressure drop over it. In the case of elastic tubes, only the flow rate at the tube ends are known. Similar to the link pressure in eq. (3.15), the link flow is approximated as the arithmetic mean of the flow rates in the back and front.

$$q_{ij}^{(n+1)} = \frac{1}{2} \left({}_j q_{ij}^{(n+1)} + {}_i q_{ij}^{(n+1)} \right), \tag{3.20}$$

The expression for Hagen-Poiseuille flow in eq. (2.11) can thus be written as

$$\frac{1}{2} \left({}_j q_{ij}^{(n+1)} + {}_i q_{ij}^{(n+1)} \right) = -g_{ij}^{(n)} \left(p_i^{(n+1)} - p_j^{(n+1)} \right) \tag{3.21}$$

Since the flow rate difference is defined as $\Delta q_{ij} = {}_i q_{ij} - {}_j q_{ij}$, eq. (3.21), with either a front or back flow rate as

$$ {}_jq_{ij}^{(n+1)} = -\, g_{ij}^{(n)} \left(p_i^{(n+1)} - p_j^{(n+1)} \right) - \frac{\Delta q_{ij}^{(n+1)}}{2}, \tag{3.22a} $$

$$ {}_iq_{ij}^{(n+1)} = -\, g_{ij}^{(n)} \left(p_i^{(n+1)} - p_j^{(n+1)} \right) + \frac{\Delta q_{ij}^{(n+1)}}{2}, \tag{3.22b} $$

where Δq_{ij} is the same as in eq. (3.19). The physical meaning of these flow rates is similar to that of the discrete Washburn equation in eq. (3.2), with an extra term proportional to $\mp \Delta q_{ij}^{(n+1)}$ added. By switching indices as $ij \rightarrow ji$, the elastic geometric factor will be symmetric, since it only depends on the tube properties for the tube of the given link, which is equivalent to

$$ h_{ij} = h_{ji}. \tag{3.23} $$

By index switching of the flow rate difference in eq. (3.19), one can easily see that

$$ \Delta q_{ji}^{(n+1)} = \Delta q_{ji}^{(n+1)}. \tag{3.24} $$

As in the previous section, the fluid is incompressible and mass conservation implies that net flow into a node i from all its neighbors j has to be zero and net flow in must be equal to net flow out.

$$ \sum_j {}_iq_{ij}^{(n+1)} = 0. \tag{3.25} $$

This condition has to be valid for all timesteps $(n+1)$. By insertion the expression for the flow rate going into node i eq. (3.22b) into eq. (3.25), the following expression is yielded

$$ p_i^{(n+1)} \sum_j \left(g_{ij}^{(n)} + \frac{h_{ij}^{(n)}}{2\Delta t} \right) - \sum_j \left(g_{ij}^{(n)} - \frac{h_{ij}^{(n)}}{2\Delta t} \right) p_j^{(n+1)} = p_i^{(n)} \sum_j \frac{h_{ij}^{(n)}}{2\Delta t} + \sum_j \frac{h_{ij}^{(n)}}{2\Delta t} p_j^{(n)} \tag{3.26} $$

By summing over all neighbors j and for a given node i with the flow rates of the corresponding links ij, and collecting all pressure terms for the next timestep $p_i^{(n+1)}$ on the left hand side and all known pressures $p_i^{(n+1)}$ on the right hand side, the system of equations can be written as a matrix equation

$$A\mathbf{x} = \mathbf{b}, \tag{3.27}$$

where $\mathbf{x} = [p_0^{(n+1)}, ..., p_{N-1}^{(n+1)}]^T$ is a column vector of size $N \times 1$ containing the node pressures. The matrix is of size $N \times N$. At the boundaries, where the initial pressures are known, the matrix components for some node can be given as $A_{ij} = \delta_{ij}$ and $b_i = P$, equivalent to $p_i^{(n+1)} = P_{n+1}$, where P_{n+1} is finite at the inlet row and zero at the outlet. All other elements in A are given as

$$A_{ij} = \delta_{ij} \sum_{ij} \left(g_{ij}^{(n)} + \frac{h_{ij}^{(n)}}{2\Delta t} \right) - (1 - \delta_{ij}) \left(g_{ij}^{(n)} - \frac{h_{ij}^{(n)}}{2\Delta t} \right), \tag{3.28}$$

and b_i an element of the vector on the right hand side of eq. (3.27) which contains the pressures for the current time, given as

$$b_i = p_i^{(n)} \sum_j \frac{h_{ij}^{(n)}}{2\Delta t} + \sum_j \frac{h_{ij}^{(n)}}{2\Delta t} p_j^{(n)}. \tag{3.29}$$

The matrix equation eq. (3.27) can then be solved by using the system properties at timestep (n) to obtain the node pressures for the next timestep $(n+1)$.

The oscillating boundary condition for the inlet row nodes is set to resemble the vibrating MB in the capillary as

$$P_n = \begin{cases} A_p \sin(2\pi f_p t_n), & t_n \leq t_p \\ 0, & t_n > t_p \end{cases} \tag{3.30}$$

where A_p is its amplitude, f_p the oscillation frequency, t_n the current time at timestep (n) and t_p a cutoff time at which the boundary condition is zero.

3.4 Parameter studies

To analyze how the transport of NPs in the rigid pore network depend on different input parameters, a parameter study has to be conducted. In this context, a parameter study is multiple simulation runs where all system parameters are fixed except one. That single parameter is then varied to see how the transport of particles change in regard to that variation. A variety of parameters can be chosen. The parameter study in this thesis specifically looks at at interstitial fluid viscosity

μ_0, link diameter d_l, US-induced pressure gradient $\Delta P_u/L_y$, diffusion coefficient D and maximum exposure time $t_{\max}$.

The transport is modeled stochastically by analyzing the vertical position distribution of independent particles over time in the network. The particles can thus not collide with each other. In order to simulate the movement through the pore network, the starting positions of the particles is chosen to be vertically a certain distance into the network at $t = 0$. The initial starting position and distribution can thus be thought of as a Delta function,

$$C(x_0, 0) = C_0' \delta(x_0), \tag{3.31}$$

where x_0 denotes the vertical starting position. At the start of every run, the matrix equation for the rigid network eq. (3.7) is solved to obtain the node pressures. The flow rate is then calculated from eq. (2.29) and the simulation time step from eq. (3.14). The particles are then transported until the time $t_{\max}$ has been reached. Since the particles are subject to the advection-diffusion equation in eq. (2.24), the starting position is subtracted, and the mean transport, hereby referred to as particle penetration depth (PPD), is calculated. The standard deviation σ_x of the particles, eq. (2.26), can be calculated from the spread of positions. This procedure is performed for every variation of the current parameter being studied.

3.5 Base case parameters

The following section lists the base case parameters used in the parameter studies. Unless other values are explicitly presented, these parameters will be the default for all the simulations. An overview of parameter names, symbols, values, units and references is summarized in table 3.1.

The number of particles are set to 10000, while the number of columns and rows in the particle are 22 and 40, corresponding to a width of 40 µm and depth of 300 µm. The cell diameter is roughly $d_c = 10\,\mu\text{m}$. As cells in the pore network are approximated to be a regular hexagon, which can be divided into six equilateral triangles, the length of each triangle side and therefore links is half of that, $L_0 = 5\,\mu\text{m}$ [46]. Assuming that the pores sizes of the network are comparable to that of a collagen gel, the pore sizes have been found to be 500 nm and 100 nm for $2\,\text{mg}\,\text{ml}^{-1}$ to $20\,\text{mg}\,\text{ml}^{-1}$ of collagen, which is comparable to collagen content in the tumor ECM [19]. Based on the range of these numbers, the link diameter dl is chosen to be 200 nm for a tumor with relatively high collagen content. The temperature T is set to 310 K, which is equal to the normal body temperature at 37 °C. The maximum exposure time of US has been set to $t_{\max} = 300\,\text{s}$ to reflect the treatment times in animal trials, which have been up to five minutes [32, 35]. The particles are considered monodisperse with a diameter corresponding to a relatively large

NP, in this case Dextran 2,000,000 with a radius of 27.2 nm [47], which is rounded to a diameter of 50 nm for convenience. The interstitial fluid has a similar viscosity to that of blood plasma, 1.2×10^{-3} Pa s [14], in addition to the same density of water, 1000 kg m^{-3}. To get a reasonable magnitude of the US-induced pressure gradient $\Delta P_u / L_y$, a value was chosen for $f = 3$ MHz [46].

Table 3.1: Table of the base case parameters used in the simulations, where each column respectively lists, for a given parameter, its name, symbol, value, unit and the source from which the value has been retrieved.

Parameter	Symbol	Value	Unit	References
Number of particles	n_p	10000	-	-
Network columns	n_x	22	-	-
Network rows	n_y	40	-	-
Cell diameter	d_c	10	µm	[46]
Link length	L_0	5	µm	[46]
Link diameter	d_l	200	nm	[19]
Particle diameter	d_p	50	nm	[47]
Body temperature	T	310	K	-
Interstitial fluid viscosity	μ_0	1.2×10^{-3}	Pa s	[14]
Interstitial fluid density	ρ_0	1000	kg m^{-3}	-
US-induced pressure gradient	$\Delta P_u / L_y$	2.5×10^5	Pa m^{-1}	[46]
Maximum exposure time	$t_{\max}$	300	s	[32, 35]

The transport from the base case simulations using the exact parameters in table 3.1 yields $\mu_x = 43.3$ µm and $\sigma_x = 43.3$ µm. To give the reader an idea of how the particles spread through a network larger in scale than the one in fig. 3.2, a schematic and results of an example simulation run can be in fig. 3.3. The figure shows the particle distribution for the parameters $t_{\max} = 150$ s and $n_x = 16, n_y = 20$ for $n_p = 200$ particles. This example simulation yields $\mu_x = 21.5$ µm and $\sigma_x = 30.1$ µm.

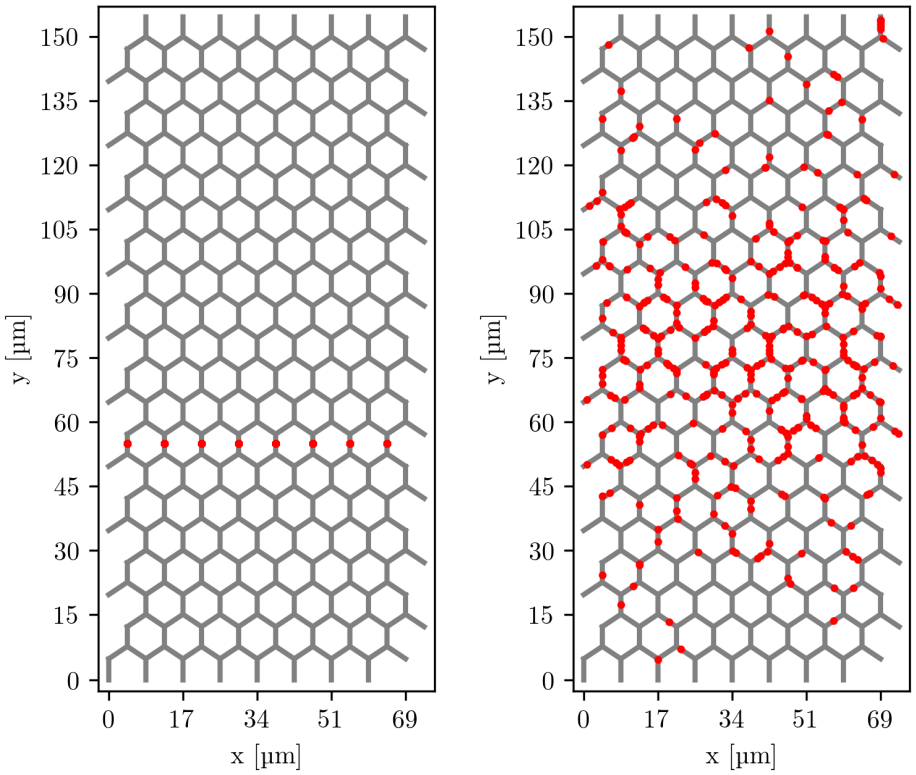

(a) At $t = 0\,\mathrm{s}$.

(b) After $t = 300\,\mathrm{s}$.

Figure 3.3: Schematic of the base case pore network with $n_x = 16, n_y = 20$ for $n_p = 200$ particles. The particles have starting positions vertically in the center of the network at $t = 0$ (fig. 3.3a). After the base case simulation has been run, the mean and standard deviation is calculated from the final particle positions at $t = 150\,\mathrm{s}$, which yields $\mu_x = 21.4\,\mu\mathrm{m}, \sigma_x = 30.1\,\mu\mathrm{m}$ (fig. 3.3b). Each point signifies an individual particle. Note that while x and y are the network coordinates, the subscript x of μ_x and σ_x signify the one-dimensional nature of the particle transport into the network, i.e. the y direction.

4 Simulation validations

Since numerical simulations are used to obtain results for given problems, the validity of the model has to be assessed to ensure its quality. The goal of any numerical simulation is to emulate the behavior of the real world as closely as possible through the use of numbers. A numerical simulation can never match the behavior of the real world, and one can only be sure that the results are good approximations [48].

To perform a validation is to compare the current model to a pattern or reference model. Validations can be done by comparison to analytical solutions, if known. One can then be sure that the code yields a solution approximately close to the exact value. Another technique is to validate by the use of other numerical simulations. If some simulation has been validated and shown to be numerically sound, it can be used as a reference to validate another simulation [48].

4.1 Advection-diffusion

A validation can be performed to ensure that the sum of individual particle movements in the numerical simulations resemble the analytical particle concentration distribution at the pore-scale level. Transport of the particles in the pore network is modeled as a random walk, where each particle moves by contributions for both advection and diffusion for each timestep, where the former and latter are respectively taken as mean and variance in eqs. (3.10) to (3.11). The sizes of these contributions are modeled after the solution for the advection-diffusion equation in eq. (2.24).

The analytical and numerical approaches can both be solved for given cases and compared to ensure the validity of the simulations at the pore-scale level. The behavior for a single link is thus analyzed. All particles had starting positions $x_0 = 0.5L_0$, in a rigid network with link length $L = 3L_0$, which can be thought of as a Dirac delta function $C(x, 0) = C_0'\delta(x_0)$. By using the base case parameters in table 3.1, setting $x_{\max} = 0.1L_0$, $C_0' = 1$ and choosing a time step with $\tau = 100$

as in eq. (3.14), the particles were transported each timestep with accordance to eq. (3.13) and a probability density function was plotted against particle position x at a given time.

Table 4.1: Table of comparisons for analytical particle position μ_x and its variance σ_x for the times $t = \{1.651, 18.166, 51.197\}$ ms, where $\delta\mu$ and $\delta\sigma$ are the the relative errors in percent for the numerically equivalent quantities. For all time steps, the relations $|\delta\mu| < 1\,\%$ and $|\delta\sigma| < 1\,\%$ are shown, which seems to indicate that the numerical simulations are valid when compared to the analytical expression.

t[ms]	μ_x[µm]	$\delta\mu$	σ_x[µm]	$\delta\sigma$
1.651	2.500	0.158 %	0.158	0.304 %
18.166	2.505	0.252 %	0.524	0.735 %
51.197	2.513	0.195 %	0.880	−0.369 %

Examples of this are shown graphically in fig. 4.1 for the times $t = \{1.651, 18.166, 51.197\}$ ms. The particle probability density function, given in μm^{-1} are plotted as functions of particle positions in µm as histograms in which the integral is 1. Then μ and σ are estimated by fitting a normal distribution $x \sim N(\mu, \sigma^2)$ to the histogram, which is plotted and compared against eq. (2.24). These quantities are then compared to the analytically equivalent quantities μ_x and σ_x by calculating the relative errors in percentage, as summarized in table 4.1. For larger times, both means and standard deviations increase as expected. The relative errors are less than 1 % for all cases, which leads to the conclusion that the transport of particles in the presented solutions are numerically sound when compared to the analytical solutions.

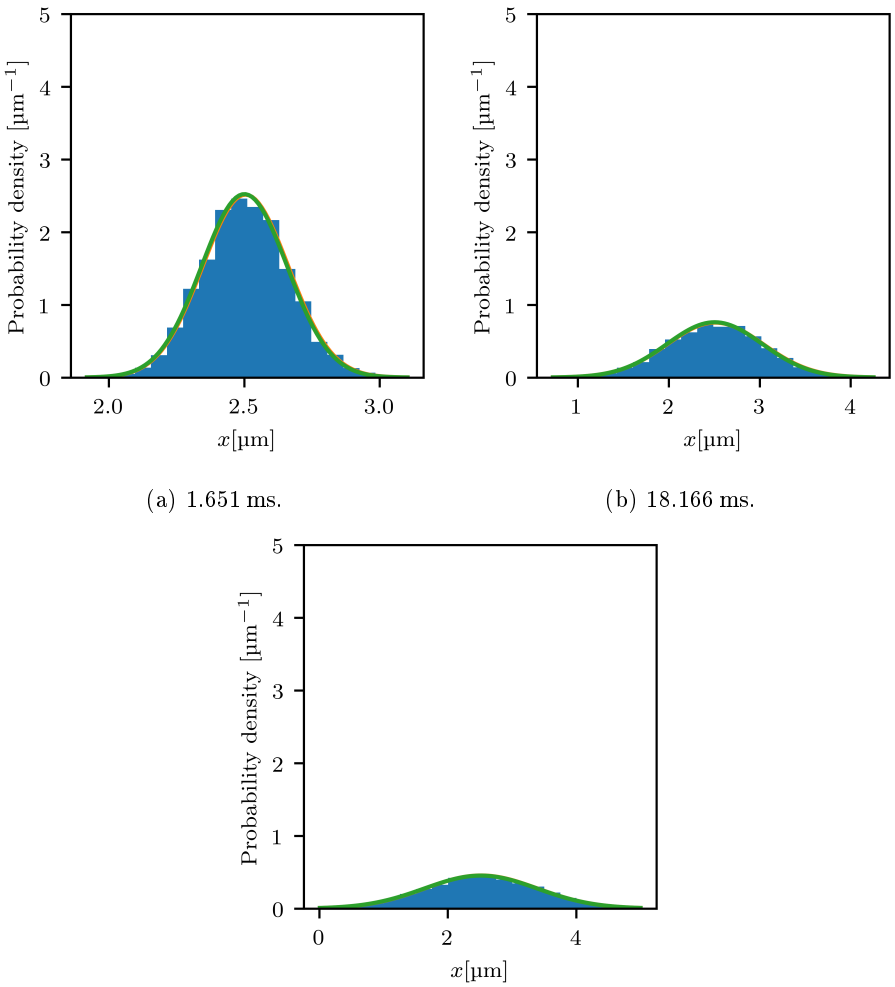

(a) 1.651 ms.

(b) 18.166 ms.

(c) 51.197 ms.

Figure 4.1: Comparisons of numerical and analytical solutions for particle positions after timesteps $t = \{1.651, 18.166, 51.197\}$ ms. The particle probability density function in µm are plotted against particle positions in µm. The base case parameters in table 3.1 for a rigid network with link length of $L = 3L_0$ are used, and start position is set to $x_0 = 0.5L_0$ and $C_0' = 1$. Iteration steps are set with $\Delta x_{\max} = 0.1L_0$ and the time step chosen as in eq. (3.14) with $\tau = 100$. As time goes on, both the mean μ_x and standard deviation σ_x of the particles increase as predicted.

4.2 Advective link selection

For each timestep the particles propagate a certain distance trough the link they are currently residing in, and has to go trough a new link when a node is reached. To ensure that the selection process works as intended for the advection step, in which the next link is drawn from a weighted probability distribution, the properties can be analyzed for given numbers of particles in the network. By only transporting the particles by advection, the choosing of the next link from a selection of links can be compared to a Bernoulli process. This process consists of a series of repeated trials where each trial can result in two possible outcomes, and must possess the following properties [49].

1. The number of repeated trials is n.

2. Each trial must result in one of two outcomes.

3. The probabilities for the outcomes are p and $q = 1 - p$, and remains constant for all trials.

4. All repeated trials are independent.

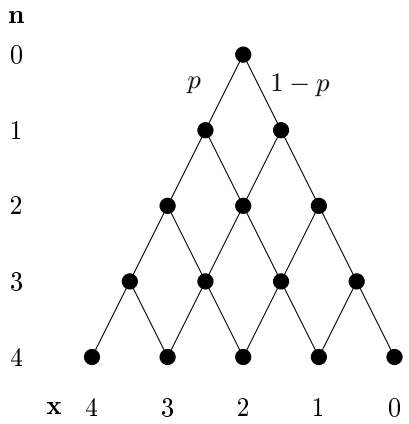

Figure 4.2: Diagram of probability outcomes in the binomial distribution where n, the number of trials, can be interpreted as the nth row and x, the number of exact outcomes with probability p, as the kth column. After a given outcome, the probability of going to the left is p, and $1 - p$ to the right.

The probability of getting exactly x outcomes of a trial with probability p in n trials is known as the binomial distribution [49, p. 144], is given as

$$b(x; n, p) = \binom{n}{x}^{x} q^{n-x} = \binom{n}{x} p^x (1-p)^{n-x}, \tag{4.1}$$

where $x \in [0, n]$. A diagram of a given number n and x for the binomial distribution can be seen in fig. 4.2.

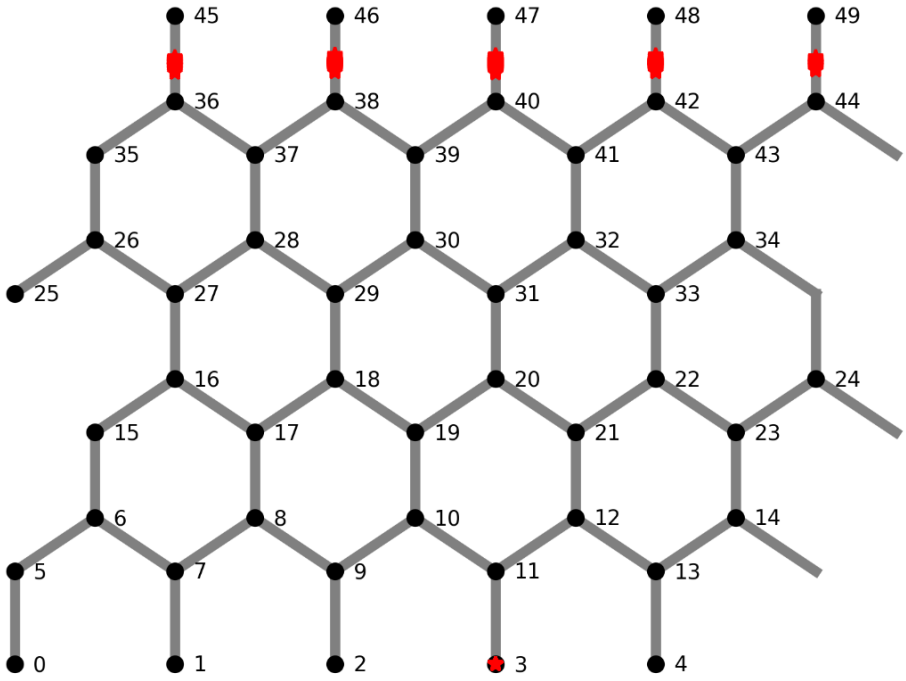

Figure 4.3: A schematic illustration of particle positions in the pore network. At the start, all particles are situated at the start of the link denoted by nodes 3 and 11. The particles have then been transported and distributed to five vertical links at the top boundary. If all non-vertical links have equal flow rates, shis case is similar to the binomial distribution for $n = 4$, since a final position in a vertical link is labeled as outcomes $x = 0$ to the far left and $x = 4$ to the far right.

If all the links in the network have equal diameters, it can be assumed that all vertical links have double the flow rate of the non-vertical links. The reasoning is that since the flow rate have to be conserved, and each row is connected by half the amount of links in the row itself. When a particle being transported through a vertical link reaches a node, the next link is being chosen from a weighted probability distribution which depends on the flow rate in the next possible links. If the flow rate of the next links are equal, due to the hereby mentioned assumed equal flow rate in the non-vertical links, the probabilities for the two possible outcomes must also be equal.

Hence, for the special case where the probabilities for the two outcomes are equivalent, i.e. $p = q = 0.5$, eq. (4.1) can be reformulated as

Table 4.2: Table of mean square errors (MSE) in eq. (4.2) for $n = 4$ and compared to particle numbers $n_p = \{200, 1000, 2000, 4000, 8000, 16000\}$. The MSE are of magnitudes 1×10^{-4} to 1×10^{-6}.

n_p	MSE
200	9.9×10^{-4}
1000	5.0×10^{-4}
2000	3.1×10^{-6}
4000	1.2×10^{-5}
8000	6.9×10^{-6}
16000	6.5×10^{-6}

$$f(x, n) \equiv b(x; n, 0.5) = \binom{n}{x} 0.5^n, \tag{4.2}$$

which can be compared to the particle distribution in a pore network with a single link diameter. Each final position in a vertical link is analogue to a discrete outcome x. An example comparison can be seen in fig. 4.3, where a given number of particles in a base-case network initially have been placed in the same link. The system has then been evolved over time until the particles are distributed over five different links, which in this case corresponds to a binomial distribution where $n = 4$ and $p = 0.5$. This case has been tested for a different amount of particles, $n_p \in \{200, 1000, 2000, 4000, 8000, 16000\}$, as expressed in eq. (4.2).

A graphical overview of these calculations can be seen in fig. 4.4 and an overview of mean square errors in table 4.2. The mean square error *MSE* seems to decrease for larger particle numbers. This means that the base case parameter for n_p in table 3.1, which is set to 10000, can be used throughout the simulations with sufficient and valid numerical behavior. However, since the diffusion constant for these validations has been set as $D \approx 0$ in order to investigate the outcome of the link selections as the particles move through the network, the particle distribution will in essence be a moving Dirac delta function. When diffusion is non-negligible, the particle distribution is a Gaussian as described in eq. (2.23), and a higher number of particles will show a better fit to the analytical solution.

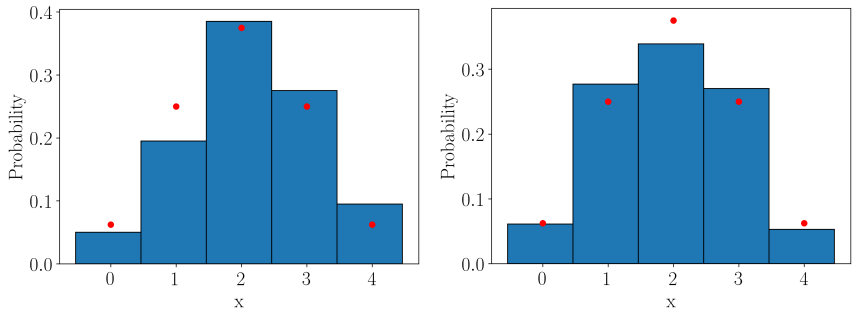

(a) $n_p = 200$.

(b) $n_p = 1000$.

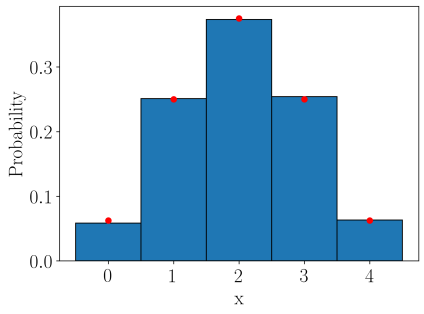

(c) $n_p = 2000$.

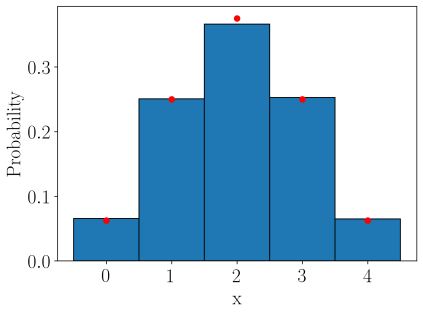

(d) $n_p = 4000$.

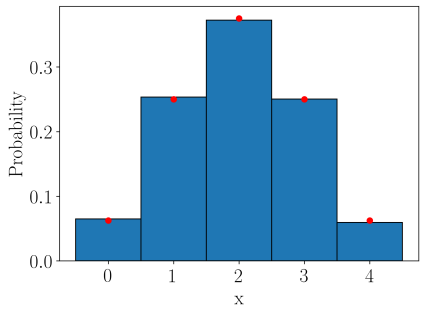

(e) $n_p = 8000$.

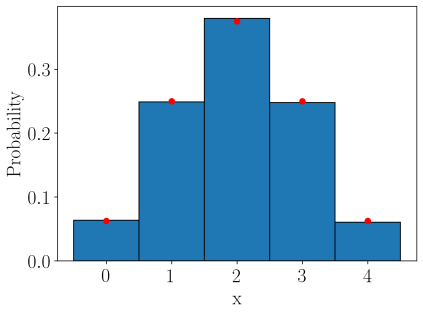

(f) $n_p = 16000$.

Figure 4.4: Numerical binomial distributions calculated for $n_p \in \{200, 1000, 2000, 4000, 8000, 16000\}$ particles compared to the analytical expression for $p = 0.5$ with $n = 4$. The numerical binomial distributions are plotted as histograms in which the value of the bins sum to 1. The red points represent the exact binomial distribution values in eq. (4.2).

5 Results

This chapter contains the results from simulating the base case as described in section 3.5, where one parameter at a time has been varied while the others parameters in table 3.1 were kept fixed. The particle starting positions at $t = 0$ were set a certain vertical distance into the network, similarly as in fig. 3.3a. Once a given time $t_{\max}$ had been reached, the initial particle positions were subtracted from the final positions.

A fit to a normal distribution was then done in order to approximate the PPD μ_x and standard deviation σ_x. These are the variables calculated at the tissue-scale. At the pore-scale, the flow rate q was calculated as the sum of the flow rates at the inlet links, i.e. from the side at which the pressure is applied as a Dirichlet boundary condition. The Reynolds and Péclet numbers were also calculated at the pore-scale, in accordance to eq. (2.31) and eq. (2.34) respectively. Linear regressions were then performed to establish scaling relations between a given input parameter and transport at the tissue-scale, in addition to estimations of particle velocity and effective diffusion coefficients. Empirical sets of equations incorporating these scaling relations and estimations will be presented.

5.1 Parameter analysis

The results for PPDs as functions of μ_0, d_l, $\Delta P_y/L_y$, $t_{\max}$ and D respectively are shown in fig. 5.1a, fig. 5.6a, fig. 5.11a, fig. 5.21b and fig. 5.16a. For each case, the base case parameters in table 3.1 have been used, where one parameter has been varied and the other kept fixed, and the PPD has been calculated. The point is the mean transport as in eq. (2.25), and the error bars represent the standard deviation σ_x of the PPDs which occurs due to particle diffusion in eq. (2.26). The Reynolds number in eq. (2.31) and Péclet number in eq. (2.34) were also calculated and plotted for each case, in addition to the flow rate q.

Additionally, to determine how the different results scale when the current parameter is varied, straight lines were fitted trough linear regression to log-log plots of

the data. For the PPD μ_x and standard deviation σ_x the slope β, which is the exponent of the power law relationship in eq. (A.1), can then be calculated to determine the scaling relation. The sample coefficient of determination R^2, eq. (A.4), indicates the total variation of the values in the log-log plot that can be accounted for by the linear fit. The closer R^2 is to 1, the better the fit. See appendix A for an explanation of the comparisons between log-log plots and power laws.

5.1.1 Variation of viscosity

In the first case all parameters were fixed except μ_0, which varied from 0.72 kPa s to 1.68 kPa s in the simulations. The PPD, and the standard deviation as well, reached a maximum of $\mu_x = 71.4\,\mu\text{m}$ and $\sigma_x = 54.0\,\mu\text{m}$ at $\mu_0 = 0.72\,\text{kPa s}$ and a minimum of $\mu_x = 30.42\,\mu\text{m}$ and $\sigma_x = 35.0\,\mu\text{m}$ at $\mu_0 = 1.68\,\text{kPa s}$, as seen in figs. 5.1a and 5.2a.

From the expression for Hagen–Poiseuille flow, eq. (2.11), flow rate is inversely related to viscosity as

$$q \sim \frac{1}{\mu_0}, \tag{5.1}$$

This is validated in figs. 5.3a to 5.3b, with an exponent $\beta = -1.0$ from the linear regression in eq. (A.2) . In the PPD however, see fig. 5.1b, the slope is $\beta = -0.999$ at the tissue-scale, which corresponds well with the flow rate in eq. (5.1) at pore-scale. The standard deviations for PPD also seem to be decreasing over the inverse in fig. 5.2a, since at the pore-scale

$$D \sim \frac{1}{\mu_0}, \tag{5.2}$$

and the standard deviation is related to the diffusion coefficient as

$$\sigma_x \sim \sqrt{D}. \tag{5.3}$$

The standard deviation should thus be inversely proportional to the inverse root of the viscosity μ_0. The log-log plot of this relationship is seen in fig. 5.2b with $\beta = -0.476$ at the tissue-scale, which corresponds well with eqs. (5.2) to (5.3).

As both D and q decreases with the same inverse exponent, the Peclet number, as defined in eq. (2.34), the ratio between these two terms will be kept constant for all μ_0 as seen in fig. 5.5 with $\text{Pe} \approx 0.087$. Since this is lower than 1, the diffusive transport is the dominant factor in this case. The Reynolds number has in this case

magnitudes of Re ≈ 0.5 to 2.5 as seen in fig. 5.4a, and is related to the viscosity as

$$\mathrm{Re} \sim \frac{1}{\mu_0^2}, \tag{5.4}$$

which is verified in fig. 5.4b with $\beta = -2.0$. Due to the Reynolds number being low, the viscous forces dominate the inertial ones, which means that the assumption and requirement of laminar flow is satisfied.

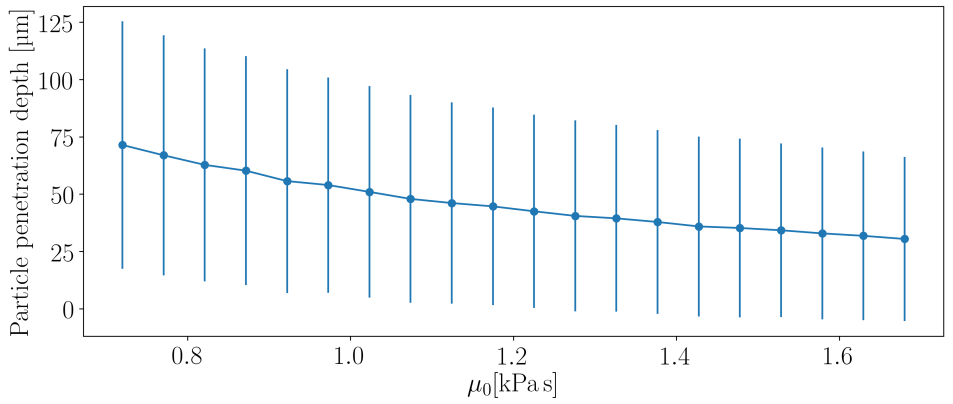

(a) PPD plotted against the variation of μ_0.

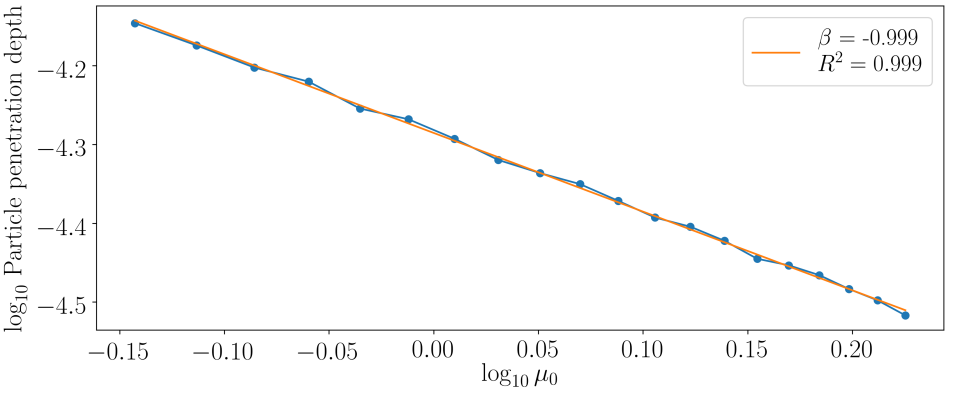

(b) Log-log plot of PPD plotted against the variation of μ_0.

Figure 5.1: PPD plots from the parameter study of μ_0, with a maximum of $\mu_x = 71.4\,\mu\mathrm{m}$ at $\mu_0 = 0.72\,\mathrm{kPa\,s}$ and minimum of $\mu_x = 30.42\,\mu\mathrm{m}$ at $\mu_0 = 1.68\,\mathrm{kPa\,s}$ (fig. 5.1a). Linear regression of the power law relationship gives an exponent of $\beta = -0.999$ with $R^2 = 0.999$ (fig. 5.1b).

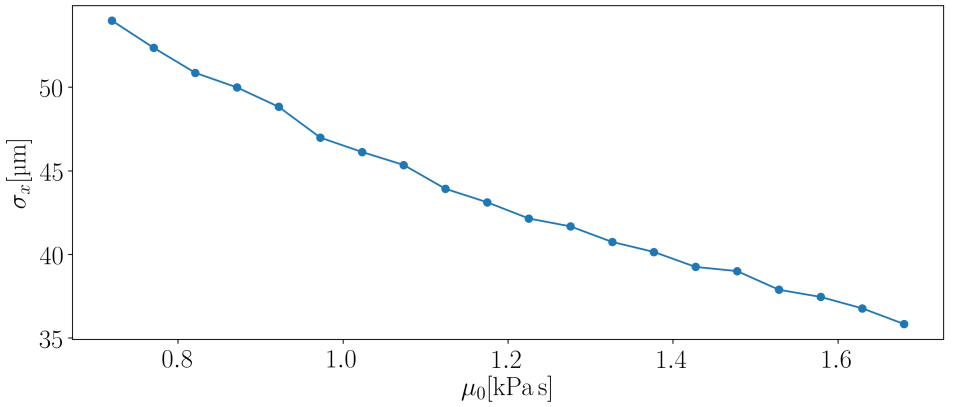

(a) Standard deviation σ_x plotted against the variation of μ_0.

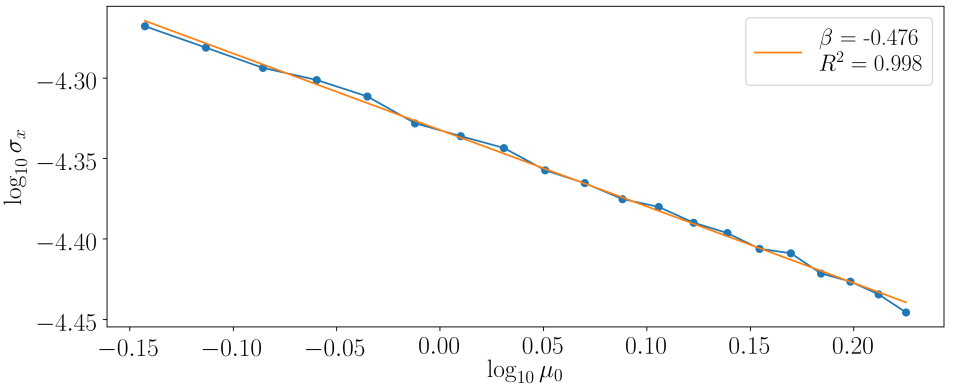

(b) Log-log plot of standard deviation σ_x plotted against the variation of μ_0.

Figure 5.2: Standard deviation σ_x plots from the parameter study of μ_0, with a maximum of $\sigma_x = 54.0\,\mu\text{m}$ at $\mu_0 = 0.72\,\text{kPa s}$ and minimum of $\sigma_x = 35.0\,\mu\text{m}$ at $\mu_0 = 1.68\,\text{kPa s}$ (fig. 5.2a). Linear regression of the power law relationship gives an exponent of $\beta = -0.476$ with $R^2 = 0.998$ (fig. 5.2b).

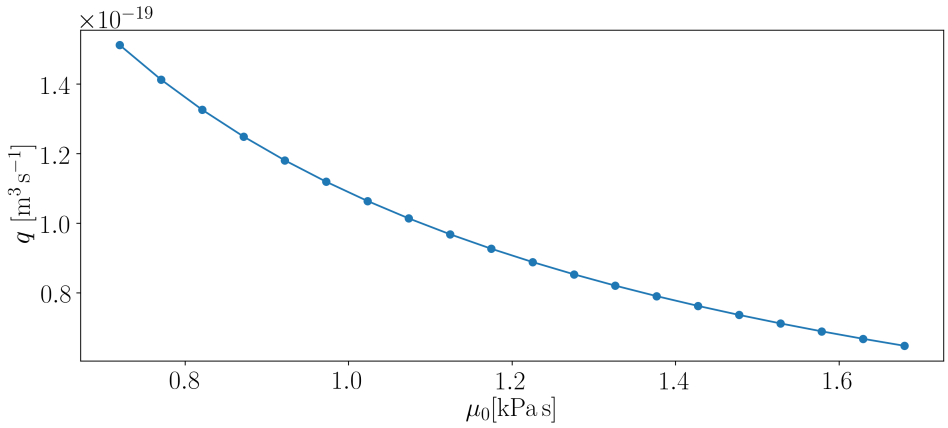

(a) Flow rate q plotted against the variation of μ_0.

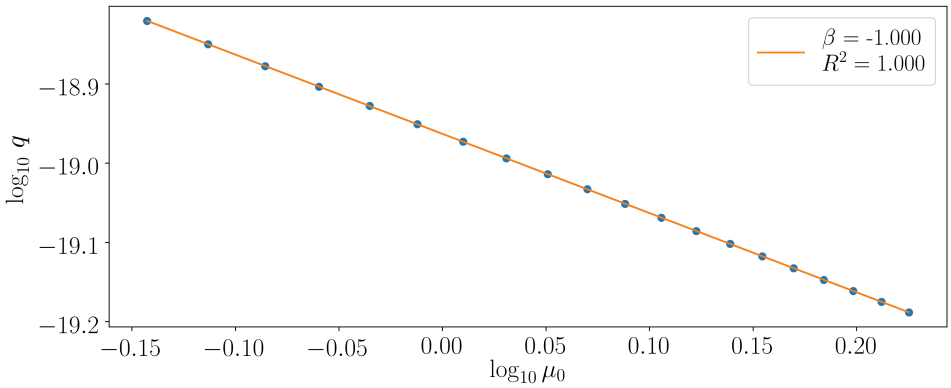

(b) Log-log plot of the flow rate q plotted against the variation of μ_0.

Figure 5.3: Flow rates q plotted against the variation of μ_0. The flow rate has magnitudes of 1×10^{-19} (fig. 5.3a). Linear regression of the power law relationship gives an exponent of $\beta = 1.000$ with $R^2 = 1$ (fig. 5.3b).

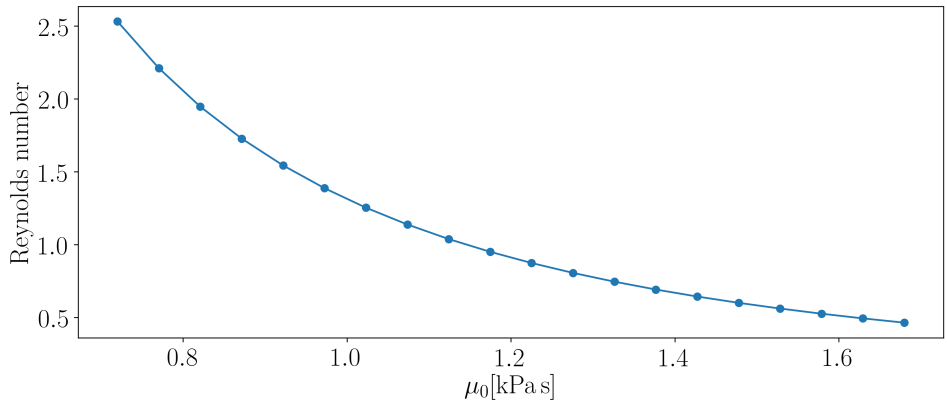

(a) The Reynolds number plotted against the variation of μ_0.

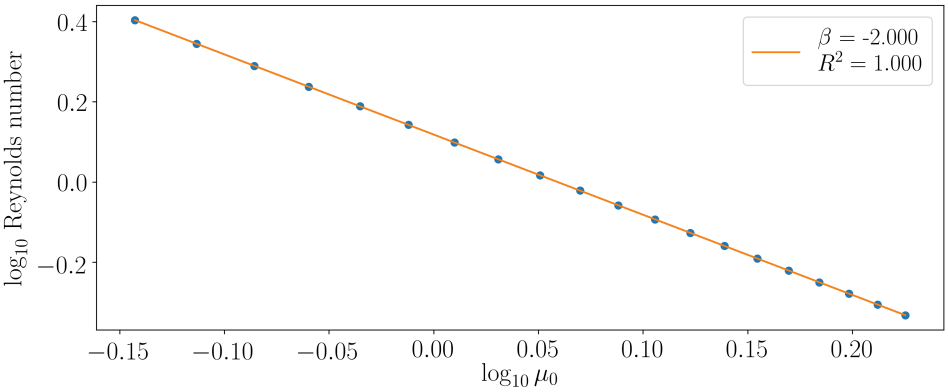

(b) Log-log plot of the Reynolds number plotted against the variation of μ_0.

Figure 5.4: The Reynolds number plotted against the variation of μ_0. The Reynolds number has magnitudes of 1 (fig. 5.4a). Linear regression of the power law relationship gives an exponent of $\beta = -2.000$ with $R^2 = 1$ (fig. 5.4b).

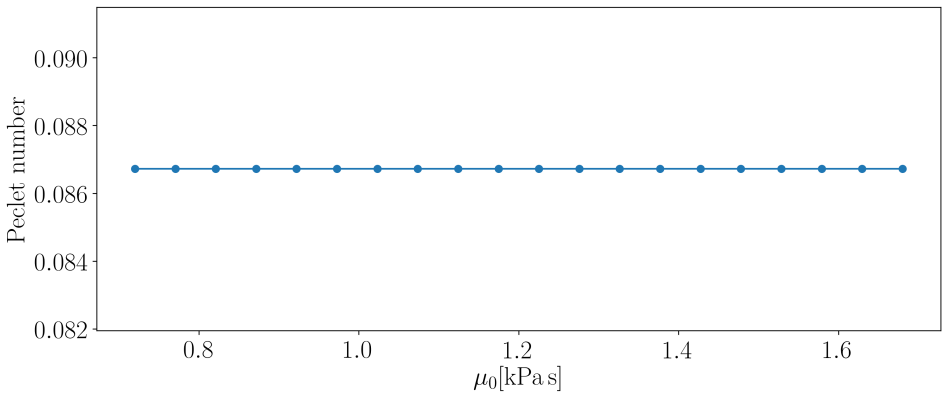

Figure 5.5: The Péclet number plotted against the variation of μ_0, with a constant value of Pe ≈ 0.087.

5.1.2 Variation of link diameter

In the second case all parameters were fixed except for the link diameter d_l, which varied from 120 nm to 280 nm in the simulations. As seen in fig. 5.6a, the penetration depth reaches a maximum of $\mu_x = 79.1$ µm at $d_l = 280$ nm and a minimum of $\mu_x = 18.1$ µm at $d_l = 120$ nm.

From the expression for Hagen–Poiseuille flow, eq. (2.11), flow rate is related to link diameter as

$$q \sim d_l^4, \tag{5.5}$$

which means that the flow velocity, eq. (3.9), will vary as

$$u = \frac{q}{a} \sim d_l^2, \tag{5.6}$$

since the cross section depends on the link diameter as $a \sim d_l^2$. The penetration depth over a given time will thus increase by this relation. The flow rate eq. (5.5) seems to be validated in figs. 5.8a to 5.8b, which is increasing and follows the linear relation in eq. (A.2) with $\beta = 4.0$. In the PPD, the slope is $\beta = 1.717$, as seen in figs. 5.6a to 5.6b, which is slightly lower at the tissue-scale than the pore-scale in eq. (5.6).

The standard deviations for PPD should to be constant, since D is independent of d_l. The standard deviation and its log-log curve is shown in figs. 5.7a to 5.7b, where the variation of the data points seem to originate from random fluctuations

in the data. The slope in the log-log plot is $\beta = -0.004$ with $R^2 = 0.023$, which means that there is no increasing noise in this trend. This means that none of the variation of the values in the log-log plot is accounted for by the linear fit.

Since q increases and D is kept constant, the Péclet number, as defined in eq. (2.34), the ratio between these two terms will be proportional to

$$\mathrm{Pe} \sim d_l^2 \tag{5.7}$$

for d_l as seen in figs. 5.10a to 5.10b where Pe has values with magnitude 1×10^{-2} to 1×10^{-1} and increases with $\beta = 2.0$. The advective transport will therefore become more dominant for increasing d_l in this case. The Reynolds number is related to the link diameter as

$$\mathrm{Re} \sim d_l^2, \tag{5.8}$$

which in this case has magnitudes of 1×10^{-1} to 1 and a slope $\beta = 2.0$, as seen in figs. 5.9a to 5.9b. Due to the Reynolds number being low, the viscous forces dominate the inertial ones, which means that the assumption and requirement of laminar flow is satisfied.

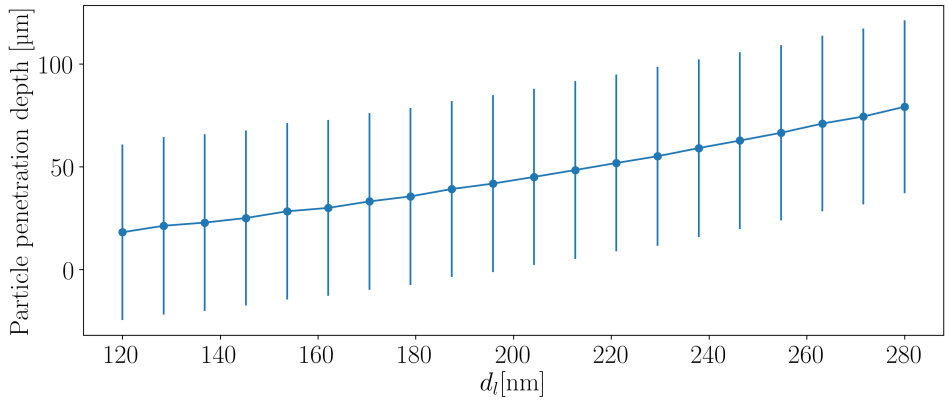

(a) PPD plotted against the variation of d_l.

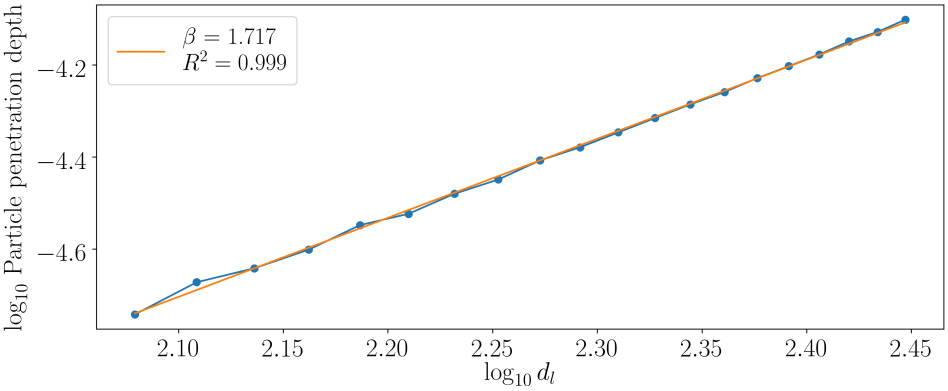

(b) Log-log plot of PPD plotted against the variation of d_l.

Figure 5.6: PPD plots from the parameter study of d_l, with a maximum of $\mu_x = 79.1\,\mu m$ at $d_l = 280\,nm$ and minimum of $\mu_x = 18.1\,\mu m$ at $d_l = 120\,nm$ (fig. 5.6a). Linear regression of the power law relationship gives an exponent of $\beta = 1.717$ with $R^2 = 0.999$ (fig. 5.6b).

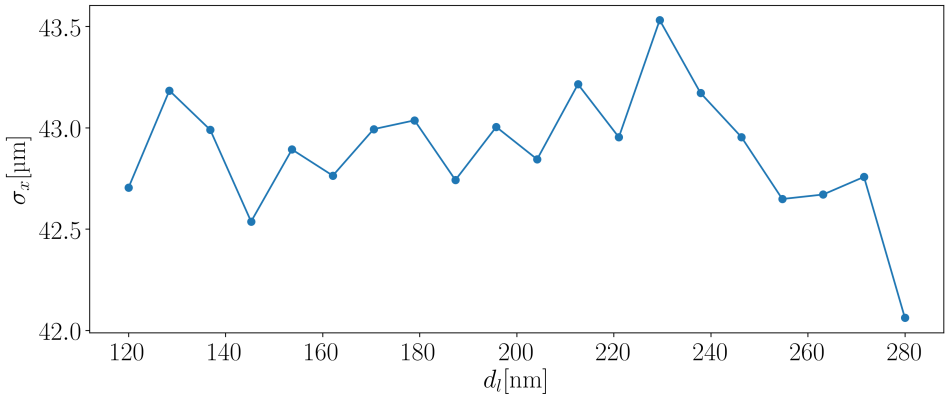

(a) Standard deviation σ_x plotted against the variation of d_l.

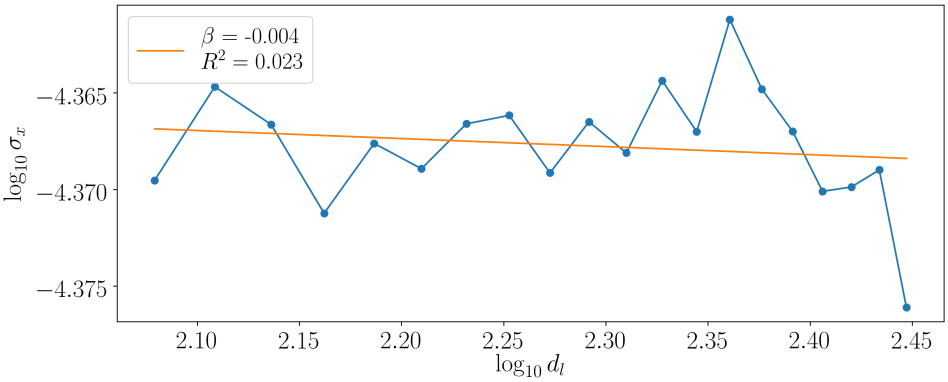

(b) Log-log plot of standard deviation σ_x plotted against the variation of d_l.

Figure 5.7: Standard deviation σ_x plots from the parameter study of d_l. The data seems to fluctuate randomly (fig. 5.7a). Linear regression of the power law relationship gives an exponent of $\beta = -0.004$ with $R^2 = 0.023$, which means that there is no trend for the noise and almost none of the variation is accounted for by the linear fit (fig. 5.7b).

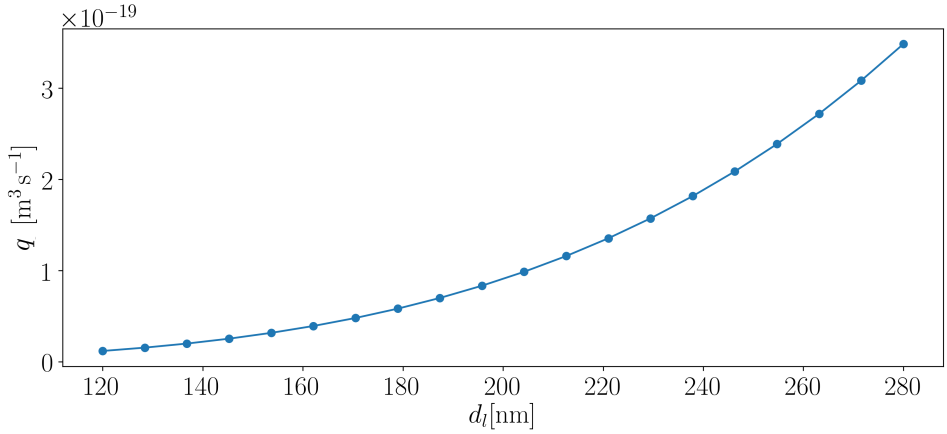

(a) The flow rate q plotted against the variation of d_l.

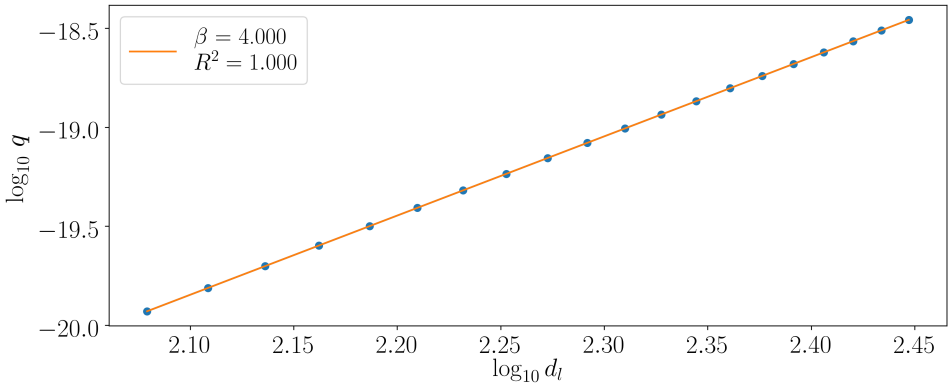

(b) Log-log plot of the flow rate q plotted against the variation of d_l.

Figure 5.8: Flow rates q plotted against the variation of d_l. The flow rate has magnitudes of 1×10^{-19} (fig. 5.8a). Linear regression of the power law relationship gives an exponent of $\beta = 4.000$ with $R^2 = 1$ (fig. 5.8b).

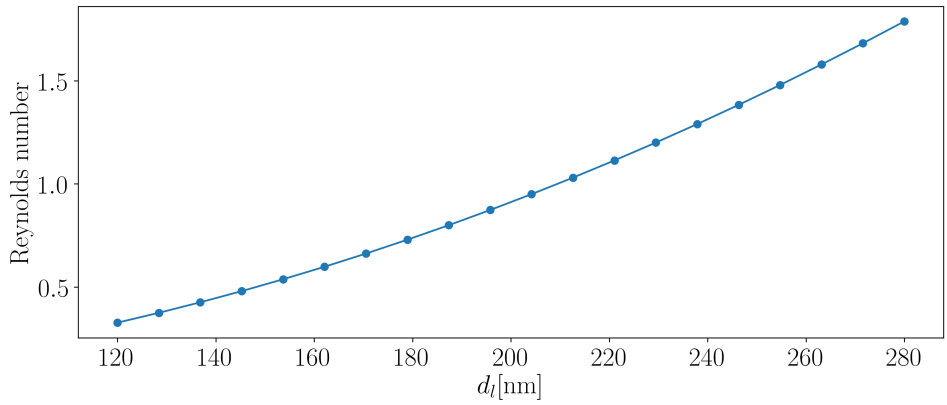

(a) The Reynolds number plotted against the variation of d_l.

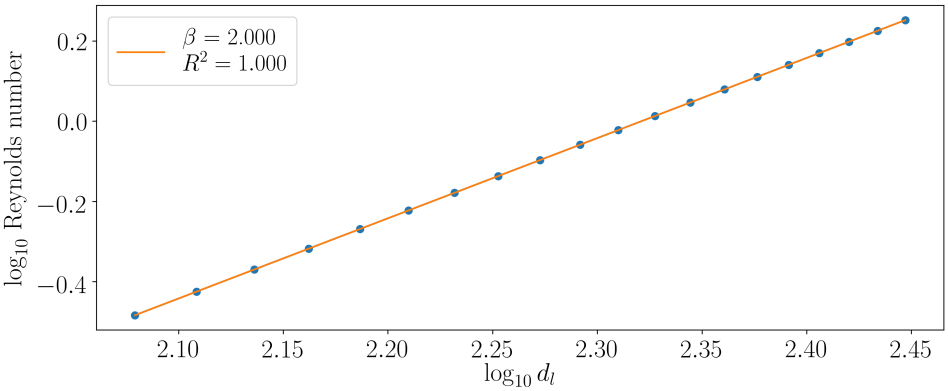

(b) Log-log plot of the Reynolds number plotted against the variation of d_l.

Figure 5.9: The Reynolds number plotted against the variation of d_l. The Reynolds number has magnitudes of 1 (fig. 5.9a). Linear regression of the power law relationship gives an exponent of $\beta = 2.000$ with $R^2 = 1$ (fig. 5.9b).

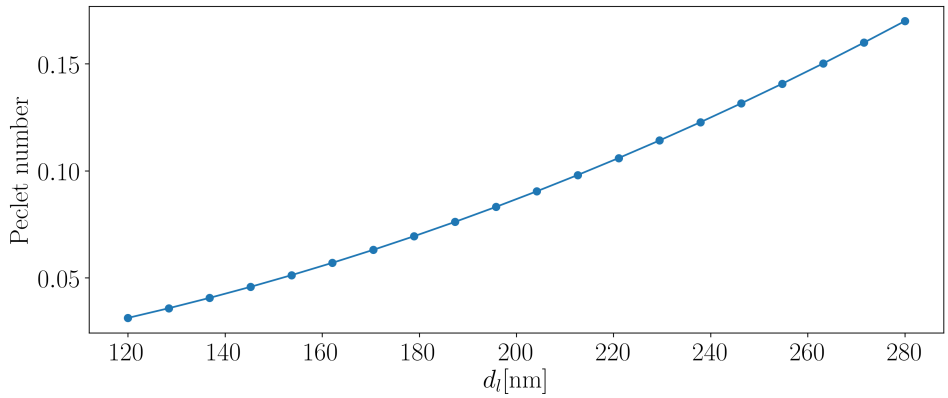

(a) The Péclet number plotted against the variation of d_l.

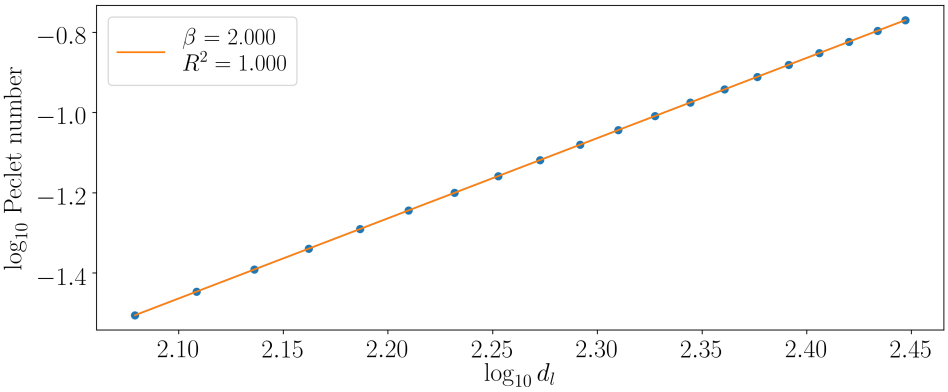

(b) Log-log plot of the Péclet number plotted against the variation of d_l.

Figure 5.10: The Péclet number plotted against the variation of μ_0. The Péclet number has magnitudes of 1×10^{-2} to 1×10^{-1} (fig. 5.10a). Linear regression of the power law relationship gives an exponent of $\beta = 2.000$ with $R^2 = 1$ (fig. 5.10b).

5.1.3 Variation of pressure gradient

In the third case all parameters were fixed for the simulations except the ultrasound-induced pressure gradient $\Delta P_y/L_y$, which was varied from $125\,\mathrm{kPa\,m^{-1}}$ to $375\,\mathrm{kPa\,m^{-1}}$. The penetration depth reached a maximum of $\mu_x = 62.4\,\mu\mathrm{m}$ at $\Delta P_u/L_y = 375\,\mathrm{kPa\,m^{-1}}$ and a minimum of $\mu_x = 24.5\,\mu\mathrm{m}$ at $\Delta P_u/L_y = 125\,\mathrm{kPa\,m^{-1}}$, which is seen in fig. 5.11a,

From the expression for Hagen–Poiseuille flow, eq. (2.11), flow rate is related linearly to the pressure gradient as

$$q \sim \Delta P_y / L_y, \tag{5.9}$$

which means that the flow rate, and therefore penetration depth over a given time, will increase by this relation. This is validated in figs. 5.13a to 5.13b, which is increasing and follows the linear relation in eq. (A.2) with $\beta = 1.0$. In the PPD expressed as a power law, however, the slope at the tissue-scale is slightly lower in comparison to the pore-scale, with $\beta = 0.865$, as seen in figs. 5.11a to 5.11b.

The standard deviations for the PPDs seem to occur from noise, since D is independent of $\Delta P_y / L_y$. The standard deviation and its log-log curve is shown in figs. 5.12a to 5.12b. Even though $\beta = -0.002$ is negative, this slope is really low with the line having an inadequate fit with $R^2 = 0.012$, which means that almost none of the variation in the log-log plot is accounted for by the linear fit. The variation of the data points thus seems to originate from random fluctuations in the data.

Since q increases and D is kept constant, the Péclet number, as defined in eq. (2.34), the ratio between these two terms will be proportional to

$$\mathrm{Pe} \sim \Delta P_y / L_y, \tag{5.10}$$

for $\Delta P_y / L_y$ as seen in figs. 5.15a to 5.15b where Pe has values with order of magnitude 1×10^{-2} to 1×10^{-1} and slope in the power law of $\beta = 1.0$. The advective transport will therefore be dominant for increasing $\Delta P_y / L_y$ in this case. The Reynolds number is related to the pressure gradient as

$$\mathrm{Re} \sim \Delta P_y / L_y, \tag{5.11}$$

which is in this case has values of 1×10^{-1} to 1. Due to the Reynolds number being low, the viscous forces dominate the inertial, which means that the assumption and requirement of laminar flow is satisfied.

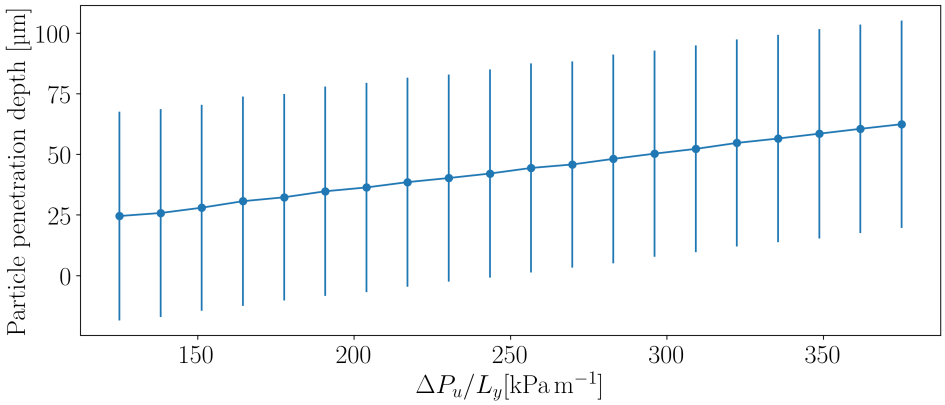

(a) PPD plotted against the variation of $\Delta P_u/L_y$.

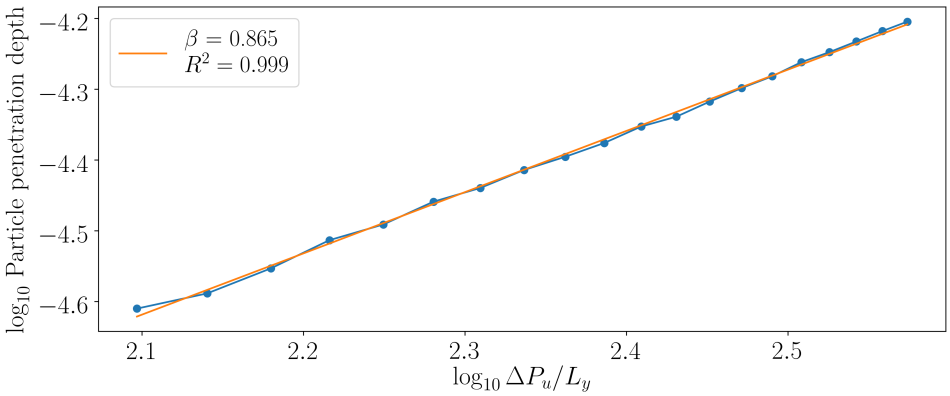

(b) Log-log plot of PPD plotted against the variation of $\Delta P_u/L_y$.

Figure 5.11: PPD plots from the parameter study of $\Delta P_u/L_y$, with a maximum of $\mu_x = 62.4\,\mu m$ at $\Delta P_u/L_y = 37\,\text{kPa m}^{-1}$ and minimum of $\mu_x = 24.5\,\mu m$ at $\Delta P_u/L_y = 125\,\text{kPa m}^{-1}$ (fig. 5.11a). Linear regression of the power law relationship gives an exponent of $\beta = 0.865$ with $R^2 = 0.999$ (fig. 5.11b).

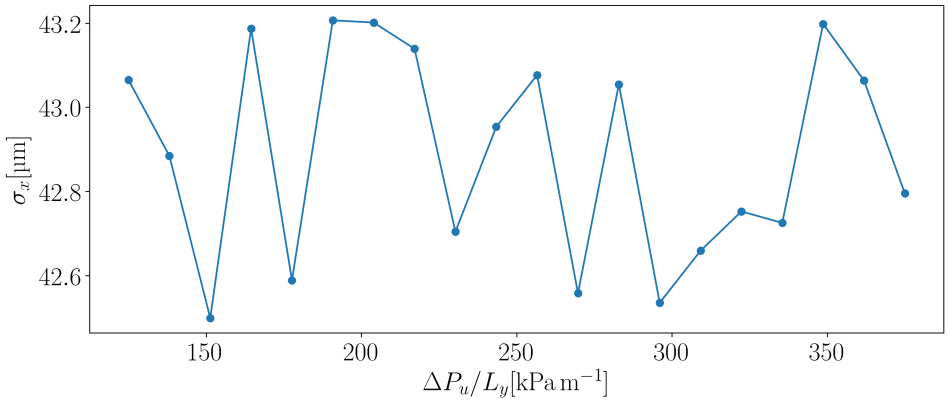

(a) Standard deviation σ_x plotted against the variation of $\Delta P_u/L_y$.

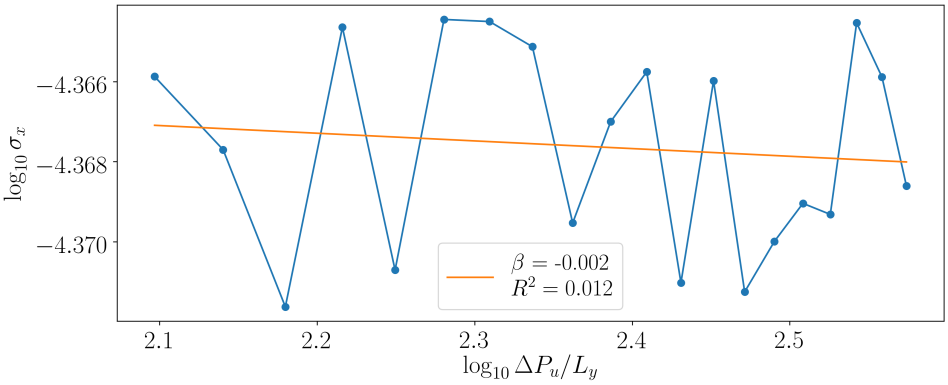

(b) Log-log plot of standard deviation σ_x plotted against the variation of $\Delta P_u/L_y$.

Figure 5.12: Standard deviation σ_x plots for $\Delta P_u/L_y$.

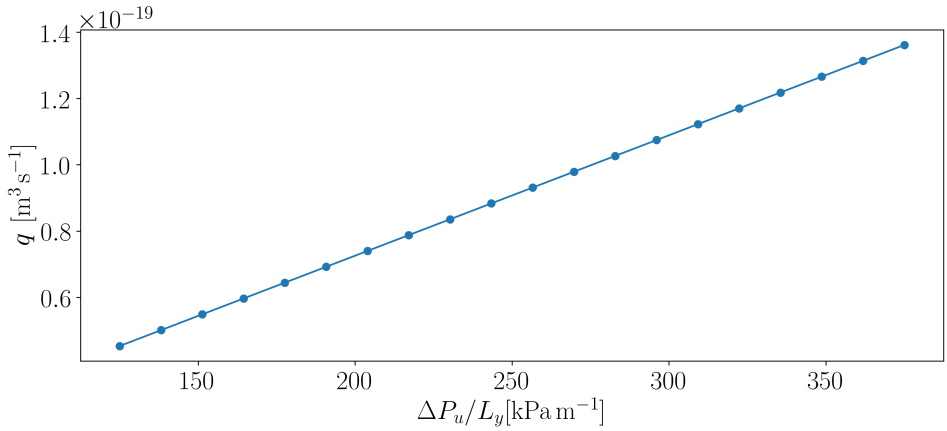

(a) The flow rate q plotted against the variation of $\Delta P_u/L_y$.

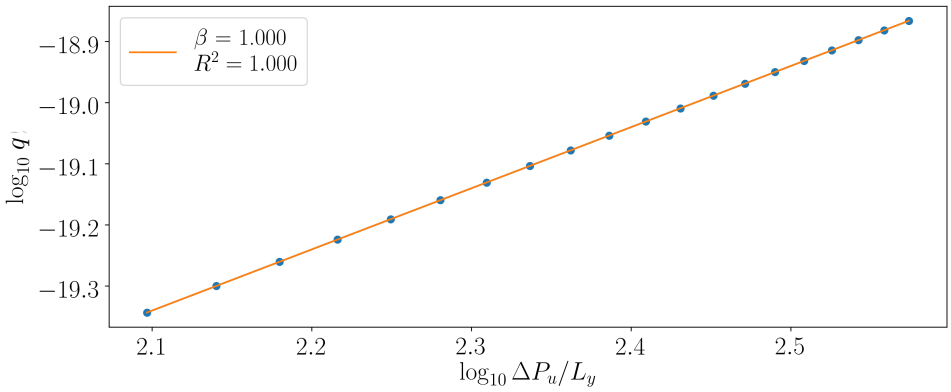

(b) Log-log plot of the flow rate q plotted against the variation of $\Delta P_u/L_y$.

Figure 5.13: Flow rates q plotted against the variation of $\Delta P_u/L_y$. The flow rate has magnitudes of 1×10^{-19} (fig. 5.13a). Linear regression of the power law relationship gives an exponent of $\beta = 1.000$ with $R^2 = 1$ (fig. 5.13b).

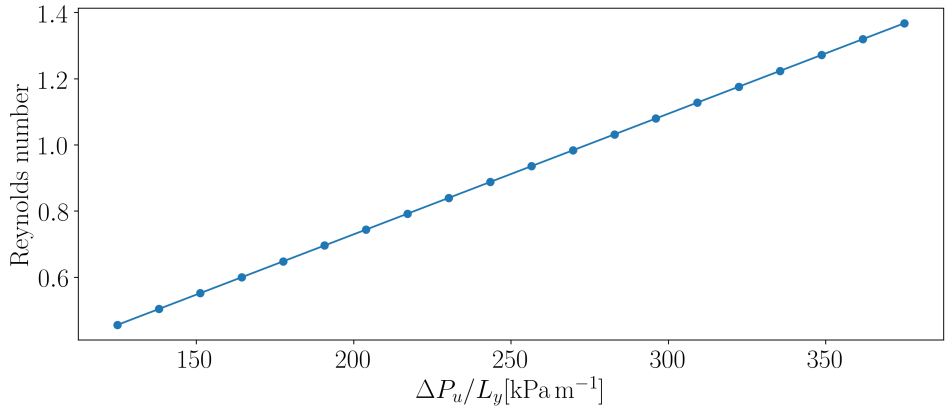

(a) The Reynolds number plotted against the variation of $\Delta P_u/L_y$.

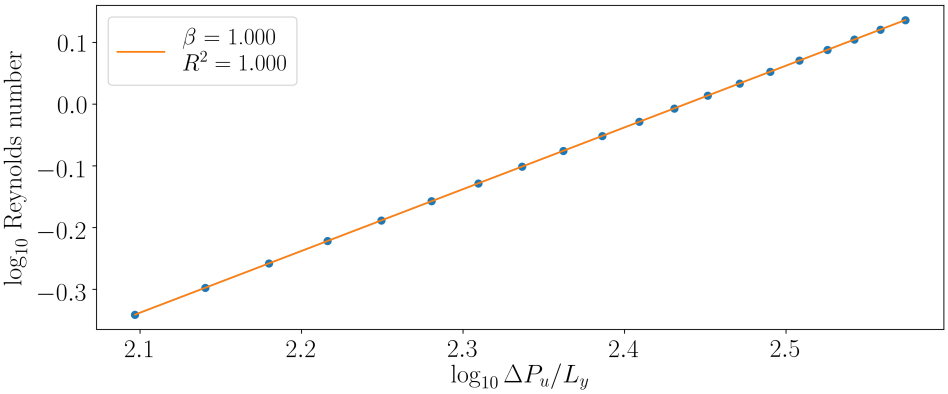

(b) Log-log plot of the Reynolds number plotted against the variation of $\Delta P_u/L_y$.

Figure 5.14: The Reynolds number plotted against the variation of $\Delta P_u/L_y$. The Reynolds number has magnitudes of 1 (fig. 5.14a). Linear regression of the power law relationship gives an exponent of $\beta = 1.000$ with $R^2 = 1$ (fig. 5.9b).

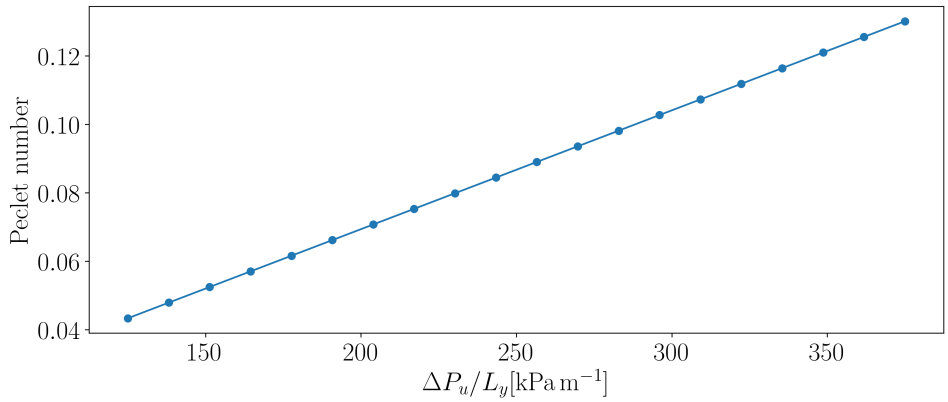

(a) The Péclet number plotted against the variation of $\Delta P_u/L_y$.

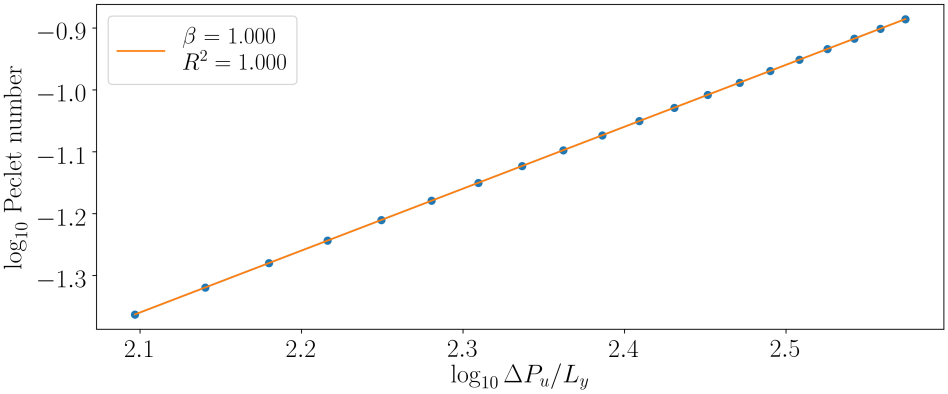

(b) Log-log plot of the Péclet number plotted against the variation of $\Delta P_u/L_y$.

Figure 5.15: The Péclet number plotted against the variation of $\Delta P_u/L_y$. The Péclet number has magnitudes of 1×10^{-2} to 1×10^{-1}(fig. 5.15a). Linear regression of the power law relationship gives an exponent of $\beta = 1.000$ with $R^2 = 1$ (fig. 5.15b).

5.1.4 Variation of the diffusion coefficient

In the fourth case all parameters except the diffusion coefficient D, which varied from $2.27\,\mu m^2\,s^{-1}$ to $9.08\,\mu m^2\,s^{-1}$, were fixed for the simulations. The flow rate is kept constant, as verified in fig. 5.18.

This trend is not seen in fig. 5.16a, where the linear regression gives an exponent of $\beta = 0.095$ with $R^2 = 1$. The slight linearity at the tissue-scale arises due to a increasing number of particles, approximately 17 out of 10000 at most, leaving the pore network at the inlet rows, due to the relatively large diffusion coefficients and time scales of the calculations. These particles are disqualified from the simulations,

causing a bias of positions in the network, since the particles are not supposed to leave the network.

The standard deviations for PPD increase due to the relation eq. (5.3) as the root, as seen in figs. 5.17a to 5.17b, where $\beta = 0.488$ with $R^2 = 0.998$, which corresponds to a standard deviation that approximately increases with the root of the diffusion coefficient.

Since q is kept constant and D increases, the Péclet number, as defined in eq. (2.34), the ratio between these two terms will be proportional to

$$\mathrm{Pe} \sim \frac{1}{D}, \tag{5.12}$$

as seen in figs. 5.20a to 5.20b where Pe has values with order of magnitude 1×10^{-1} and slope in the power law of $\beta = -1.0$. The advective transport will therefore be less dominant for increasing D in this case. The Reynolds number, as seen in fig. 5.19 with a value of $\mathrm{Re} \approx 0.91$, is independent of the diffusion coefficient, and therefore constant in this case. The Reynolds number is low, and the viscous forces dominate the inertial ones, and the assumption and requirement of laminar flow is satisfied.

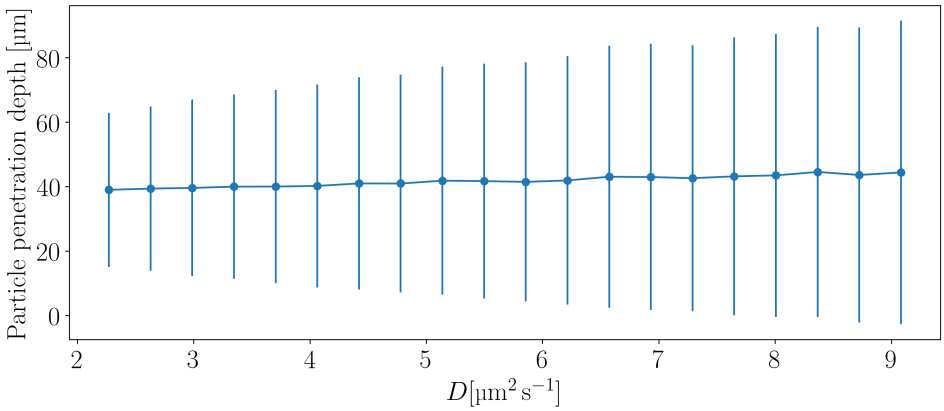

(a) PPD plotted against the variation of D.

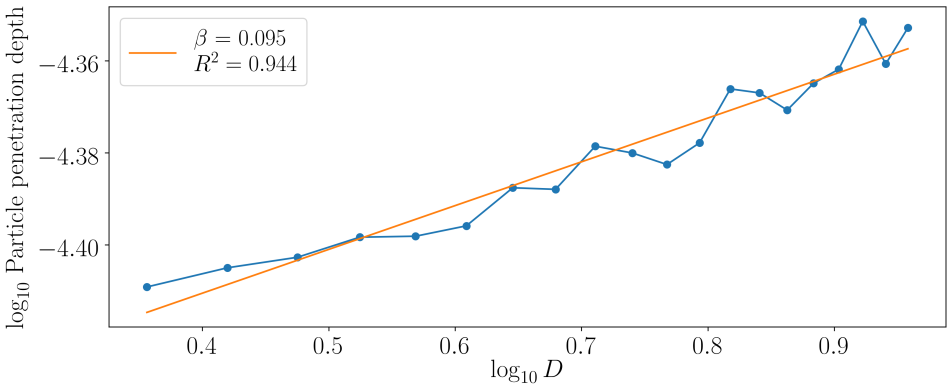

(b) Log-log plot of PPD plotted against the variation of D.

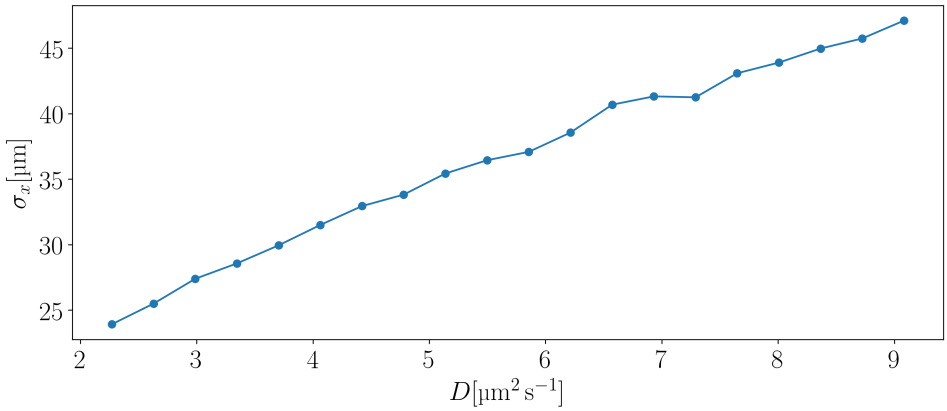

(a) Standard deviation σ_x plotted against the variation of D.

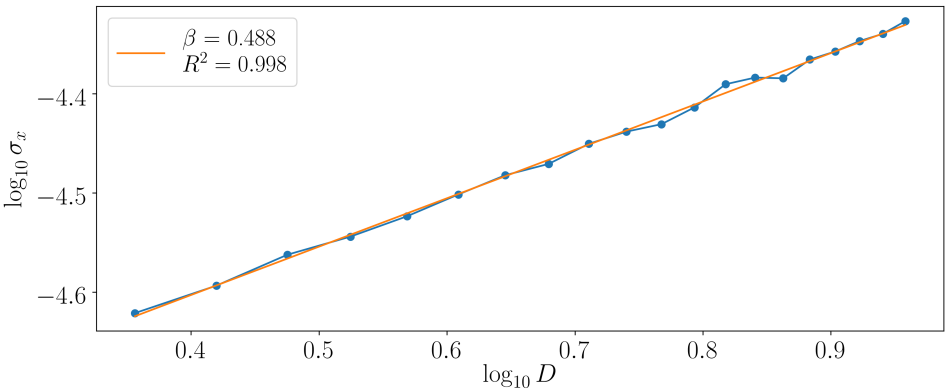

(b) Log-log plot of standard deviation σ_x plotted against the variation of D.

Figure 5.17: Standard deviation σ_x plots from the parameter study of D, with a maximum of $\sigma_x = 47.1\,\mu m$ at $D = 9.08\,\mu m^2\,s^{-1}$ and minimum of $\sigma_x = 23.9\,\mu m$ at $\mu_0 = 2.27\,\mu m^2\,s^{-1}$ (fig. 5.2a). Linear regression of the power law relationship gives an exponent of $\beta = -0.476$ with $R^2 = 0.998$ (fig. 5.2b). Linear regression of the power law relationship gives an exponent $\beta = -0.476$ with $R^2 = 0.998$ (fig. 5.17b).

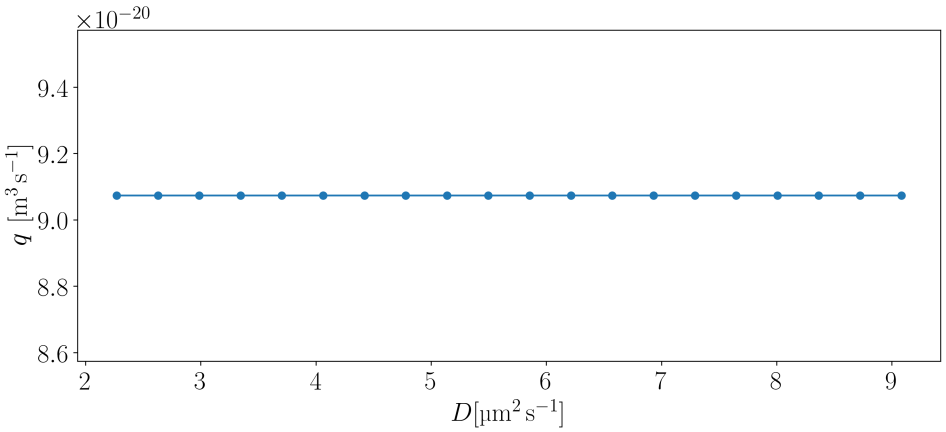

Figure 5.18: The flow rate q plotted against the variation of D, with a constant value of $q \approx 9.1 \times 10^{-20}\,\mathrm{m^3\,s^{-1}}$.

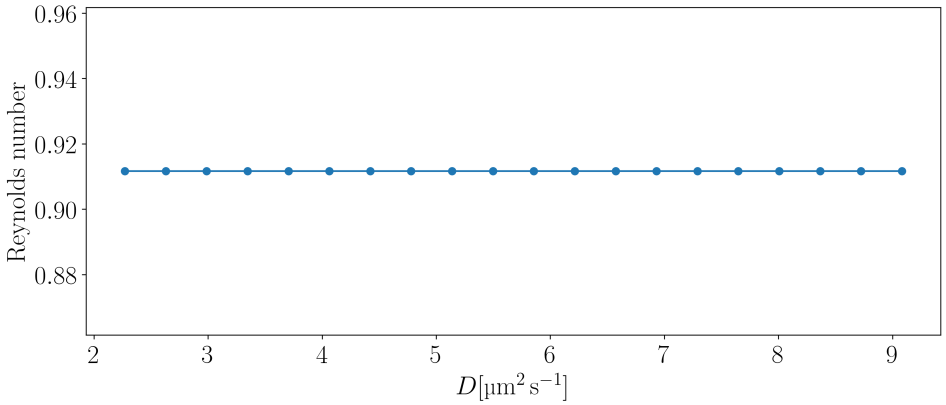

Figure 5.19: The Reynolds number plotted against the variation of D, with a constant value of $\mathrm{Re} \approx 0.91$.

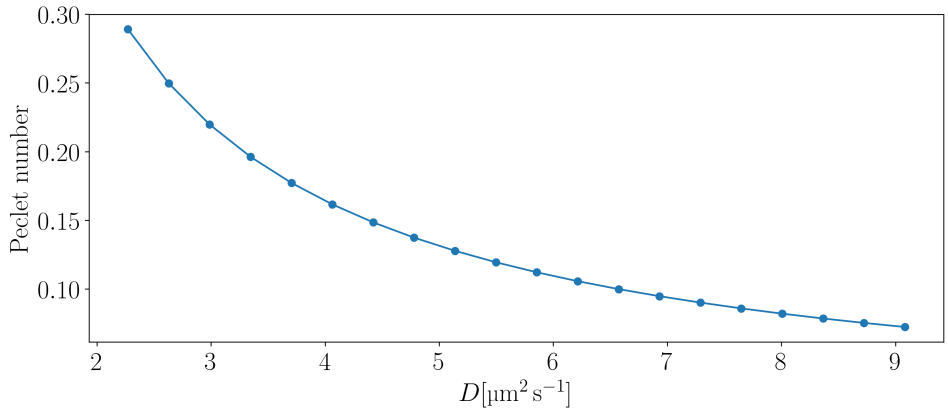

(a) The Péclet number plotted against the variation of D.

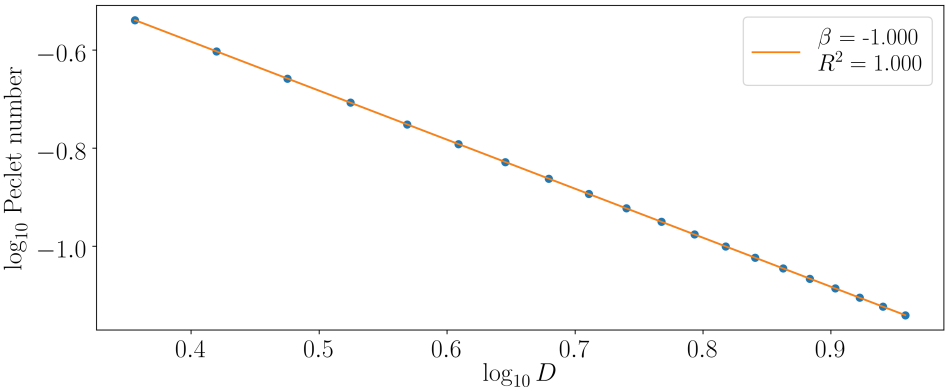

(b) Log-log plot of the Péclet number plotted against the variation of D.

Figure 5.20: The Péclet number plotted against the variation of D. The Péclet number has magnitudes of 1×10^{-1} (fig. 5.20a). Linear regression of the power law relationship gives an exponent of $\beta = 2.000$ with $R^2 = 1$ (fig. 5.20a).

5.1.5 Variation of maximum simulation time

In the final case all parameters except the maximum simulation time $t_{\max}$, which varied from 30 s to 450 s, were fixed for the simulations. The penetration depth reached a maximum of $\mu_x = 64.4\,\mu m$ at $t_{\max} = 450\,s$ and a minimum of $\mu_x = 4.10\,\mu m$ at $t_{\max} = 30\,s$ As the flow rate is kept constant for each time, longer simulation times means that the particles will penetrate further as a linear relation. This seems to be validated in fig. 5.21a and fig. 5.21b, which approximately follows the same linear relation with $\beta = 1.011$. The standard deviation for PPD is increasing with $\beta = 0.495$ as seen in figs. 5.22a to 5.22b, even though the diffusion coefficient in eq. (5.19) is independent of time, since the variance in the advection-diffusion equation, eq. (3.13), is related to the maximum time as

$$\sigma_x \sim \sqrt{t_{\max}}. \tag{5.13}$$

As both D and q themselves are independent of $t_{\max}$, the Peclet number will be kept constant for all $t_{\max}$ as seen in fig. 5.25 with $\mathrm{Pe} \approx 0.087$. The advective transport will therefore be dominant for all $t_{\max}$ in this case. The Reynolds number is also independent of $t_{\max}$ and has magnitudes of $\mathrm{Re} \approx 0.91$. The viscous forces dominate the inertial ones, which means that the assumption and requirement of laminar flow is satisfied.

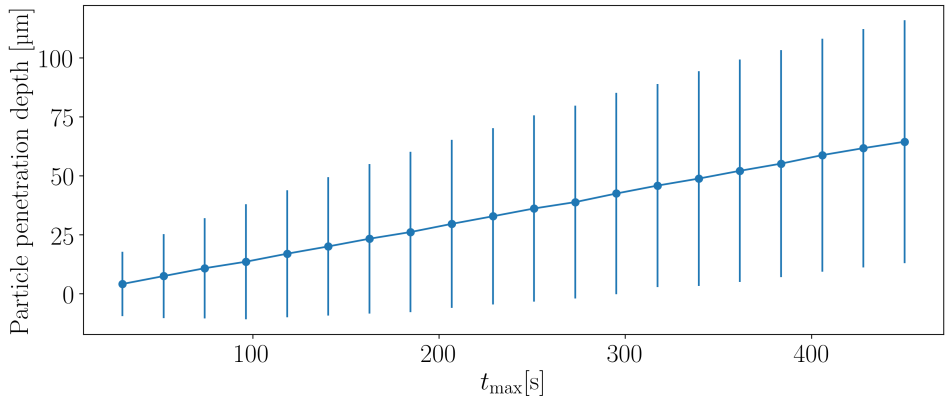

(a) PPD plotted against the variation of $t_{\max}$.

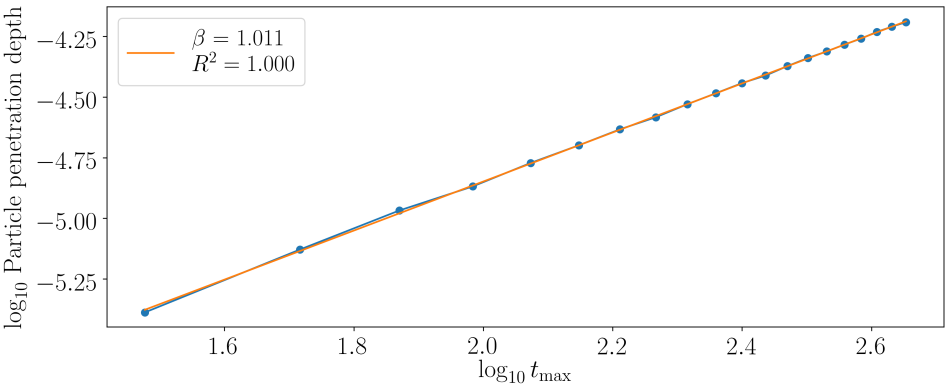

(b) Log-log plot of particle penetration plotted against the variation of $t_{\max}$.

Figure 5.21: PPD plots from the parameter study of $t_{\max}$, with a maximum of $\mu_x = 64.4\,\mu\mathrm{m}$ at $t_{\max} = 450\,\mathrm{s}$ and minimum of $\mu_x = 4.10\,\mu\mathrm{m}$ at $t_{\max} = 30\,\mathrm{s}$ (fig. 5.21a). Linear regression of the power law relationship gives an exponent $\beta = 1.011$ with $R^2 = 1.000$ (fig. 5.21b).

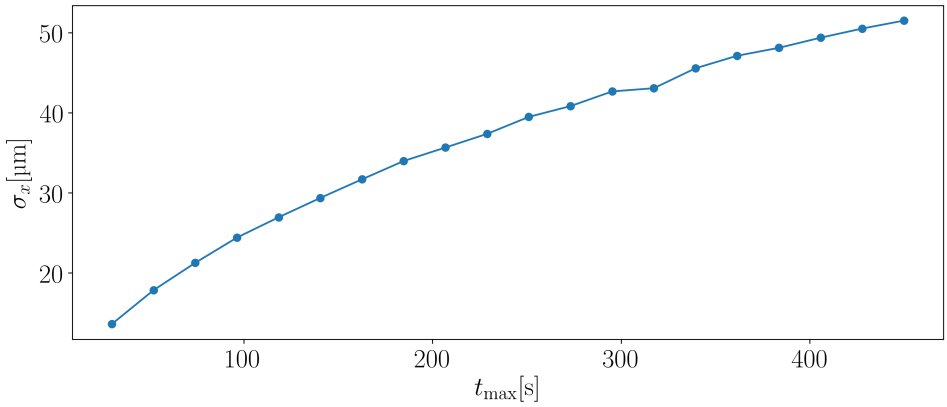

(a) Standard deviation σ_x plotted against the variation of $t_{\max}$.

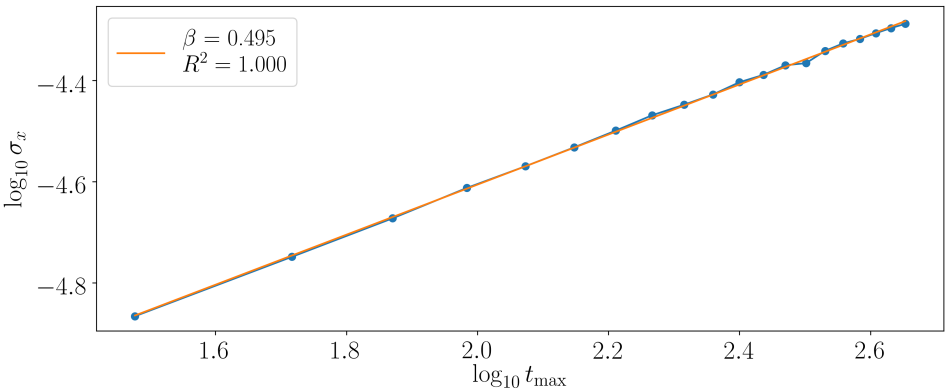

(b) Log-log plot of standard deviation σ_x plotted against the variation of $t_{\max}$.

Figure 5.22: Standard deviation σ_x plots from the parameter study of $t_{\max}$, with a maximum of $\sigma_x = 51.5\,\mu m$ at $t_{\max} = 450\,s$ and minimum of $\sigma_x = 13.6\,\mu m$ at $t_{\max} = 30\,s$ (fig. 5.22a). Linear regression of the power law relationship gives an exponent $\beta = 0.495$ with $R^2 = 1.000$ (fig. 5.22b).

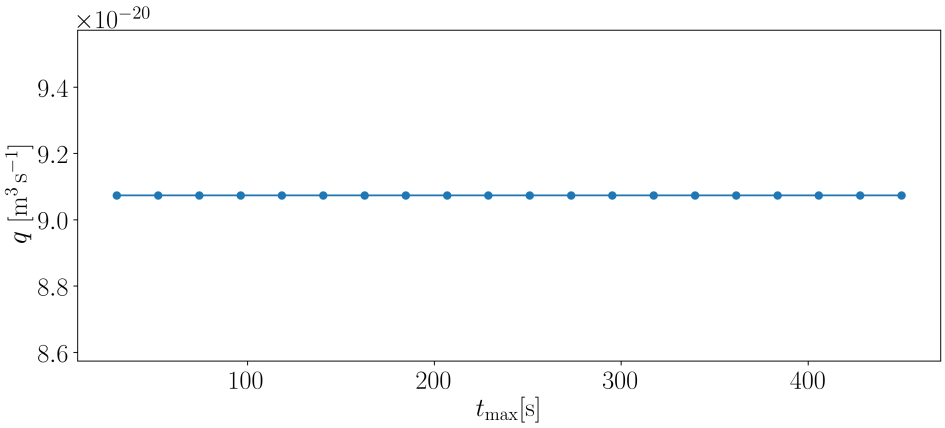

Figure 5.23: The flow rate q plotted against the variation of $t_{\max}$, with a constant value of $q = 9.1 \times 10^{-20}\ \mathrm{m^3\,s^{-1}}$.

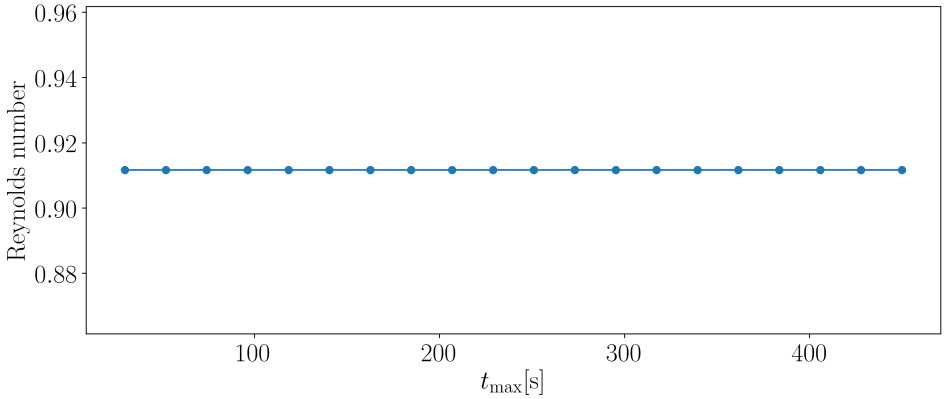

Figure 5.24: The Reynolds number plotted against the variation of $t_{\max}$, with a constant value of $\mathrm{Re} \approx 0.91$.

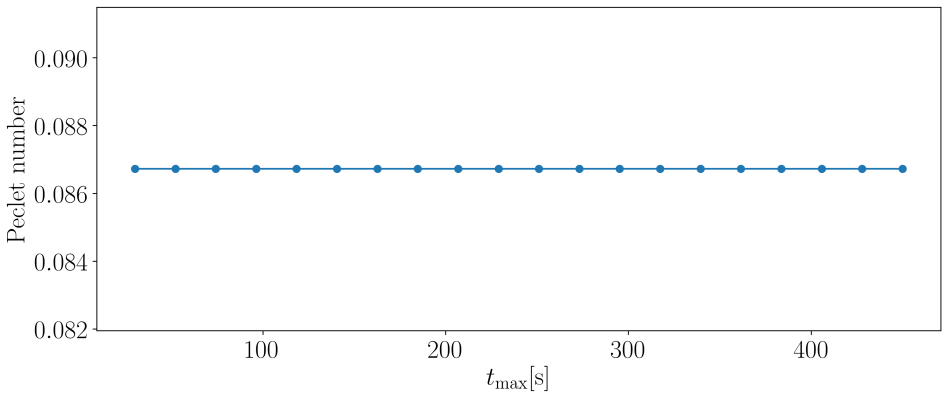

Figure 5.25: The Péclet number plotted against the variation of $t_{\max}$, with a constant value of Pe ≈ 0.087.

5.2 Interpretation of results

By variation of the parameters μ_0, d_l, $\Delta P_y/L_y$, D and $t_{\max}$ the exponents β for PPD μ_x, standard deviation σ_x, the flow rate q, and the Reynolds and Péclet numbers were established in sections 5.1.1 to 5.1.5

Table 5.1: Summary of different exponents from eq. (A.2) where the subscripts indicate the β for PPD, standard deviation σ_x, flow rate q and the Reynolds and Péclet numbers. These have individually been determined for the parameters μ_0, d_l, $\Delta P_y/L_y$, D and $t_{\max}$ by using the base case parameters in table 3.1. The cases where $\beta = 0$ have been omitted.

Parameter	β_{μ_x}	β_{σ_x}	β_q	β_{Re}	β_{Pe}
μ_0	-0.999	-0.476	-1.0	-2.0	-
d_l	1.717	-	4.0	2.0	2.0
$\Delta P_y/L_y$	0.865	-	1.0	1.0	1.0
D	-	0.488	-	-	-1.0
$t_{\max}$	1.011	0.495	-	-	-

The results seem to suggest that scaling relations between variables on the pore-scale are in accordance to the analytical solutions, i.e. flow rate q and Reynolds and Péclet numbers. Additionally, the results show that the scaling relations carried over variables at the tissue-scale, PPD and standard deviation, are similar or slightly lower than the expected values at the pore-scale.

5.2.1 Power law transport extrapolation

The exponents in table 5.1 that have been established through the parameter analysis for the base case parameters shows how the PPD μ_0 and standard deviation σ_x are dependent on and scale by a single of those parameters while the rest are kept static. Those exponents contains information on how particle transport in the pore network level scale, i.e. the statistical distribution of particles, when parameters on the link level change. Now suppose that one wants to vary two, or even several, of the parameters simultaneously, or extrapolate the transport for values which have not been accounted for in previous simulations. The exponents can then be used as powers on their respective parameters to get new power law expressions which estimate the transport as

$$\mu_x = C_{\mu_x} (\mu_0)^{\beta^0_{\mu_x}} (d_l)^{\beta^1_{\mu_x}} \left(\frac{\Delta P_y}{L_y} \right)^{\beta^2_{\mu_x}} (D)^{\beta^3_{\mu_x}} (t_{\max})^{\beta^4_{\mu_x}}, \tag{5.14a}$$

$$\sigma_x = C_{\sigma_x} (\mu_0)^{\beta^0_{\sigma_x}} (d_l)^{\beta^1_{\sigma_x}} \left(\frac{\Delta P_y}{L_y} \right)^{\beta^2_{\sigma_x}} (D)^{\beta^3_{\sigma_x}} (t_{\max})^{\beta^4_{\sigma_x}}, \tag{5.14b}$$

where C_{μ_x} and C_{σ_x} are proportionality constants of units $\mathrm{m\,kg^2\,s^3}$. The superscripts of $\beta^i_{\mu_x}, \beta^i_{\sigma_x}$ indicate the row i in table 5.1, starting from 0, i.e. the parameters μ_0, d_l, $\Delta P_y / L_y$, D and $t_{\max}$ respectively. By solving eqs. (5.14a) to (5.14b) with respect to C_{μ_x} and C_{σ_x} and taking the mean, these constants are determined as

$$C_{\mu_x} = \frac{1}{M} \sum_{i=1}^{M} \frac{\mu_{x,i}}{(\mu_0)_i^{\beta^0_{\mu_x}} (d_{l,i})_i^{\beta^1_{\mu_x}} \left(\frac{\Delta P_y}{L_y} \right)_i^{\beta^2_{\mu_x}} (D)_i^{\beta^3_{\mu_x}} (t_{\max})_i^{\beta^4_{\mu_x}}}, \tag{5.15a}$$

$$C_{\sigma_x} = \frac{1}{M} \sum_{i=1}^{M} \frac{\sigma_{x,i}}{(\mu_{0,i})_i^{\beta^0_{\sigma_x}} (d_{l,i})_i^{\beta^1_{\sigma_x}} \left(\frac{\Delta P_y}{L_y} \right)_i^{\beta^2_{\sigma_x}} (D)_i^{\beta^3_{\sigma_x}} (t_{\max})_i^{\beta^4_{\sigma_x}}}, \tag{5.15b}$$

where i is one of M data points resulting from a given parameter analysis, where the numerators and one factor at a time in the denominators in eqs. (5.15a) to (5.15b) will vary, while the other factors are fixed, depending on which parameter was varied. One C_{μ_x} can thus be calculated from the variation of either μ_0, d_l, etc.

Once the proportionality constants have been determined, the time at which the particles are transported a distance $\mu_x = L_{\mu_x}$ can be extrapolated from eq. (5.14a), and equivalently for the standard deviation $\sigma_x = L_{\sigma_x}$, by solving with respect to time in eqs. (5.14a) to (5.14b) as

$$t_{\mu_x} = \left(\frac{L_{\mu_x}}{C_{\mu_x} (\mu_0)^{\beta^0_{\mu_x}} (d_l)^{\beta^1_{\mu_x}} \left(\frac{\Delta P_y}{L_y} \right)^{\beta^2_{\mu_x}} (D)^{\beta^3_{\mu_x}}} \right)^{1/\beta^4_{\mu_x}}, \tag{5.16a}$$

$$t_{\sigma_x} = \left(\frac{L_{\sigma_x}}{C_{\sigma_x} (\mu_0)^{\beta^0_{\sigma_x}} (d_l)^{\beta^1_{\sigma_x}} \left(\frac{\Delta P_y}{L_y} \right)^{\beta^2_{\sigma_x}} (D)^{\beta^3_{\sigma_x}}} \right)^{1/\beta^4_{\sigma_x}}. \tag{5.16b}$$

To show how these estimations hold up, calculations of exponents and proportionality constants were performed for simulations done at the times $t_{\max} = \{50, 100, 150\}$ seconds, in addition to the previously examined results for $t_{\max} = 300\,\mathrm{s}$ in section 5.1, and are summarized in tables 5.2 to 5.3. These were performed for the times in the same manner as described in section 3.5 and the corresponding exponents calculated from log-log plots as similarly seen in section 5.1 for $t_{\max} = 300\,\mathrm{s}$.

Table 5.2: Table of β_{μ_x} and the proportionality constant C_{μ_x} for times $t_{\max} = 50\,\mathrm{s}$ to $150\,\mathrm{s}$ in addition to those calculated for $t_{\max} = 300\,\mathrm{s}$ in section 5.1. Superscripts 0, 1, 2, 3, 4 corresponds to the power law eq. (A.2) slope estimation of PPD μ_x for parameters μ_0, d_l, $\Delta P_y/L_y$, D and $t_{\max}$ respectively. Due to some variations in the exponents for different times, the difference in C_{μ_x} are almost an order in magnitude in the extreme.

$t_{\max}$ [s]	$\beta^0_{\mu_x}$	$\beta^1_{\mu_x}$	$\beta^2_{\mu_x}$	$\beta^3_{\mu_x}$	$\beta^4_{\mu_x}$	C_{μ_x} [m kg^2 s^3]
50	-1.030	2.012	0.985	0	1.002	1.880×10^{-2}
100	-1.001	1.900	0.966	0	1.026	4.632×10^{-3}
150	-1.004	1.881	0.989	0	0.998	2.830×10^{-3}
300	-0.999	1.717	0.865	0	1.011	1.112×10^{-3}

The exponents for μ_x have some variation in $\beta^i_{\mu_x}$ at different times. This results in a difference of almost an order of magnitude for C_{μ_x} at most, as the constant is

Table 5.3: Table of β_{μ_x} and the proportionality constant C_{σ_x} for times $t_{\max} = 50\,\mathrm{s}$ to $150\,\mathrm{s}$ in addition to those calculated for $t_{\max} = 300\,\mathrm{s}$ in section 5.1. Superscripts 0, 1, 2, 3, 4 corresponds to to the power law eq. (A.2) slope estimation of σ_x for parameters μ_0, d_l, $\Delta P_y/L_y$, D and $t_{\max}$ respectively. The exponents are significantly close for 1 or 2 decimals, resulting in similar C_{σ_x} for all three times.

$t_{\max}$ [s]	$\beta^0_{\sigma_x}$	$\beta^1_{\sigma_x}$	$\beta^2_{\sigma_x}$	$\beta^3_{\sigma_x}$	$\beta^4_{\sigma_x}$	C_{σ_x} [m kg^2 s^3]
50	-0.502	0	0	0.486	0.490	2.303×10^{-2}
100	-0.506	0	0	0.490	0.492	2.472×10^{-2}
150	-0.505	0	0	0.488	0.496	2.326×10^{-2}
300	-0.476	0	0	0.488	0.495	2.758×10^{-2}

calculated using these exponents, and thus is sensitive for small differences in the exponents. The exponents for σ_x, on the other hand, have small variations for $\beta^i_{\sigma_x}$ at either the second or third decimals, causing C_{σ_x} to only have a variation in the first decimal.

Estimations of the particle transport are seen in fig. 5.26. The exponents and constants for different times in tables 5.2 to 5.3 were calculated and eqs. (5.14a) to (5.14b) used to extrapolate μ_x and σ_x for up to $t = 300\,\mathrm{s}$. Due to random fluctuations in the stochastic approach, the differences in tables 5.2 to 5.2 will result in variations in the final particle positions. The PPDs will thus slowly diverge for infinite times, and yield vastly different results. In a clinical and numerical setting, luckily, the time scales which are accounted for will not cause major differences in final particle positions in these simulations.

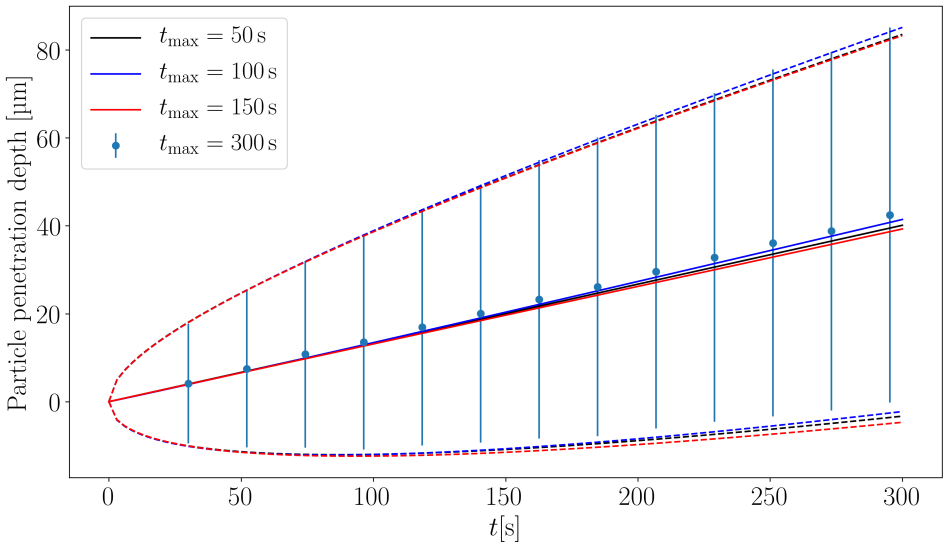

Figure 5.26: Estimation of particle transport, μ_x and $\mu_x \pm \sigma_x$, plotted from to $t = 0\,\mathrm{s}$ to $300\,\mathrm{s}$, where exponents in addition to C_{μ_x} and C_{σ_x} are summarized in tables 5.2 to 5.3 for the times $t_{\max} = \{50, 100, 150, 300\}$ seconds.

5.2.2 Estimation of network level parameters

The plot in fig. 5.22b shows the log-log plot of the standard deviation in eq. (2.26). This information can be used to get an estimate of the diffusion coefficient on the tissue-scale. The log-log of eq. (2.26) will be

$$\log \sigma_x = \frac{1}{2} \log 2\hat{D} + \frac{1}{2} \log t, \tag{5.17}$$

where $\hat{D}$ will be estimated from the intercept $a = \log \alpha$ in eq. (A.2) as

$$\hat{D} = 10^{2a - \log 2}. \tag{5.18}$$

With the values in the base case parameters table 3.1, the diffusion coefficient for a particle in free solution eq. (2.22) is $D = 7.569\,\mu m^2\,s^{-1}$. Due to the network tortuosity as defined in eq. (1.1), the diffusion constant is effectively reduced on the pore network level, and can thus be expressed as

$$D_{\text{eff}} = D \left(\frac{l_0}{l} \right)^2, \tag{5.19}$$

where, for a given row unit as described in fig. 3.1, $l_0 = dy = 1.5L$ is the unit height and $l = 2L$ the total tube path length in the row unit. The theoretical tortuosity is $\lambda = l/l_0 = 1.33$ and the effective diffusion coefficient in eq. (5.19) thus has a value of $D_{\text{eff}} = 4.279\,\mu m^2\,s^{-1}$. The numerical tortuosity eq. (1.1) is calculated by comparing eq. (5.18) to eq. (2.22) as

$$\hat{\lambda} = \sqrt{\frac{\hat{D}}{D}}. \tag{5.20}$$

The same operation can be performed to calculate the estimated mean vertical bulk velocity of the particles in the network from fig. 5.21a. The log-log of eq. (2.25) is

$$\log \mu_x = \log \hat{u} + \log t, \tag{5.21}$$

which can be solved from the intercept $a = \log \alpha$ in eq. (A.2) as

$$\hat{u} = 10^a. \tag{5.22}$$

The maximum and minimum fluid velocities in the links of the network respectively are $u_{\max} = 0.263\,\mu m\,s^{-1}$ and $u_{\min} = 0.131\,\mu m\,s^{-1}$. The maximum velocities occur in the vertical links, and the minimum in the non-vertical. Thus, one has to look at the vertical components of the velocity in the latter links, weighed by the ratio of $n_1 = 0.339$ vertical and $n_2 = 1 - n_1$ non-vertical links in the network as

$$\bar{u}_y = n_1 u_{\max} + n_2 u_{\min} \sin 30^\circ, \tag{5.23}$$

which yields $\bar{u}_y = 0.132\,\mu\mathrm{m\,s}^{-1}$. When compared to the velocity in eq. (5.22), the relative error of the simulated particle velocities can be expressed as

$$\delta\hat{u} = \frac{\hat{u} - \bar{u}_y}{\bar{u}_y}. \tag{5.24}$$

An alternative method to calculate the mean PPD can thus be to estimate the vertical components of the pore network fluid velocities by using eq. (5.23) and multiply with $t_{\max}$, instead of simulating the movement of n_p particles through the network, which bears a much higher computational cost.

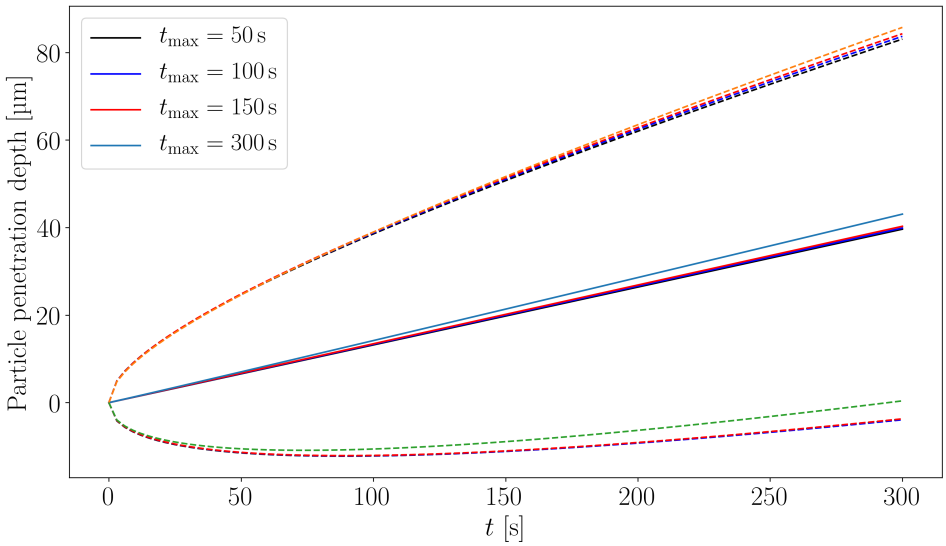

Figure 5.27: Estimation of particle transport $\hat{\mu}_x$ and $\hat{\mu}_x \pm \hat{\sigma}_x$, plotted for $t = 0\,\mathrm{s}$ to $300\,\mathrm{s}$. $\hat{\mu}_x$ and $\hat{\sigma}_x$ are calculated from eqs. (5.25a) to (5.25b) where $\hat{u}$ and $\hat{D}$ are summarized in table 5.4 and exponents in tables 5.2 to 5.3 for the times $t_{\max} = \{50, 100, 150, 300\}$ seconds.

A summary of the calculations of eq. (5.22), eq. (5.18), eq. (5.24) and eq. (5.20) is seen in table 5.4 for the times $t_{\max} = \{50, 100, 150, 300\}$ seconds. The calculated diffusion coefficients are smaller, and thus corresponding tortuosities larger, than for the theoretical effective diffusion coefficient in eq. (5.19). The tortuosity in fig. 1.5 is calculated as the ratio of path lengths, and the numerical one in eq. (5.20) from the root of diffusion coefficient ratios. While based on the same formula, the latter is calculated from the movement of particles for low Péclet numbers, approximately $\mathrm{Pe} \approx 0.087$. The advective contribution is small, which might cause some particles to not take the most efficient path through, thus increasing tortuosity.

Note that $\hat{u}$ and $\hat{D}$ still depend on the other input parameters from the parameter

studies. The difference is that $\hat{u}$ can be estimated from the pore network itself without transporting particles, or performing a parameter study for $t_{\max}$ in which the numerical tortuosity also can be calculated.

Once the fluid velocity and diffusion coefficient have been calculated in this manner, the mean and standard deviation can respectively be approximated as

$$\hat{\mu}_x = \hat{u}t^{\beta^4_{\mu_x}}, \tag{5.25a}$$

$$\hat{\sigma}_x = \sqrt{2\hat{D}}t^{\beta^4_{\sigma_x}}, \tag{5.25b}$$

where the exponents for $t_{\max}$ are included and listed in tables 5.2 to 5.3 for the different times $t_{\max}$.

Estimations of the particle transport using eqs. (5.25a) to (5.25b) are seen in fig. 5.27 for up to $t = 300\,\mathrm{s}$ calculated for $t_{\max} = \{50, 100, 150, 300\}$ seconds, summarized in table 5.4. The estimations for the three first times, unlike in fig. 5.26, seem to converge to the same values, while the estimation for $t_{\max} = 300\,\mathrm{s}$ is diverging away from those, yielding vastly different results for simulation times approaching infinity.

Table 5.4: Summary of the estimated variables $\hat{u}$, $\hat{D}$ and $\hat{\lambda}$ in addition to relative error $\delta\hat{u}$ for the velocity for times $t_{\max} = \{50, 100, 150, 300\}$ seconds.

$t_{\max}$ [s]	$\hat{u}$ [µm s^{-1}]	$\hat{D}$ [µm^2 s^{-1}]	$\delta\hat{u}$ [%]	$\hat{\lambda}$
50	0.131	3.543	-0.76	1.462
100	0.134	3.375	1.52	1.488
150	0.135	3.376	2.27	1.497
300	0.135	3.226	2.27	1.532

6 Clinical impact

The aim of the thesis was to gain a further understanding of how different transport parameters affect the distribution of NPs in the ECM by developing a numerical simulation tool, since performing experimental studies comes with costs both in terms of funds and time. Particle transport depends on the properties of the tumor tissue, US parameters and particles. This adds a complexity, making it difficult to investigate and perform tests of all variables involved in the system. Numerical modeling can serve as an aid to understand and evaluate this complexity.

The motivation behind using a pore network model was to approximate the fluid flow in a tumor with a well defined and interconnected collagen network with a regular structure, thus giving insight in how the different input parameters affect the particle transport. The parameter study established and demonstrated the scaling relations between variables of the system on pore-scale and how these impact particle transport into the interstitium at the tissue-scale for finite times. These relations allow for the derivation of empirical equation sets for the estimation and extrapolation of the particle positions.

The results in fig. 5.11a, in addition to the exponents summarized in table 5.2, show the impact of applying US, where the particle transport is almost fully linear with in the power law relation of eq. (A.1), with the exponents being lower than, but approximately close to 1. This means that as the pressure gradient $\Delta P_u/L_y$ becomes larger, the increase of PPD μ_0 slows down ever so slightly. For the sake of estimation purposes though, the slope can be considered to be approximately 1. The simulations have been performed with finite pressure gradients. To account for the absence of US, a zero value can be inserted into eq. (5.14a), which will yield $\mu_x = 0$. The standard deviation σ_x is independent of the pressure gradient even in this case, since the relevant exponents in table 5.3 are zero for $\Delta P_u/L_y$. The value 0^0 will appear in eq. (5.14b), but will be set to 1 since $\lim_{x\to 0} x^0 = 1$.

Most importantly, the model can be used to estimate the required treatment time. All living cells of the tissue are commonly located within 100 µm to 200 µm of perfused blood vessels, the diffusion limit for oxygen [50]. In histological sections, the viable cells are often actively seen growing around perfused blood vessels up to about 150 nm. This distance is also quoted to range from 70 mm to 200 mm

[51]. Assuming that all tumor cells are oxygenated the between two capillaries, the shortest intercapillary distance can be chosen as 140 nm. In order for all cells in the tumor to be affected by the treatment, NPs originating from one given capillary has to be transported throughout this whole intercapillary space. Suppose that the PPD in this example is chosen to be $L_x = \mu_x = 70\,\mu m$. This distance can be inserted into eq. (5.16a) to calculate the time at which this transport has occurred, which is then used in eq. (5.14b) to calculate the standard deviation of the particle transport at that time.

While the focus of this thesis is on the pore network, a brief discussion on the pressure gradient is called for. The upper range for IFP in tumors is from 10 mmHg to 30 mmHg [21]. In order to facilitate transport into the interstitium, the US-induced pressure gradient has to be larger than the IFP. For the simulations the base case pressure gradient was chosen to be $\Delta P_u/L_y = 2.5 \times 10^5\,\mathrm{Pa\,m^{-1}} = 1.9\,\mathrm{mmHg\,mm^{-1}}$, which will not be sufficient to overcome the higher IFP and improve particle transport. As seen in table 6.1, increasing the US frequency greatly increases the pressure gradients for. For example, the pressure gradients for 10 MHz to 20 MHz can be of sufficient magnitude to cause a net transport into the ECM.

Table 6.1: Summary of US-induced pressure gradients in $\mathrm{Pa\,m^{-1}}$ and correspondingly in $\mathrm{mmHg\,mm^{-1}}$ for given frequencies f. Data is taken from [46], where preliminary calculations for radiation force on tissue have given estimations on the pressure gradient.

f [MHz]	$\Delta P_u/L_y$ [$\mathrm{Pa\,m^{-1}}$]	$\Delta P_u/L_y$ [$\mathrm{mmHg\,mm^{-1}}$]
3	2.50×10^5	1.9
5	6.95×10^5	5.2
7	1.36×10^6	10.2
10	2.78×10^6	20.8
20	1.11×10^7	83.3

These values are based on preliminary calculations for the application of focused US and therefore radiation force on the tissue, which have to determined by experimental procedures. In an unpublished study, 5 MHz and 10 MHz focused US was applied to generate acoustic radiation forces of 5 $\mathrm{mmHg\,mm^{-1}}$ to 15 $\mathrm{mmHg\,mm^{-1}}$ in subcutaneous prostate tumors in mice [52]. The results seem to indicate that both extravasation and penetration of NPs through the ECM improves, and particles were found to be up to 200 µm away from the capillary, with acoustic streaming dominating over diffusive contributions. Experimental activities such as these are necessary to provide realistic input parameters to the simulations such as those performed for this thesis.

6.1 The role of advection and diffusion

Overall, there are complex phenomenon involving diffusive and advective effects that are not fully understood, but can still be incorporated into the pore network to better model how the ECM composition decreases the effective diffusion, in addition to facilitated diffusion arising from the presence of fluid flow in the medium and application of US. These effects are not accounted for in the current model.

The diffusion coefficient as given in eq. (2.22) is an estimation for a particle in free solution. In real tissues however, the diffusivity of the particles can be reduced by 18 % to 93 % due to electrostatic interactions between the solute and ECM components, in comparison to the free solution [14]. The charged components of the ECM that hinder diffusion of nanoparticles include collagen fibers and glycosaminoglycan (GAG) chains [53]. Experimental results also indicate that the concentration of collagen in the ECM impacts diffusion to a further degree than the structure of the collagen network itself [54].

Models of porous media have also shown that advection enhances the transport of macromolecules, such that the diffusion constant is increased in the presence of a macroscopic one-dimensional flow field in the network, in comparison to diffusion only. Moreover, when advective and diffusive effects contribute to transport, the effective diffusion decreases more slowly than by diffusion only for higher tortuosites, since the one-dimensional flow field facilitates the transport process [55].

Experimental results have shown that a US beam of moderate intensity, far below the intensity necessary to induce acoustic cavitation, can effectively be used to promote liposomes towards and into bacterial alginate hydrogel films similar in structure to that of the ECM. Acoustic streaming and thermal convection flow from acoustic heating can also speed up the penetration of liposomes through diffusion significantly, linear in relation to US intensity [56]. Measured values of the acoustic diffusion coefficient have also been found to be 74 % and 133 % larger than the diffusion coefficients of NPs of sizes 20 nm and 100 nm respectively, in addition acoustic streaming velocities in the order of $0.1\,\mu m\,s^{-1}$ arising from the US. [57]. These works seems to suggest that the application of US can enhance and cause facilitated diffusion of NPs in materials similar to the ECM, which is relevant to challenges involving US-mediated drug delivery in tissues.

6.2 Alternative models and improvement

In addition to the effects outlined in section 6.1, several improvements can be done to account for the heterogeneity of tumors, thus further improving the current pore network model.

Tumors can be be classified into soft and rigid groups depending on their mechanical behaviors when undergoing compression, and some soft tumors, such as the two carcinomas in fig. 1.2 may exhibit viscous properties that are more typical for macromolecular solutions rather than a well-structured solid matrix [13]. Even though the expression in eq. (2.11) describes the flow in a single tube, it can be compared to Darcy's law, which is a continuum approximation of the actual microscopic flow phenomenon that occurs in a porous medium, given as

$$\bar{u} = \frac{-K\boldsymbol{\nabla} p}{\mu} = -K'\boldsymbol{\nabla} p \tag{6.1}$$

where $\bar{u}$ is bulk-averaged fluid velocity, K the specific permeability, K' the hydraulic conductivity [14]. Both normal and tumor tissues have properties similar to those of a porous medium, in which empirical observations have shown that the fluid velocity on the tissue-scale is proportional to the pressure gradient. The permeability, and thus the conductivity, depends on different factors of the extracellular matrix, such as pore size, composition and geometry, and can be measured experimentally by measuring the steady flow rate over a tissue slice. This method provides values for the net interstitial flow on the tissue-scale, and not the local convective fluid velocity [11], as in the pore network model presented in this thesis. Additionally, the Navier–Stokes equations in blood flow through capillaries have been used to simulate interstitial and intravascular flows, where Starling's law is included for the movement of fluid across capillary membranes and for closing this system of equations [58].

If the cells were not to have fixed positions, other approaches than the kind of pore networks discussed in this thesis would have to be considered. However, a proposition can be to distribute the link diameters randomly over a interval of possible sizes. The consequence would be a disorder in the flow rates throughout the network, which in turn would affect the behavior of NP transport, since the next link for the advective step is chosen from a link selection where the weighted probability distribution is proportional to flow rates.

The NPs have also been assumed to be monodisperse, with all particles of equal size. For some nanocarriers, it is difficult to control the particle size distribution during their preparation. The polydisperity index (PDI), is sometimes used to describe the non-uniformity of the size distribution, and can range from 0.0 for uniformity of all particle sizes, to 1.0 for a highly polydisperse size distribution [59]. For future work, an analysis of particle transport for clinically relevant PDI can be of interest.

7 Conclusion and outlook

The work has concluded by providing a theoretical model and implementation for the transport of NPs in a rigid pore network subjected to the advection-diffusion equation and a US-induced pressure gradient, thus establishing relationships between parameters on the pore-scale and transport on the tissue-scale. Theory and discretization for a elastic pore network model has also been derived and presented.

Application of US does indeed improve the transport of particles. The flow rate at the pore-scale increases linearly with the pressure gradient, the effect of which is approximately linear at the tissue-scale for NPs. Empirical sets of equations have been derived to relate the scaling of transport at the pore-scale and tissue-scale, which can be used estimate required treatment times and particle transport for given input parameters. Estimations of fluid velocity at the tissue-scale and effective diffusion coefficients can also be calculated from the model to approximate the particle concentrations in the network.

The main goal for future work is to further develop the elastic pore network model to ensure its validity and check whether the hypothesis of net flow in the network holds up with an oscillating boundary condition. Thus, the physical problem involving the mechanical properties of both the capillary wall and gas bubble must be accounted for. The current rigid pore network model is regular, and it would be of great interest to consider a heterogeneous model in regards to link diameter and particle polydispersity. Additionally, if tissue deformation is to accounted for, other models than the Aker-type networks have to be considered. Hindrance and facilitation of diffusion respectively due to ECM composition, and the presence of fluid flow in the medium and application of US, are also effects of significant interest.

Bibliography

Articles

[6] R. K. Jain and T. Stylianopoulos. "Delivering nanomedicine to solid tumors". English. In: *Nature Reviews Clinical Oncology* 7.11 (2010), pp. 653–664. ISSN: 17594774 (ISSN).

[7] Siv Eggen et al. "Ultrasound Improves the Uptake and Distribution of Liposomal Doxorubicin in Prostate Cancer Xenografts". In: *Ultrasound in Medicine & Biology* 39.7 (July 2013), pp. 1255–1266. ISSN: 0301-5629. (Visited on 11/01/2017).

[8] Morton W. Miller, Douglas L. Miller, and Andrew A. Brayman. "A review of in vitro bioeffects of inertial ultrasonic cavitation from a mechanistic perspective". In: *Ultrasound in Medicine & Biology* 22.9 (Jan. 1996), pp. 1131–1154. ISSN: 0301-5629. (Visited on 11/09/2017).

[9] V. P. Chauhan et al. "Delivery of molecular and nanoscale medicine to tumors: Transport barriers and strategies". English. In: *Annual Review of Chemical and Biomolecular Engineering* 2 (2011), pp. 281–298. ISSN: 19475438 (ISSN).

[10] Sandra N. Ekdawi et al. "Spatial and temporal mapping of heterogeneity in liposome uptake and microvascular distribution in an orthotopic tumor xenograft model". In: *Journal of Controlled Release* 207 (June 2015), pp. 101–111. ISSN: 0168-3659. (Visited on 02/22/2019).

[11] Rakesh K. Jain. "Transport of Molecules in the Tumor Interstitium: A Review". en. In: *Cancer Research* 47.12 (June 1987), pp. 3039–3051. ISSN: 0008-5472, 1538-7445. (Visited on 03/21/2019).

[12] Joseph W. Nichols and You Han Bae. "EPR: Evidence and fallacy". In: *Journal of Controlled Release*. 30th Anniversary Special Issue 190 (Sept. 2014), pp. 451–464. ISSN: 0168-3659. (Visited on 05/08/2019).

[13] Paolo A. Netti et al. "Role of Extracellular Matrix Assembly in Interstitial Transport in Solid Tumors". en. In: *Cancer Research* 60.9 (May 2000), pp. 2497–2503. ISSN: 0008-5472, 1538-7445. (Visited on 03/19/2019).

[14] Melody A. Swartz and Mark E. Fleury. "Interstitial Flow and Its Effects in Soft Tissues". In: *Annual Review of Biomedical Engineering* 9.1 (July 2007), pp. 229–256. ISSN: 1523-9829. (Visited on 02/28/2019).

[15] James W. Baish et al. "Role of Tumor Vascular Architecture in Nutrient and Drug Delivery: An Invasion Percolation-Based Network Model". In: *Microvascular Research* 51.3 (May 1996), pp. 327–346. ISSN: 0026-2862. (Visited on 03/22/2019).

[16] Hiroya Hashizume et al. "Openings between Defective Endothelial Cells Explain Tumor Vessel Leakiness". In: *The American Journal of Pathology* 156.4 (Apr. 2000), pp. 1363–1380. ISSN: 0002-9440. (Visited on 03/22/2019).

[17] T. P. Padera et al. "Pathology – Cancer cells compress intratumour vessels". English. In: *Nature* 427.6976 (2004), p. 695. ISSN: 0028-0836. (Visited on 03/22/2019).

[18] Vikash P. Chauhan et al. "Multiscale Measurements Distinguish Cellular and Interstitial Hindrances to Diffusion In Vivo". In: *Biophysical Journal* 97.1 (July 2009), pp. 330–336. ISSN: 0006-3495. (Visited on 03/22/2019).

[19] Saroja Ramanujan et al. "Diffusion and Convection in Collagen Gels: Implications for Transport in the Tumor Interstitium". In: *Biophysical Journal* 83.3 (Sept. 2002), pp. 1650–1660. ISSN: 0006-3495. (Visited on 02/22/2019).

[20] Yves Boucher and Rakesh K. Jain. "Microvascular Pressure Is the Principal Driving Force for Interstitial Hypertension in Solid Tumors: Implications for Vascular Collapse". en. In: *Cancer Research* 52.18 (Sept. 1992), pp. 5110–5114. ISSN: 0008-5472, 1538-7445. (Visited on 03/22/2019).

[21] Yves Boucher, Laurence T. Baxter, and Rakesh K. Jain. "Interstitial Pressure Gradients in Tissue-isolated and Subcutaneous Tumors: Implications for Therapy". en. In: *Cancer Research* 50.15 (Aug. 1990), pp. 4478–4484. ISSN: 0008-5472, 1538-7445. (Visited on 03/19/2019).

[22] Junru Wu and Wesley L. Nyborg. "Ultrasound, cavitation bubbles and their interaction with cells". In: *Advanced Drug Delivery Reviews*. Ultrasound in Drug and Gene Delivery 60.10 (June 2008), pp. 1103–1116. ISSN: 0169-409X. (Visited on 11/09/2017).

[23] Katherine W. Ferrara. "Driving delivery vehicles with ultrasound". In: *Advanced Drug Delivery Reviews*. Ultrasound in Drug and Gene Delivery 60.10 (June 2008), pp. 1097–1102. ISSN: 0169-409X. (Visited on 02/22/2019).

[24] Baris E. Polat et al. "Ultrasound-mediated transdermal drug delivery: Mechanisms, scope, and emerging trends". In: *Journal of Controlled Release* 152.3 (June 2011), pp. 330–348. ISSN: 0168-3659. (Visited on 11/08/2017).

[25] William D. O'Brien. "Ultrasound–biophysics mechanisms". In: *Progress in Biophysics and Molecular Biology*. Effects of ultrasound and infrasound relevant to human health 93.1 (Jan. 2007), pp. 212–255. ISSN: 0079-6107. (Visited on 02/22/2019).

[26] Klazina Kooiman et al. "Acoustic behavior of microbubbles and implications for drug delivery". In: *Advanced Drug Delivery Reviews*. Ultrasound triggered drug delivery 72 (June 2014), pp. 28–48. ISSN: 0169-409X. (Visited on 03/21/2019).

[27] Vassilis Sboros. "Response of contrast agents to ultrasound". In: *Advanced Drug Delivery Reviews*. Ultrasound in Drug and Gene Delivery 60.10 (June 2008), pp. 1117–1136. ISSN: 0169-409X. (Visited on 03/21/2019).

[28] M. Afadzi et al. "Mechanisms of the ultrasound-mediated intracellular delivery of liposomes and dextrans". In: *IEEE Transactions on Ultrasonics, Ferroelectrics, and Frequency Control* 60.1 (Jan. 2013), pp. 21–33. ISSN: 0885-3010.

[29] Paul Dayton et al. "Acoustic radiation force in vivo: a mechanism to assist targeting of microbubbles". In: *Ultrasound in Medicine & Biology* 25.8 (Oct. 1999), pp. 1195–1201. ISSN: 0301-5629. (Visited on 03/21/2019).

[30] Chrit Moonen and Ine Lentacker. "Ultrasound assisted drug delivery". In: *Advanced Drug Delivery Reviews*. Ultrasound triggered drug delivery 72 (June 2014), pp. 1–2. ISSN: 0169-409X. (Visited on 03/21/2019).

[31] Michael Dunne, Kullervo Hynynen, and Christine Allen. "Thermosensitive nanomedicines could revolutionize thermal therapy in oncology". In: *Nano Today* 16 (Oct. 2017), pp. 9–13. ISSN: 1748-0132. (Visited on 03/21/2019).

[32] Annemieke van Wamel et al. "Acoustic Cluster Therapy (ACT) enhances the therapeutic efficacy of paclitaxel and Abraxane® for treatment of human prostate adenocarcinoma in mice". In: *Journal of Controlled Release* 236 (Aug. 2016), pp. 15–21. ISSN: 0168-3659. (Visited on 02/28/2019).

[33] Per Sontum et al. "Acoustic Cluster Therapy (ACT) – A novel concept for ultrasound mediated, targeted drug delivery". In: *International Journal of Pharmaceutics* 495.2 (Nov. 2015), pp. 1019–1027. ISSN: 0378-5173. (Visited on 02/28/2019).

[34] Andrew John Healey et al. "Acoustic Cluster Therapy: In Vitro and Ex Vivo Measurement of Activated Bubble Size Distribution and Temporal Dynamics". In: *Ultrasound in Medicine & Biology* 42.5 (May 2016), pp. 1145–1166. ISSN: 0301-5629. (Visited on 03/22/2019).

[35] Annemieke van Wamel et al. "Acoustic Cluster Therapy (ACT) - pre-clinical proof of principle for local drug delivery and enhanced uptake." eng. In: *158-164* (2016). ISSN: 0168-3659. (Visited on 03/22/2019).

[36] Eyvind Aker et al. "A Two-Dimensional Network Simulator for Two-Phase Flow in Porous Media". en. In: *Transport in Porous Media* 32.2 (Aug. 1998), pp. 163–186. ISSN: 1573-1634. (Visited on 01/03/2019).

[37] Magnus Aashammer Gjennestad et al. "Stable and efficient time integration of a dynamic pore network model for two-phase flow in porous media". eng. In: *6* (2018). ISSN: 2296-424X. (Visited on 01/14/2019).

[38] Isha Savani et al. "A Monte Carlo Algorithm for Immiscible Two-Phase Flow in Porous Media". en. In: *Transport in Porous Media* 116.2 (Jan. 2017), pp. 869–888. ISSN: 1573-1634. (Visited on 01/03/2019).

[43] Henning Arendt Knudsen, Eyvind Aker, and Alex Hansen. "Bulk Flow Regimes and Fractional Flow in 2D Porous Media by Numerical Simulations". en. In: *Transport in Porous Media* 47.1 (Apr. 2002), pp. 99–121. ISSN: 1573-1634. (Visited on 05/20/2019).

[44] V. Joekar-Niasar and S. M. Hassanizadeh. "Analysis of Fundamentals of Two-Phase Flow in Porous Media Using Dynamic Pore-Network Models: A Review". In: *Critical Reviews in Environmental Science and Technology* 42.18 (Sept. 2012), pp. 1895–1976. ISSN: 1064-3389. (Visited on 05/20/2019).

[47] Alain Pluen et al. "Diffusion of Macromolecules in Agarose Gels: Comparison of Linear and Globular Configurations". In: *Biophysical Journal* 77.1 (July 1999), pp. 542–552. ISSN: 0006-3495. (Visited on 05/20/2019).

[50] Heiko Rieger and Michael Welter. "Integrative models of vascular remodeling during tumor growth". en. In: *Wiley Interdisciplinary Reviews: Systems Biology and Medicine* 7.3 (2015), pp. 113–129. ISSN: 1939-005X. (Visited on 06/06/2019).

[51] S R McKeown. "Defining normoxia, physoxia and hypoxia in tumours—implications for treatment response". In: *The British Journal of Radiology* 87.1035 (Mar. 2014). ISSN: 0007-1285. (Visited on 06/06/2019).

[53] Triantafyllos Stylianopoulos et al. "Diffusion of Particles in the Extracellular Matrix: The Effect of Repulsive Electrostatic Interactions". In: *Biophysical Journal* 99.5 (Sept. 2010), pp. 1342–1349. ISSN: 0006-3495. (Visited on 06/07/2019).

[54] Arne Erikson et al. "Physical and chemical modifications of collagen gels: Impact on diffusion". en. In: *Biopolymers* 89.2 (2008), pp. 135–143. ISSN: 1097-0282. (Visited on 03/19/2019).

[55] Muhammad Sahimi. "Transport of macromolecules in porous media". In: *The Journal of Chemical Physics* 96.6 (Mar. 1992), pp. 4718–4728. ISSN: 0021-9606. (Visited on 06/06/2019).

[56] Dong Ma et al. "Effects of acoustic streaming from moderate-intensity pulsed ultrasound for enhancing biofilm mitigation effectiveness of drug-loaded liposomes". In: *The Journal of the Acoustical Society of America* 138.2 (Aug. 2015), pp. 1043–1051. ISSN: 0001-4966. (Visited on 06/06/2019).

[57] Dong Ma, Jeffrey S. Marshall, and Junru Wu. "Measurement of ultrasound-enhanced diffusion coefficient of nanoparticles in an agarose hydrogel". In: *The Journal of the Acoustical Society of America* 144.6 (Dec. 2018), pp. 3496–3502. ISSN: 0001-4966. (Visited on 06/06/2019).

[58] M. Soltani and P. Chen. "Numerical Modeling of Interstitial Fluid Flow Coupled with Blood Flow through a Remodeled Solid Tumor Microvascular Network". In: *PLOS ONE* 8.6 (June 2013), e67025. ISSN: 1932-6203. (Visited on 10/17/2017).

[59] M. Danaei et al. "Impact of Particle Size and Polydispersity Index on the Clinical Applications of Lipidic Nanocarrier Systems". In: *Pharmaceutics* 10.2 (May 2018). ISSN: 1999-4923. (Visited on 06/11/2019).

Books

[1] Gregory Bertoni Wayne M. Becker Jeff Hardin and Lewis J. Kleinsmith. *Becker's World of the Cell*. 8th ed. Pearson Education Inc., 2012.

[5] Amato J. Giaccia Eric J. Hall. *Radiology for the Radiologist*. 7th ed. Lippincott Williams & Wilkins, 2012.

[39] L.D. Laudau and E.M. Lifshitz. *Fluid Mechanics*. 2nd ed. Butterworth-Heinemann, 2012.

[41] Tilman Neunhoeffer Micheal Griebel Thomas Dornseifer. *Numerical Simulation in Fluid Dynamics: A Practical Introduction*. Society for Industrial and Applied Mathematics, 1998.

[42] Edwin N. Lightfoot R. Byron Bird Warren E. Stewart. *Transport phenomena*. 2nd ed. John Wiley & Sons, Inc, 2007.

[45] N.G. van Kampen. *Stochastic Processes in Physics and Chemistry*. 3rd ed. Elsevier, 2007.

[48] Ricardo Jauregui Tellería and Fernando Silva Martínez. *Numerical validation methods*. eng. INTECH, Sept. 2011. ISBN: 978-953-307-389-7. URL: https://upcommons.upc.edu/handle/2117/13404 (visited on 05/03/2019).

[49] Sharon L. Myers Ronald E. Walpole Raymond H. Myers and Keying Ye. *Probability & Statistics for Engineers & Scientists*. 8th ed. Pearson Education International, 2007.

Webpages and other documents

[2] *Fakta om kreft*. no. URL: https://www.kreftregisteret.no/Generelt/Fakta-om-kreft/ (visited on 02/13/2019).

[3] *WHO | Cancer*. URL: http://www.who.int/cancer/en/ (visited on 02/13/2019).

[4] *Stor økning i krefttilfeller fram mot 2030*. no. URL: https://www.kreftregisteret.no/Generelt/Nyheter/Stor-okning-i-krefttilfeller-fram-mot-2030/ (visited on 02/13/2019).

[40] *Cardiovascular biomechanics*. Oct. 9, 2018. URL: https://folk.ntnu.no/leifh/teaching/tkt4150/main.pdf.

[46] Stian Solberg Bjørn A J Angelsen Robin Cleveland. *Ultrasound Radiation Force on Sub-Cellular Scale*. Nov. 2017.

[52] Mercy Afadzi et al. *Effect of acoustic radiation force on the distribution of nanoparticles in solid tumors*. unpublished article. 2019.

Appendix

A Power laws and log-log plots

Log-plots can be used to test whether some kind of data follow power laws of the form

$$y = \alpha x^{\beta}. \tag{A.1}$$

To gain more information or trends about the data, α and β can be extracted to establish if the relationship between x and y follows a power law. For these kinds of expressions the logarithm can be taken for eq. (A.1). This yields

$$\log y = \beta \log x + \log \alpha, \tag{A.2}$$

which can be plotted in a log-log plot. Base 10 is chosen to more easily interpret the values on the logarithmic axes. If eq. (A.2) is a straight line, the power term β will be the slope of the line as a function of $\log x$. The line intercept will be the constant term $\log \alpha$.

Linear regression can then be used to fit a line for data according to eq. (A.2). The sample coefficient of determination [49, p. 435], defined as

$$R^2 = r_{xy}^2, \tag{A.3}$$

is used to establish if there is a good linear association between $\log x$ and $\log y$. The sample correlation coefficient r_{xy} is given as

$$r_{xy} = \frac{S_{xy}}{\sqrt{S_{xx} S_{yy}}}. \tag{A.4}$$

A perfect linear relationship appears in the data if $r_{xy} = \pm 1$. The terms in eq. (A.4) are defined [49, p. 401] as

$$S_{xy} = \sum_{i=1}^{n} (x_i - \bar{x})(y_i - \bar{y}), \tag{A.5a}$$

$$S_{xx} = \sum_{i=1}^{n} (x_i - \bar{x})^2, \tag{A.5b}$$

$$S_{yy} = \sum_{i=1}^{n} (y_i - \bar{y})^2, \tag{A.5c}$$

where n is the number of data points, (x_i, y_i) a data point and $\bar{x}$ and $\bar{y}$ the sample means for x and y respectively. R^2 expresses the proportion of the total variation of the values y_i in the log-log plot which can be accounted for by the linear relationship with the values of x_i.

The slope β and intercept $\log \alpha$ are thus calculated through linear regression and used to construct a line which is compared to the data points in order to determine how well the power law coefficients are estimated. The closer R^2 is to 1, the better the variation of $\log y$ is accounted for by a linear relationship with $\log x$, and thus the power law analysis is more accurate.

B Dimensional analysis

In the expression for tube flow in eq. (2.11), the tube itself is described by its radius R and length L. Suppose that one wants to use another scale for the system and use some other tube which has a different radius and length, but in which the flow rate appropriately scaled. This means that one needs to have geometric similarity, which means that the ratios of dimensions for the tube in the original system and scaled system must be the same. Additionally, one must have dynamic similarity, and the dimensionless groups in the expression for flow rate must be the same for different systems [42, p.97].

Since this is a flow system, scale factors related to both the physical properties of the tube and fluid, such as tube length L, fluid viscosity μ and density ρ can be suitable. Scaling factors can be arbitrarily chosen, but they must contain the required units m, kg and s, which is a requirement to make the other variables dimensionless. Since the expression for Hagen–Poiseuille flow in eq. (2.11) does not contain ρ as one of its factors, a trick is to temporarily rewrite it as an expression with density. Kinematic viscosity, ν, can be expressed as a product of the dynamic viscosity μ and interstitial fluid density ρ as

$$\nu = \frac{\mu}{\rho}, \tag{B.6}$$

with units $[\nu] = \mathrm{m}^2\,\mathrm{s}^{-1}$. The expression for the fluid flow in eq. (2.11) can then be written as

$$q = \frac{-\pi R^4}{8\rho\nu L}\Delta p, \tag{B.7}$$

which can be given as a function in which the flow rate q depends on the variables on the right hand side:

$$q = f(R, L, \nu, \rho, \Delta p). \tag{B.8}$$

Its now possible to create dimensionless groups in which the dynamic viscosity can be substituted back. The dimension matrix for this equation can be written as follows

$$\begin{bmatrix} 3 & 0 & -1 \\ 1 & 0 & 0 \\ 1 & 0 & 0 \\ 2 & 0 & 1 \\ -3 & 1 & 0 \\ -1 & 1 & -2 \end{bmatrix} \begin{bmatrix} \mathrm{m} \\ \mathrm{kg} \\ \mathrm{s} \end{bmatrix} = \begin{bmatrix} [q] \\ [R] \\ [L] \\ [\nu] \\ [\rho] \\ [\Delta p] \end{bmatrix}, \tag{B.9}$$

where flow rate q has been added to the matrix in order to get an dimensionless group which contains it, since it will be advantageous for the sake of the simulations that all variables are dimensionless.

For simplicity, the dimension matrix eq. (B.9) can be written in augmented form as

$$\left[\begin{array}{ccc|c} 3 & 0 & -1 & [q] \\ 1 & 0 & 0 & [R] \\ 1 & 0 & 0 & [L] \\ 2 & 0 & -1 & [\nu] \\ -3 & 1 & 0 & [\rho] \\ -1 & 1 & -2 & [\Delta p] \end{array}\right] \tag{B.10}$$

The matrix has a rank of 3 with 6 variables, which means that there are $6-3=3$ independent dimensionless groups. Gauss-Jordan of eq. (B.10) elimination yields the reduced row echelon form as

$$\left[\begin{array}{ccc|c} 1 & 0 & 0 & [L] \\ 0 & 1 & 0 & [\rho L^3] \\ 0 & 0 & 1 & [\frac{L^2}{\nu}] \\ 0 & 0 & 0 & [\frac{q}{L\nu}] \\ 0 & 0 & 0 & [\frac{R}{L}] \\ 0 & 0 & 0 & [\frac{\Delta p L}{\rho \nu^2}] \end{array}\right] \tag{B.11}$$

The three first rows constitute the characteristic unit variables. These can be suitable for usage in the numerical simulations, for example to make a dimensionless time dimensional. The dimensionless groups in the final matrix eq. (B.11), with ρ substituted back, are

$$\frac{R}{L}, \tag{B.12a}$$

$$\frac{q}{L\nu} = \frac{q\rho}{L\mu}, \tag{B.12b}$$

$$\frac{\Delta p L}{\rho \nu^2} = \frac{\Delta p L^2 \rho}{\mu^2}. \tag{B.12c}$$

Since eqs. (B.12a) to (B.12c) are dimensionless, all variables in expression for Hagen–Poiseuille flow eq. (2.11) can be expressed in dimensionless form by using characteristic variables length L_0, density ρ_0 and dynamic viscosity μ_0. This analysis can also be extended to include the necessary variables of the advection-diffusion equation for the particles in eq. (2.23), and elastic network in eq. (2.20), which will introduce additional dimensionless groups.

C Program Source Code

The source code for the numerical program used throughout the process of writing this thesis is hosted on Bitbucket in a repository.
`https://bitbucket.org/stigenstig/npflow/`